INVESTIGATIONS OF NORTHERN HEMISPHERE STRATOSPHERIC POLAR VORTEX DISTURBANCES

A Dissertation

Presented to the Faculty of the Graduate School

of Cornell University

In Partial Fulfillment of the Requirements for the Degree of

Doctor of Philosophy

by

Thomas Ehrmann

May 2019

INVESTIGATIONS OF NORTHERN HEMISPHERE STRATOSPHERIC POLAR VORTEX DISTURBANCES

Thomas Ehrmann, Ph. D.

Cornell University 2019

The polar vortex is the dominant dynamic feature of the wintertime polar stratosphere. The defining characteristic of the Northern Hemisphere polar vortex is its interannual and intraseasonal variability caused by global scale atmospheric waves propagating into the stratosphere from the troposphere. This variability is manifest by disturbances which, in this study, are strictly defined and identified in the reanalysis data for the Northern Hemisphere winters from 1981 to 2017. Sixty disturbances are found over the 37 winters by taking geometric moments of Ertel's potential vorticity and classifying the polar vortex as either undisturbed, displaced off of the pole, or split into two or more vortices. The position of the polar vortex during each disturbance event is averaged and applied to thermodynamic diagnostic quantities in the air column enclosed by the polar vortex. This diagnosis reveals that the location of the disturbed polar vortex experiences, on average, cooling driven by horizontal temperature advection in the lower and middle stratosphere prior to the onset of the disturbance, along with significant residual (likely adiabatic) cooling in the troposphere in the weeks surrounding the onset. The relationship these polar vortex disturbances have with other dynamic phenomena in the stratosphere is also explored, namely: the Aleutian high, the Atlantic high, and the quasi-biennial oscillation. The likelihood of a disturbed day is negatively correlated with the stratospheric quasi-biennial oscillation (positively correlated with its easterly phase). It is also,

surprisingly, negatively correlated with the presence of a stratospheric Aleutian anticyclone (the Aleutian high). Finally, a series of experiments were performed using a dry-core idealized general circulation model that contained a stratospheric polar vortex. A topographic and tropospheric eddy temperature wave are added as forcing to the model with varying phase differences between them to see how polar vortex is affected. This revealed that eddy warming (cooling) west of the peak in the topography by 45° latitude is the most (least) optimal configuration for causing a polar vortex disturbance because this increases (decreases) vertically propagating wave activity fluxes in both the upper and lower troposphere.

BIOGRAPHICAL SKETCH

Thomas Stephen Ehrmann was born on January 25, 1989 and raised in West Deptford, New Jersey. His father is Thomas Mark Ehrmann, his mother is Mary Ellen Ehrmann, and his younger brother is Daniel James Ehrmann, married to Samantha Rae Ehrmann. He graduated high school in 2007, and from there attended Embry-Riddle Aeronautical University in Daytona Beach, Florida. At Embry-Riddle he received his bachelor's and master's degrees in Engineering Physics. While attaining his master's degree, he completed a master's thesis, under the advisement of Dr. John Hughes, studying the stratospheric polar vortex. After completing his master's degree, in 2012, Thomas spent a year working at a pizzeria and living in a housing cooperative in Philadelphia, Pennsylvania. In the fall of 2014 he began attending Cornell University under the advisement of Dr. Stephen Colucci, again research the stratospheric polar vortex. During his time at Cornell University Thomas met his partner, Dr. Ariel Wan-Yee Chan. He will complete his doctorate degree in Atmospheric Science in May, 2019.

I dedicate this work to be beautiful and brilliant fiancée, Ariel Chan. Your support and compassion have made these years the best of my life.

ACKNOWLEDGMENTS

I would like to acknowledge my committee members: Stephen Colucci, David Hysell, Peter Diamessis, and Peter Hess. Additionally, I would like to acknowledge Mark Wysocki, Susan Riha, Toby Ault, and Isla Simpson. Thank you all for your help and support through this process. This research was supported in part by a grant from the National Science Foundation to Cornell University. I would like to acknowledge high-performance computing support from Cheyenne provided by NCAR's Computational and Information Systems Laboratory, sponsored by the National Science Foundation.

TABLE OF CONTENTS

LIST OF FIGURES

represents all disturbances (displacements and splits combined). The bold dashed lines show the values smoothed with a 5-day moving average.

Figure 6: The frequency of a disturbed vortex (left ordinate) is shown as a function of year. As in Figure 4 blue represents displacements, red represents splits, and black represents all disturbances (displacements and splits combined). The dashed lines show the mean values for each of those three quantities. The gray bars represent the number of PVD events identified in each year (right ordinate).

Figure 7: Composites of all 60 PVDs with the area filter associated with each event from 20 days before through 30 days after the onset. The vertical dotted line represents the onset. **a)** Normalized height anomalies in color, contoured at 0.1 standard deviation intervals. Analyzed height tendencies (m/days) in black, contoured at 10 m/days intervals with the bold contour representing zero and dashed contours being negative. **b)** Normalized temperature anomalies in color, contoured at 0.1 standard deviation intervals. Analyzed temperature tendencies (K/days) in black, contoured at 0.5 K/days intervals with the bold contour representing zero and dashed contours being negative.

Figure 8: Composites of all 60 PVDs with the area filter associated with each event from 20 days before through 30 days after the onset. The vertical dotted line represents the onset. **a)** the analyzed temperature changes, **b)** the temperature changes from horizontal advection, and **c)** the residual temperature changes. All temperature changes in units of K/day. The zero contour is dark black and the color scale on each panel is unique. Values below 99% statistical significance are removed.

Figure 9: Thermodynamic energy budget values for the 10 Apr 1993 PVD averaged with the area filter associated with the event (Figure 1a) from 20 days before through 30 days after the onset. The vertical dotted line represents the onset. **a)** the analyzed temperature changes, **b)** the temperature changes from horizontal advection, **c)** the

adiabatic temperature changes, and **d)** the residual temperature changes. All temperature changes in units of K/day.

Figure 10: a) Equatorial zonal-mean zonal wind at 50 hPa averaged over the winter season (DJF) for each year representing the phase of the QBO. **b)** The fraction of days in the extended winter season (NDJFM) in which an AH is present. The correlation coefficient with the disturbance time series from Figure 5, along with the p-value of that correlation is in the upper right corner of each plot.

Figure 11: a) Area average representing the position of the polar vortex during AH PVDs. **b)** Average PV field, in units of $m^2s^{-1}K\ kg^{-1}$, of AH PVDs. **c)** Area average representing the position of the polar vortex during non-AH PVDs. **d)** Average PV field, in units of $m^2s^{-1}K\ kg^{-1}$, of a non-AH PVD. Longitude 90W is marked with -90^o and the Greenwich Meridian is marked with 0^o.

Figure 12: Composites of 31 AH PVDs minus composite of 29 non-AH PVDs. The vertical dotted line represents the onset. **a)** The analyzed temperature changes, **b)** the temperature changes from horizontal advection, and **c)** the residual temperature changes. All temperature changes in units of K/day. Values above 99% and 95% statistical significance are contoured in dashed and solid white lines, respectively.

Figure 13: a) Area average representing the position of the polar vortex during a QBOe PVD. **b)** Average PV field, in units of $m^2s^{-1}K\ kg^{-1}$, of a QBOe PVD. **c)** Area average representing the position of the polar vortex during a QBOw PVD. **d)** Average PV field, in units of $m^2s^{-1}K\ kg^{-1}$, of a QBOw PVD. Longitude 90W is marked with -90^o and the Greenwich Meridian is marked with 0^o.

Figure 14: Composites of 21 QBOe PVDs minus composite of 39 QBOw PVDs. The vertical dotted line represents the onset. **a)** The analyzed temperature changes, **b)** the temperature changes from horizontal advection and **c)** the residual temperature

changes. All temperature changes in units of K/day. Values above 99% and 95% statistical significance are contoured in dashed and solid white lines, respectively.

Figure 15: Days satisfying Aleutian High spatial criteria (blue shading) as a function of Day of Year relative to January 1 (Day 0) and the Year of that January 1. Each circle denotes the onset of an Aleutian High event, or a sequence of days satisfying both the spatial and temporal Aleutian High criteria. Each red asterisk marks a wave-breaking block onset within 100E – 80W. Each Aleutian High onset within day -15 and day +5 of a local block onset is marked with a cross beneath its circle.

Figure 16: Each day with a displaced or split polar vortex marked with green or red shading respectively. The onset of each PVD is marked with a cross. The blue shading and black circles are as in Figure 15.

Figure 17: Geopotential height tendencies [m $(10d)^{-1}$] averaged over the area enclosed by each Aleutian High at its onset and composited over all 68 Aleutian High cases as a function of Days from Onset (Day 0) and Pressure (hPa): (a) height tendencies calculated directly from the analyzed geopotential heights, (b) Sum total of height tendencies calculated from all forcing and boundaries, (c) height tendencies due to potential vorticity changes in the troposphere, (d) height tendencies due to potential vorticity changes in the stratosphere, and (e) height tendencies due to the height changes at the lower boundary pressure level. The contour interval is 100 m $(10d)^{-1}$ in panels (a), (b) and (d), 5 m $(10d)^{-1}$ in panel (c), and 2 m $(10d)^{-1}$ in panel (e). The bold dark contour is zero. Areas within solid and dashed white curves denote 95% and 99% significance, respectively, while the vertical dotted white line is Day 0.

Figure 18: As in Figure 17, but composited over the 13 Aleutian High cases coinciding with local blocking, determined from a wave-breaking definition and that the contour interval is 4 m $(10d)^{-1}$ in panel (e).

Figure 19: As in Figure 17, but composited over all 68 Aleutian High cases as a function of days from Decay (Day 0) and that the contour interval is 50 m $(10d)^{-1}$ in panels (b) and (d).

Figure 20: Eddy heat fluxes (K m s^{-1}) averaged over the area enclosed by each Aleutian High at its onset and composited over all 68 Aleutian High cases as a function of Days from Onset (Day 0) and Pressure (hPa). The contour interval is 25 K m s^{-1} and the white dotted line marks Day 0.

Figure 21: As in Figure 20, but averaged over the area enclosed by each Aleutian High at its decay and composited over all 68 Aleutian High cases as a function of Days from Decay (Day 0) and Pressure (hPa). The contour interval is 20 K m s^{-1}.

Figure 22: Histograms of the centroid latitude and longitude of the polar vortex in each control model run. The vertical red line in the centroid latitude plots represents the threshold for determining a displaced vortex (76.7°N).

Figure 23: The percentage of disturbed days, number of PVD events, and average PVD duration in days is shown as a function of the phase difference between the topography and temperature forcing for the 2 km topography runs. The values for the topography only and thermal forcing only runs are shown with dashed black and red lines, respectively.

Figure 24: Same as Figure 23 but for the 1.5 km topography runs.

Figure 25: The time-mean vertical EP flux in all four model control runs as a function of latitude and pressure, and in units of m^2/s^2.

Figure 26: Same as Figure 25 but for all the 1.5 km topography and temperature forcing runs.

Figure 27: The time-mean WAFz in the control runs in upper and lower troposphere in units of m^2/s^2.

LIST OF TABLES

CHAPTER 1

INTRODUCTION

General Overview

The polar vortex is a term that has become increasingly prevalent in popular culture and in the scientific literature. This is largely due to the recent high profile cold-air outbreaks in northeastern North America in the winters of 2014 and 2019 that were associated with disturbances of the polar vortex. The research presented here will be focused on the dynamics surrounding the polar vortex in the Northern Hemisphere of Earth's stratosphere. In order to understand this work, it is important to first establish the current understanding of the related topics in atmospheric science.

The atmosphere, when considered from a global perspective, is regarded as a geophysical fluid, meaning a fluid that is moving around an Earth-sized sphere in a rotating reference frame. The governing equations for a geophysical fluid are the Navier-Stokes equations, with the system of equations closed by the ideal gas law and the hydrostatic assumption. The Navier-Stokes equations describe the conservation of mass, momentum, and energy in a fluid. The ideal gas law assumes that, within a gas, pressure is directly related to both density and temperature. Last, the hydrostatic assumption defines the pressure over an area to be the weight of all the air per unit area above that area, thus defining the vertical gradient of pressure to be negative everywhere. These equations can be used to derive the wind velocity, temperature, pressure, and density throughout the entire system.

The vertical structure of the atmosphere is usually divided into four layers, each of which is often considered distinctly. These four layers are defined by reversals in the vertical temperature gradient. Starting near the surface and proceeding upwards, they are the troposphere, stratosphere, mesosphere, and thermosphere. The troposphere features variability with the smallest spatial and time scales, and is therefore where most of the variability associated with weather phenomena occur. Additionally, nearly all of the water vapor in the atmosphere is

contained within the troposphere. Much of the work in this research is focused on the stratosphere and how the troposphere relates to the stratosphere. The dynamics of the stratosphere are controlled by phenomena with large spatial and time scales. Because of this the stratosphere is generally symmetric in the longitudinal (zonal) direction, and it evolves mostly with the seasonal cycle. The stratosphere also has very stable stratification due to the positive vertical temperature gradient. This makes it difficult for information to propagate vertically into the stratosphere, which prevents the small-scale disturbances of the troposphere from perturbing the stratosphere.

During the winter seasons in both hemispheres the polar stratosphere is completely blocked from receiving solar radiation by the Earth, entering into polar night. This leads to a dramatic cooling of the polar air, and an enhanced temperature gradient in the latitudinal (meridional) direction toward the warmer equator. This temperature gradient leads to a pressure gradient, from the ideal gas law, that accelerates air toward the winter pole. Since the Earth is a rotating reference frame, anything that moves in the meridional direction will be subject to the Coriolis force. In both hemispheres, when air is moved toward the respective pole it is deflected toward the east. Then the Coriolis force and the pressure gradient balance each other as the wind forms a circumpolar westerly jet in the high latitude stratosphere known as the polar vortex.

In the southern hemisphere, the winter polar vortex is nearly zonally symmetric with a strong coherent wind structure that reaches maximum wind speeds around 60°S in the middle stratosphere. This strong zonal jet isolates the air in the southern polar vortex, preventing it from mixing with low latitudes. This isolation result in a decrease in the ozone density since ozone is created by ultraviolet radiation. In the northern hemisphere, the polar vortex tends to be less zonally symmetric, but the peak winds still occur around 60°N. In fact, the climatology of the northern hemisphere winter has the polar vortex displaced slightly toward Scandinavia with a climatological anticyclone over the northern Pacific known as the Aleutian high. The asymmetry in the northern hemisphere stratosphere is the result of planetary scale waves generated by the

topography and variability in the troposphere. These waves, which are driven the Coriolis force, are known as Rossby waves.

There are two principal research projects presented in this dissertation: one studying the polar vortex and related stratospheric phenomena such as anticyclones and the quasibiennial oscillation (QBO) in reanalysis data, and the other studying the polar vortex in an idealized general circulation model (GCM). The results from the first project have already been reported in two publications (Colucci and Ehrmann 2018; Ehrmann and Colucci 2019) while the results from the second project are unpublished.

Literature Review

The stratospheric polar vortex is the dominant dynamic feature of the winter stratosphere, and it has attracted considerable recent attention in the scientific literature and news media (Waugh and Polvani 2010; Waugh et al. 2016). Specifically, disturbances to the polar vortex, such as splits or displacements, are associated with an increase in planetary scale Rossby waves entering into the stratosphere from the troposphere (Matsuno 1971; Polvani and Waugh 2004). This increase in wave activity is evident into the mesosphere and thermosphere (Stray et al. 2015; Yiğit and Medvedev 2016). In an extremely disturbed state, the stratosphere can anomalously warm and experience a reversal of the zonal mean zonal flow over middle to high latitudes from westerly to easterly (Limpasuvan et al. 2004; Charlton and Polvani 2007; Hitchcock et al. 2013). These events are known as Sudden Stratospheric Warmings (SSWs).

A list and climatology of SSWs was established by Charlton and Polvani (2007), and more recently expanded by Butler et al. (2017), defining SSWs as a mid-winter reversal of the zonal mean zonal wind at 60°N on the 10 hPa isobaric surface. However, Coughlin and Gray (2009) concluded that 60°N may not be the best indicator of a disturbed polar vortex, and there is an on-going discussion about how best to identify mid-winter disturbances of the polar vortex (Palmeiro et al. 2015; Butler et al. 2015). One method for assessing the state of the stratospheric

vortex that has become increasingly popular is geometric moments. The technique was first applied by Waugh (1997) and Waugh and Randel (1999) to show that the Arctic vortex experiences more variability, and is more climatologically displaced and elongated, than its Antarctic counterpart. More recently, moments were used by Hannachi et al. (2011) and Mitchell et al. (2011) to demonstrate the statistically distinct structure of split versus displacement vortex disturbances. The moments technique was simplified by Seviour et al. (2013) so it could be quickly applied to identify split and displaced vortices, and Mitchell et al. (2013) used moments to create a catalog of split and displacement events to quantify tropospheric signatures. It is worth noting that these mid-winter disturbances of the polar vortex are usually considered separate from the climatological breakdown of the vortex as the high latitude stratosphere returns to summer conditions; this is referred to as the final warming.

A common feature of the Northern Hemisphere wintertime stratosphere is a large anticyclone near the Aleutian Islands, known as the Aleutian High (AH). First noted by Hare (1960), the structure and climatology of the AH were documented by Harvey and Hitchman (1996). Despite this considerable attention, the mechanisms leading to the formation, evolution and decay of the AH are not well understood. It has been suggested in idealized modeling studies (O'Neill and Pope 1988) that the AH could result from an "upward burrowing" of anticyclones (such as blocking highs) from the troposphere. Furthermore, Rosier and Lawrence (1999) have suggested that an enlarged AH can help displace the stratospheric polar vortex off the polar cap.

The polar vortex is also related to the quasi-biennial oscillation (QBO). The QBO is the dominant dynamic feature of the equatorial stratosphere, with zonal-mean zonal winds (ZMZW) oscillating between easterly and westerly over a period of about 28 months. The polar vortex tends to be weaker during winters were the QBO is in the easterly phase, relating to an increase in wave activity converging at high latitudes (Holton and Tan 1980; Watson and Gray 2014).

Many previous studies have linked tropospheric blocking and surface pressure anomalies as a precursor to SSWs. Colucci and Kelleher (2015, hereafter CK) show that all SSWs during 1980

– 2012 were preceded by or coincided with tropospheric blocking events. Those blocking events were associated with significantly larger upper tropospheric poleward eddy heat fluxes, stratospheric thermally forced geopotential height rises near the polar vortex, and height falls equatorward of the polar vortex than those blocking events not associated with SSWs. Surface pressure lows and decreased blocking in the northern Pacific, along with surface highs and increased blocking in Europe are connected to vortex disturbances by constructive interference with climatological planetary waves (Garfinkel et al. 2010; Huang et al. 2017). Furthermore, Bao et al. (2017) demonstrated lows over the Western Hemisphere and highs over Pacific-North America to be stronger precursors to SSWs than Pacific lows and European highs.

The influence of these polar vortex disturbances on the troposphere has been well documented. A weakened polar vortex corresponds to anomalies in the Northern-Annular Mode, which propagate down to the surface and can persist for weeks (Limpasuvan et al. 2004; Karpechko et al. 2017). The strength of the polar vortex also correlates with the position of the mid-latitude tropospheric jet, with a weaker vortex corresponding to an equatorward shift in the jet (Kidston et al. 2015; Dunn-Sigouin and Shaw 2015). SSWs also lead to an increase in the likelihood of a cold air outbreaks over Eurasia and North America (Kolstad et al. 2010; Mitchell et al. 2013; Yu et al. 2015a,b; Kidston et al. 2015; Jia et al. 2017; Karpechko et al. 2017; Kretschmer et al. 2018). Yu et al. (2015a,b) interpret these outbreaks as discharges of polar air toward mid-latitudes accompanying warm-air transport into the high latitude stratosphere.

Recent studies have begun to analyze temperature anomalies in the mid-latitude troposphere preceding the onset of SSWs. Kolstad et al. (2010) showed in composite analyses that the onsets of SSWs were preceded by lower tropospheric cold-air anomalies over Eurasia, and weaker vortex disturbances, not satisfying the strict SSW criteria, were preceded in onset by lower tropospheric cold-air anomalies over North America. Especially noteworthy, Lehtonen and Karpechko (2016) showed strong cold and warm anomalies over Eurasia and North America, respectively, preceding SSW onset, especially for displacement events. In their research, the

sea-level pressure anomalies and near surface temperature anomalies both have a wave 1 zonal structure preceding SSW onset, however, there is phase difference between the two wave patterns. Understanding how these temperature anomalies influence the polar vortex, and the importance of this phase difference between the temperature and sea-level pressure anomalies motivates the modelling research presented here.

The purpose of this research is to investigate stratospheric polar vortex disturbances (PVDs), especially how these disturbances are influenced by thermodynamic activity in the troposphere. This will be achieved creating a climatology of PVDs from a long reanalysis dataset using a modified version of the Hannachi et al. (2011) geometric moments technique. Then a spatial average is created for each PVD representing the average position of the disturbed polar vortex. That spatial average is used to average terms from a thermodynamic budget calculation throughout the troposphere and stratosphere on the days surrounding a PVD onset. The goal will be to understand the local thermodynamics response associated with the migrating polar vortex. Additionally, the relationship between PVDs and other large scale stratospheric phenomena is also examined, along with what, if any, impact these phenomena have on the PVDs thermal signatures. Final, a series of modelling experiments are performed with the goal of understanding how zonally asymmetric tropospheric temperature interact with surface wave forcing, in the form of topography, to influence the occurrence of PVDs. The specific question for this modelling work is: how does a temperature wave in the lower troposphere interact with surface topography to influence the polar vortex? This is done through specifically looking at the way vertical wave activity is modified. An idealized dry-core global circulation model (GCM) is used for these experiments. Chapter 2 will describe the data and model, along with all other computational methods, used in this research. The results of the research on the reanalysis dataset will be presented and discussed in Chapter 3. The results of the modelling experiments will be presented and discussed in Chapter 4. The conclusions of this work will be summarized in Chapter 5.

CHAPTER 2

DATA & METHODS

Reanalysis Data

The data used in this research is the Modern-Era Retrospective Analysis for Research and Applications version 2 (MERRA2) reanalysis dataset provided by the National Aeronautics and Space Administration (Gelaro et al. 2017). From this dataset, we have extracted daily averaged data for the years of 1980 to 2017, at 42 vertical levels from 1000 to 0.1 hPa, and a horizontal resolution of 0.625° in longitude and 0.5° in latitude over the Northern Hemisphere. Among other variables, the air temperature, geopotential height, horizontal and vertical winds, and Ertel's potential vorticity are provided. The data associated with each day are referred to by Day of Year (DOY), or days from 1 January, and the year given is the year of 1 January for that winter. Therefore, DOY 59 of 1996 and DOY -2 of 2005 represent 29 February 1996 and 30 December 2004, respectively.

CAM6 in CESM2

The modelling experiments in this research are performed using the Community Earth Systems Model version 2 (CESM2) provided by the National Center for Atmospheric Research (Lauritzen et al. 2018). This is a fully coupled global climate models that is comprised several different models focusing on specific aspect of the global system. The model applicable to this research is the Community Atmosphere Model version 6 (CAM6) which solves the hydrostatic Navier-Stokes equations in the Earth's atmosphere (Dennis et al. 2012). CAM6 actually includes several different dynamic cores which solve the physical equations using different numerical schemes. The dynamic core used in the work is the Eulerian dynamic core, using spectral methods based on spherical harmonics in the horizontal direction, and finite differencing in the vertical direction and with time. There are also a series of physical packages included in CAM6 that model subgrid scale processes like cloud formation, aerosols, ground-air exchange,

etc. All of these physics packages are turn off in this research. The model is run in a highly idealized configuration, first published by Held and Suarez (1994) for the purposes of intermodal comparison. The, heretofore called, Held-Suarez model is a dry planet global circulation model (GCM) with no additional physics except for momentum dampening at the surface to enforce the no-slip boundary condition. The only forcing in the model is a relaxation of the temperature field toward a zonally and hemispherically symmetric temperature field with a meridional temperature gradient from equator to pole and vertically decreasing temperatures up to the tropopause. This configuration is modified with the adjustments defined in Polvani and Kushner (2002) which modify the temperature forcing field by adding a basic stratosphere, designating a winter hemisphere, and including a cold winter stratospheric pole to induce a polar vortex. These Polvani-Kushner modifications also include a momentum sponge layer at the top of the model to prevent wave reflection.

The model is additionally modified to include a topography field, and zonally asymmetric perturbation in the temperature forcing. Both of these are added to the winter hemisphere, the northern hemisphere in all model runs, and both are defined by the following equation:

$$F(\lambda, \phi, P) = F_\lambda(\lambda) F_P(P) \sin^2\left(\frac{\phi - \phi_1}{\phi_2 - \phi_1}\right) \quad \text{for } \phi_1 < \phi < \phi_2 \quad (1)$$

where λ is longitude, ϕ is latitude, P is pressure, ϕ_1= 20°N and ϕ_2= 80°N. For the topography, represented as the surface geopotential

$$F_\lambda(\lambda) = \Phi_0[1 - \cos(m\lambda)] \text{ and } F_P(P) = 1 \quad (2)$$

where Φ_0= 10,000 or 7,500 m^2/s^2 giving a topographical peak of approximately 2 or 1.5 km at $\lambda = 180°$. For the temperature perturbations

$$F_\lambda(\lambda) = T_0 \cos(m\lambda + \lambda_0) \text{ and } F_P(P) = \sin^2\left[\ln\left(\frac{P}{P_1}\right) \Big/ \ln\left(\frac{P_2}{P_1}\right)\right] \text{ for } P > P_2 \quad (3)$$

where T_0 = 20K, P_2 = 300 hPa, and P_1 is approximately 2,408 hPa such that the maximum perturbation is at 850 hPa. Lastly, λ_0 is varied from 0° to 360° in sixteen 22.5° intervals. For all model runs in this research the zonal wave number, m, is equal to one.

The modified model was run with (1) no topography or temperature perturbation, (2) with only the topography, (3) with only the temperature perturbation, and (4) with topography and temperature perturbation for all values of λ_0. This gives a total of sixteen model runs outlined in Table 1. The model uses the T42 resolution which has 128 points in the longitude and 64 points in the latitude, along with 40 vertical levels. Each model run is ten years, or 3650 days, long and the first two hundred days are dismissed as the spin-up period, this requires 8.11 hours wallclock time using a single node with 36 cores which comes to 12.5 simulated days per core hour.

Topography	**Temperature Phase**
None	N/A
2 km	N/A
1.5 km	N/A
None	0°
2 km	-180°
2 km	-135°
2 km	-90°
2 km	-45°
2 km	0°
2 km	45°
2 km	90°
2 km	135°
1.5 km	-180°
1.5 km	-167.5°
1.5 km	-135°
1.5 km	-115.5°
1.5 km	-90°
1.5 km	-67.5°
1.5 km	-45°
1.5 km	-22.5°
1.5 km	0°
1.5 km	22.5°
1.5 km	45°

1.5 km	67.5°
1.5 km	90°
1.5 km	115.5°
1.5 km	135°
1.5 km	167.5°

Table 1: A brief description of the topography and temperature forcing utilized in each of the 28 model runs used in this research.

Geometric moments

The geometric moments method uses the statistical moments techniques to describe the geometric qualities of a 2-D dataset. The goal is to take moments with respect to spatial coordinates to fit a geometric shape, usually an ellipse, to the dataset. The methods used here for finding geometric moments are similar to those used by Waugh (1997), Hannachi et al. (2011), and Mitchell et al. (2013). Moments are taken of Ertel's potential vorticity (PV) field at 10 hPa that has been smoothed with a 3-day moving average to remove filament structures for all longitudes and latitudes from 30-90°N. The moment m is defined by

$$m_{kl} = \iint_{q \geq q_b} x^k y^l q(x,y) dx\, dy \quad (4)$$

where x and y are Cartesian spatial coordinates, k and l give the order of the moment, q is Ertel's potential vorticity (Haynes and McIntyre 1990), and q_b is an edge value. All data points are projected onto a Cartesian coordinate system with the North Pole centered at the origin. A unique value q_b is found for every day using a method described in Hannachi et al. (2011). The maximum in the PV field is located and set as a pseudo-pole in a new coordinate system. Derivatives are taken in the "meridional" direction within this new coordinate system. The maximum of this "up-slope" derivative is found (inflection point in PV field), and q_b is set to the PV value at that point. A plot of the q_b values for each winter season, and the climatology of q_b is presented in Figure 1. These edge values will increase in earlier winter and decrease in late winter with a peak around early February, but will generally stay around 4×10^{-4} $m^2s^{-1}K\ kg^{-1}$.

However, preceding PVDs the polar vortex tends to intensify and create sharper PV gradients causing q_b values to rise quickly. Then, as the vortex is distorted or breaks down, q_b values drop below average. This can cause q_b to experience a large temporal variability in a short time around the onset of a PVD, so a 30-day moving average filter is applied.

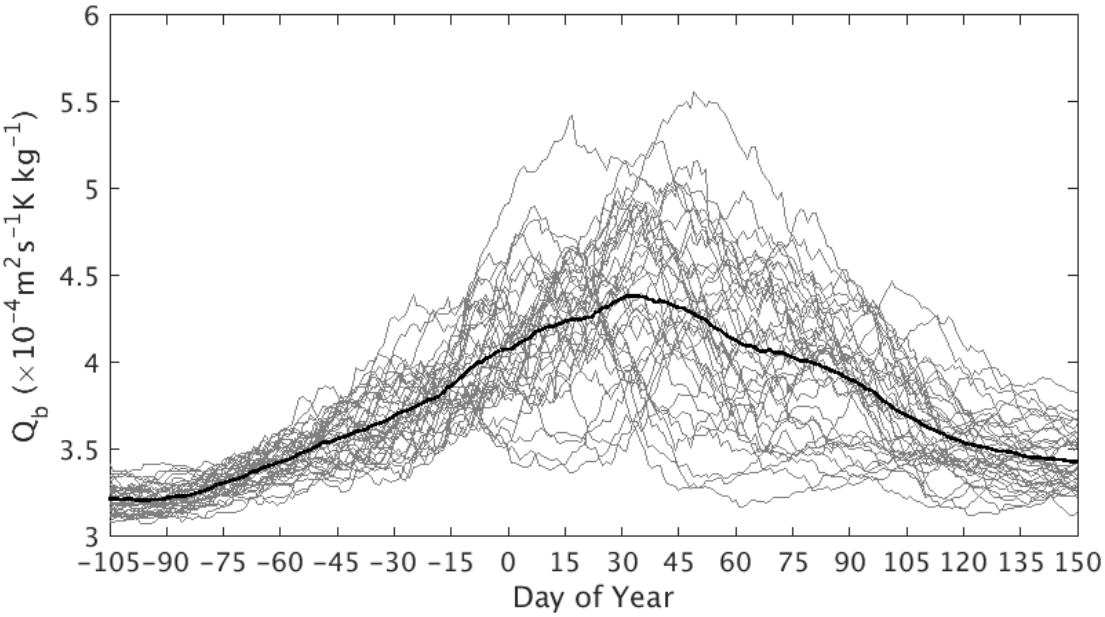

Figure 1: The value of q_b plotted as a function of day of year for each of the 37 years in the MERRA2 data (gray lines), and the mean value of q_b plotted as a function of day of year (bold black line).

The primary difference between the moments method used in this study compared to previous studies (e.g. Mitchell et al. 2013) is that moments are taken within closed contours separately, instead of taking moments of the entire PV field. This means that if the PV field on a particular day has two closed contours with value q_b then two separate moments will be calculated. This allows for identifying split vortices by comparing separate vortices instead of using aspect ratio as in Hannachi et al. (2011).

The 0^{th} and 1^{st} order moments are used in this study to provide information about the strength and centroid of each vortex, respectively. Higher order moments could also be taken to provide information such as aspect ratio, skewness, and kurtosis, but are not necessary for this analysis. The 0^{th} order geometric moment is usually referred to as the area, however in this instance an area integral of potential vorticity could more accurately be described as a circulation and is therefore used as a measure of the strength of a vortex. The contour with the largest 0^{th} order moment each day is the primary vortex. Any contour with a 0^{th} order moment less than 10% of the primary vortex on that day is dismissed as being insignificant; all other contours are heretofore called significant vortices. The 1^{st} order moments are used to calculate the centroid of each contour, which is analogous to a center of mass. The centroids are calculated according to

$$x_c = {}^{m_{10}}/_{m_{00}}, y_c = {}^{m_{01}}/_{m_{00}}. \quad (5)$$

Here the coordinates of the centroid for a particular contour are defined as (x_c,y_c). These coordinates are additionally converted into a centroid latitude and longitude.

The anticyclone analysis was done by taking geometric moments of the 10 hPa geopotential height field in the MERRA2 Reanalysis data. Equations (4) and (5) are used to calculate the size and centroid of every anticyclone in the high latitude stratosphere. The vortex edge value, q_b, for the anticyclone analysis is set as 31.2 km at all times. This value was chosen because it captures the Aleutian high in the winter climatology, but is sufficiently high is that there is no anticyclone on most days.

The geometric moments method used to track the polar vortex in the idealized GCM is based on the method described above and the method described in Seviour et al. (2013). The vortex edge is defined using the zonal mean of the geopotential height field at 68°N, the peak of the zonal jet, at 8 hPa. Similar to the Ehrmann and Colucci (2019) work, the vortex edge values are smoothed with a thirty-day sliding average, moments are taken within closed contours, separately. An area integral is calculated, and the zeroth and first order moments are taken to

find the centroid using equations (4) and (5). Additionally, the zeroth, first, and second order moments are calculated using the modified moments calculation:

$$J_{kl} = \iint_{q \geq q_b} (x - x_c)^k (y - y_c)^l q(x, y) dx\, dy \quad (6)$$

Using equation (6) the aspect ratio and orientation angle can be calculated using (Matthewman et al. 2009):

$$AR = \left| \frac{(J_{20} + J_{02}) + \sqrt{4{J_{11}}^2 + (J_{20} - J_{02})^2}}{(J_{20} + J_{02}) - \sqrt{4{J_{11}}^2 + (J_{20} - J_{02})^2}} \right|^{1/2} \quad (7)$$

and

$$\psi_e = \frac{1}{2} \tan^{-1} \left(\frac{2J_{11}}{J_{20} - J_{02}} \right). \quad (8)$$

With the aspect ratio and the orientation angle, in addition to the centroid and area, it is possible to complete an elliptical representation of the polar vortex. This analysis is performed on every day of all model runs.

Vortex events

There are three types of vortex events considered in this research: polar vortex disturbances (PVDs) in MERRA2, anticyclonic vortex episodes in MERRA2 i.e. Aleutian highs, and polar vortex displacements in the idealized GCM.

The value of q_b, along with the strength and centroid of each closed contour is calculated for the 10-hPa PV field on each day of the extended winter seasons of 1981-2017 in the MERRA2 dataset, where the extended winter season is defined as DOY -105 to 150 (approximately corresponding to 18 September to 30 May). This extended definition of winter allows us to study the full evolution of the vortices.

According to Hannachi et al. (2011) and many others, the polar vortex is known to experience disturbances of two separate kinds: either a displacement in which the polar vortex

migrates away from the pole, or a split whereby the polar vortex separates into two or more vortices of comparable size. A split is here defined to occur on any day when the ratio of the strengths of any secondary vortex to the primary vortex > 0.5, similar to the classification methods for SSWs used in Charlton and Polvani (2007). A displacement is defined as any vortex that is not a split when the centroid latitude of the largest vortex is equatorward of 70°N. Any day that is either a split or displacement is considered a disturbed day, while all other days are considered undisturbed days.

Also similar to Charlton and Polvani (2007), a polar vortex disturbance (PVD) event is defined by at least 3 consecutive disturbed days, with at least 15 consecutive undisturbed days between each PVD. The first disturbed day of a PVD is labeled the onset date of the event, and the time from the onset to the last disturbed day associated with an event is the duration of that event. These PVDs make no distinction between SSWs and final warmings.

The method used for identifying AH events is based on the definition in Harvey and Hitchman (1996), updated to incorporate more rigorous data processing techniques. Harvey and Hitchman (1996) required five criteria for an AH event: magnitude in a specific region, occurrence during the extended winter, spatial coverage, relative vorticity, and persistence in time. Our updated criteria for an AH event are as follows. The closed 31.2-km at 10 hPa must 1) have a centroid within 40°-80°N, 120°E-100°W, 2) occur during the period of 1 October to 31 March, 3) have with an areal extent greater than 1.84×10^6 km^2 (corresponding to 50° longitude by 10° latitude centered near 70^{o}N), and 4) persist for at least 5 days with 15 undisturbed days being necessary for a new event. Note that this classification neglects the relative vorticity criterion, although its inclusion would have had little effect on the results. The criteria also exclude anticyclones that migrate north of 80°N or form during April.

In the idealized GCM only wave 1 forcings are used so only displacement type disturbances occur. Because of this, only the centroid latitude of the main polar vortex contour is necessary to identify disturbances. To establish a threshold latitude for the centroid of a displaced polar

vortex the model run with only 2000m wave 1 topographic forcing is used. In the MERRA2 data approximately 10% of all the extended winter days have a displaced polar vortex. Therefore, a threshold latitude is chosen for the idealized GCM run such that approximately 10% of all days are displaced, specifically 78°N. This latitude is used as the threshold for defining a displaced vortex in all other model runs. A displaced event is then defined the same as a PVD, requiring three consecutive displaced days with fifteen undisturbed days needed before a new event.

PVD area averaging

For each day of a PVD, a new field is created in which grid points within the significant vortices are each assigned a value of one and all other points have a value of zero. These binary fields are then averaged together at each grid point on every disturbed day throughout the duration of the event. The result creates an area average that represents the position of the polar vortex throughout the PVD; a one in this field means the polar vortex is above that grid point every day of the event, a zero means the polar vortex in never above that grid point during the event, and a number between zero and one means the polar vortex is above that point for only a portion of the event. This grid point area average is used as a weighting for averaging derived quantities so that a single value can be obtained within the area into which the disturbed polar vortex moves. Figure 2 shows two examples of these filters: for a typical displaced PVD that begins on DOY 100 (11 April) in the winter season of 1993 and has a duration of 8 days, and for a typical split PVD that begins on DOY 84 (25 March) in the winter season of 2002 and has a duration of 21 days. The largest values for the displaced vortex (Figure 2a) are around the Eurasian region, and the largest values for the split vortex (Figure 2b) are around the Eurasian and North American regions. This indicates that, during these particular disturbance events, the disturbed polar vortex spent the largest amount of time around those regions.

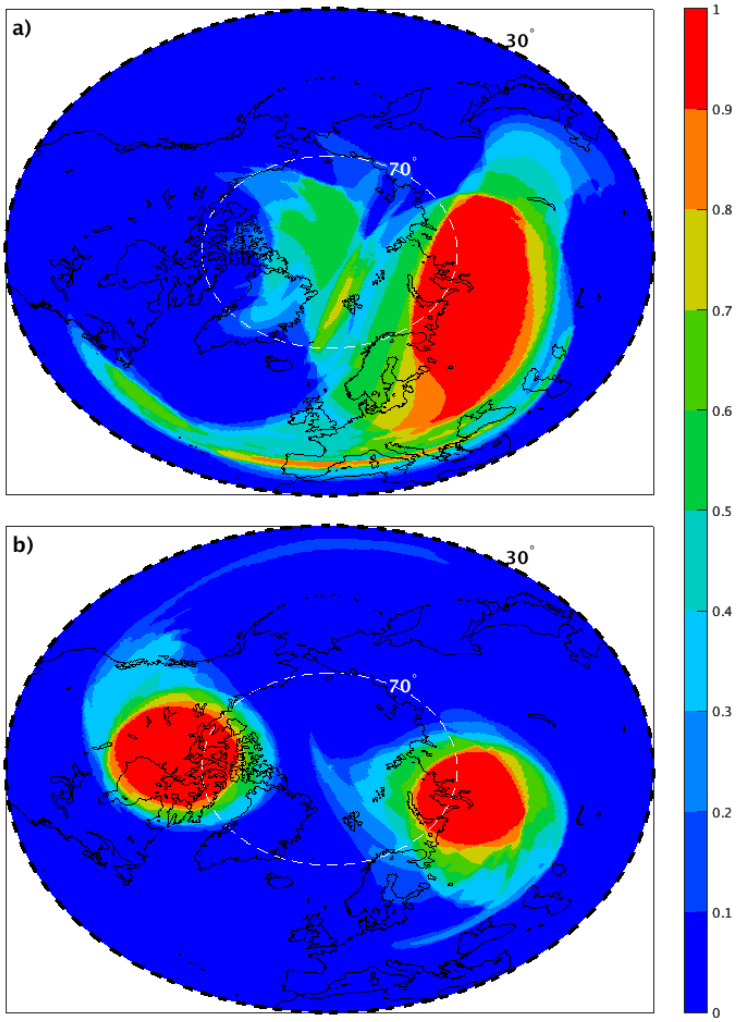

Figure 2: a) The area filter for the 8 days associated with the PVD starting on DOY 99 (10 Apr) during the winter of 1993. **b)** The area filter for the 21 days associated with the PVD starting on DOY 83 (25 Mar) during the winter of 2002. Contoured values are normalized by the number of disturbed days during the event, so a value of 1 would imply the vortex was over that point for every disturbed day of the event. Dashed black lines at 30°N and dashed white lines 70°N indicate the region over which the filter is applied.

The area averaging filters are used to weight only mid-latitude grid points, between 30-70°N, for each PVD, separately. Geopotential height and temperature tendencies and normalized

anomalies, as well as the thermodynamic energy budget calculations, are averaged on each isobaric level for the period stating 20 days before and ending 30 days after the onset of each PVD. This allows us to determine how these quantities vary vertically and with time over the region into which the polar vortex migrates for each PVD.

Thermal Budget Calculations

In order to better understand the thermodynamic processes associated with PVDs, a thermodynamic energy budget is calculated, based upon terms the following equation:

$$\frac{\partial T}{\partial t} = -\vec{V}_H \cdot \nabla_P T + \frac{1}{C_p}\frac{dh}{dt} + \frac{\omega P \sigma}{R_d} \quad (9)$$

Here T is the temperature, t is time, $\vec{V}_H$ is the horizontal wind velocity, ∇_P is the horizontal gradient on constant pressure (P) surfaces, C_p is the isobaric specific heat capacity, h is the diabatic heating rate per unit mass, $\omega = dP/dt$ is the pressure vertical speed, $\sigma = -{}^{R_d T}/_{P\theta}{}^{\partial\theta}/_{\partial P}$ is the static stability for potential temperature θ, and R_d is the dry gas constant. The left side of the equation represents the analyzed temperature tendencies, which are calculated as differences between the daily average temperature fields. The first term on the right side of the equation represents temperature changes associated with horizontal advection, calculated with centered finite differences, averaged over consecutive 24 h periods, and expressed in units of K day^{-1}. The second and third terms on the right side represent diabatic and adiabatic temperature changes, respectively.

Instantaneous, three-dimensional diabatic heating fields were unavailable in the MERRA2 dataset. In the absence of these heating fields, they are sometimes calculated as a residual of the other terms in (3), e.g. in studies of tropospheric cold-air outbreaks by Colucci et al. (1999) and Portis et al. (2006). However, we found these residually calculated diabatic temperature changes to be unrealistically large in our dataset, especially in the stratosphere. This led us to suspect the accuracy of the stratospheric vertical motion fields in the data. This same problem was

previously found in other reanalysis datasets by Wohltmann and Rex (2008) and Colucci (2010) who calculated vertical motion as a residual in (3) using diabatic heating rates from other sources. Rather than mixing datasets here, we have chosen to combine the adiabatic and diabatic terms in (3) into one term, calculated as a residual of the other terms (analyzed tendencies and horizontal advection). This follows the procedure of Konrad and Colucci (1989) in an earlier cold-air outbreak study. Because diabatic heating rates in the stratosphere are relatively small on the time scale of one day (e.g. Colucci 2010), we will assume that our thermodynamic residual represents mostly adiabatic temperature changes in the stratosphere, but it could well include diabatic processes in the troposphere. Resolution of the relative importance of diabatic versus adiabatic temperature changes during PVD evolution is beyond the scope of the present study and is left as a topic for future research.

Following the above procedure, the analyzed, advective and residual temperature tendencies were calculated everywhere in the Northern Hemisphere for the period starting twenty days before and ending thirty days after the onset of each PVD.

Potential Vorticity Inversion

Because the region into which the polar vortex migrates will experience isobaric geopotential height falls, it is of interest to understand the nature of these geopotential height tendencies. A form of potential vorticity inversion (PVI) was employed to relate the change in geopotential height over time to forcing from different layers of the atmosphere, in this case the stratosphere and troposphere as previously defined.

We begin with the definition of quasigeostrophic potential vorticity (QGPV)

$$q = \frac{g}{f_0}\nabla_p^2 Z + f + f_0 g \frac{\partial}{\partial P}\left[\frac{1}{\sigma}\frac{\partial Z}{\partial P}\right] = q_v + q_T, \quad (10)$$

where

$$q_v = \frac{g}{f_0}\nabla_p^2 Z + f = \eta_g \quad (11)$$

and

$$q_T = f_0 g \frac{\partial}{\partial P}\left[\frac{1}{\sigma}\frac{\partial Z}{\partial P}\right] = -R_d f_0 \frac{\partial}{\partial P}\left[\frac{T}{\sigma P}\right], \quad (12)$$

since from hydrostatic balance

$$\frac{\partial Z}{\partial P} = -\frac{R_d T}{P g}. \quad (13)$$

Here g is gravity, f_0 is a constant mid-latitude value of the Coriolis parameter (f), Z is geopotential height, σ is static stability, a function only of pressure (P) and time (t), η_g is the geostrophic absolute vorticity, R_d is the dry gas constant, and T is temperature. Equations (11), (12), and (13) are differentiated with respect to time, combined, and common terms are eliminated to yield

$$\left(\nabla_p^2 - \frac{{f_0}^2}{\sigma^2}\frac{\partial \sigma}{\partial P}\frac{\partial}{\partial P} + \frac{{f_0}^2}{\sigma}\frac{\partial^2}{\partial P^2}\right)\frac{\partial Z}{\partial t} = \frac{f_o}{g}\frac{\partial \eta_g}{\partial t} - \frac{R_d {f_0}^2}{g}\frac{\partial}{\partial P}\left(\frac{1}{\sigma P}\frac{\partial T}{\partial t}\right). \quad (14)$$

The right-hand side (RHS) of equation (14) is equal to the QGPV tendency plus a term involving the static stability tendency that is relatively small, especially in the stratosphere. Thus, the RHS of (14) is approximately equal to the QGPV tendency and will be referred to here as the PV forcing. Since we are interested in the role of tropospheric temperature tendencies in inducing stratospheric geopotential height tendencies we will use the RHS of (14) rather than replacing it with the approximate QGPV tendency. The RHS of (14) is calculated with ten-day differences in temperature and geostrophic absolute vorticity. The two terms on the RHS of (14) are then summed together to obtain a total forcing by the (approximate) QGPV tendency, although we will also attempt to isolate the effect of temperature tendencies.

Equation (14) is then solved for the height tendency field throughout the interior of the domain (within the lower and upper boundaries) due to the PV forcing (RHS) with successive relaxation by first guessing zero height tendencies everywhere, keeping them zero on the upper and lower boundaries, then iterating to a convergent solution. The impact of the PV forcing in one layer (troposphere or stratosphere) on the height tendency field throughout the domain was

isolated by setting the forcing function equal to zero in the other layer (stratosphere or troposphere) before numerical solution.

The PV forcing is not calculated on the lower and upper boundaries, 1000 hPa and 0.1 hPa respectively, whose contributions to the internal height tendencies are calculated separately. To calculate the contribution of each boundary, the PV forcing (RHS of equation 14) is set to zero, the height tendencies at the boundary are set equal to the analyzed height tendencies, and equation (14) is then solved for the induced height tendencies in the interior of the domain. Because of the large static stability in the upper stratosphere, the upper boundary height tendency does not produce a measurable effect at 10 hPa so it is not presented in this work. Note that grid points below the earth's surface are excluded from the MERRA dataset such that the lower boundary in some places is at a pressure level lower than 1000 hPa.

The boundary condition above differs from temperature advection or tendency conventionally used in PV inversions, although in our method the lower boundary temperature tendency influences the interior height tendency through the vertical derivative in the second term on the RHS of (14). Our calculation of the impact of the lower boundary height tendency (proportional to surface pressure tendency) on the interior height tendency is analogous to Mudryk and Kushner's (2011) study of the effect of surface pressure variations on internal annular mode variability. Otherwise, our PV inversion most closely resembles that of Bresky and Colucci (1996), adapted from Davis and Emanuel (1991), who calculate (Ertel's) PV tendencies from analyses and forecasts, then solve for the geopotential height tendencies throughout their domain due to the PV tendencies in two different layers of the troposphere. Note that our equation (14) is not strictly a statement of QGPV conservation since the tendencies on the RHS could be due to non-geostrophic processes in addition to geostrophic advection of QGPV. Thus, it yields inversion results that are more accurate than those from QGPV inversion while retaining its simplicity relative to Ertel's PV inversion.

Vertical Wave Activity Flux

The PVDs that are the focus of this work are known to be associated with increased fluxes of wave activity. So, for the modelling experiments, it will be useful to study the changes in the wave activity between model run to better understand the different responses of the polar vortex in each model. The formulas for calculating the three-dimensional wave activity flux were first derived by Plumb (1985). This was a generalization of the popular Eliassen-Palm (EP) wave flux (Edmon et al. 1980) which evaluates wave activity in the meridional and vertical directions. In fact, taking the zonal average of the Plumb wave activity flux gives the EP flux. Since the stratosphere is primarily driven by wave activity propagating vertically from the troposphere into the stratosphere, this research will focus on the vertical component of the wave activity flux (WAFz). The exact equation for WAFz is

$$WAFz = \frac{f}{S}\left[v'T' - \frac{1}{fa\cos\phi}\frac{\partial}{\partial\lambda}(T'\Phi')\right] \quad (15)$$

where f is the Coriolis parameter, a is the radius of the Earth, v is the meridional wind, T is the temperature, Φ is the geopotential (gz), and S is a modified stability term defined as

$$S = \frac{\partial\hat{T}}{\partial z} + \frac{R_d\hat{T}}{c_pH} \quad (16)$$

with H being a constant scale height. The apostrophe (T') represents the eddy term, or the difference from the zonal mean, and the hat ($\hat{T}$) represents the horizontal average.

The primary driver of WAFz both in sign and magnitude is the $v'T'$ term, often refered to as the eddy heat flux. This means warm air moving poleward and cold air moving equatorward are associated with upward (positive) WAFz, while cold air moving poleward and warm air moving equatorward are associated with downward (negative) WAFz. The WAFz is calculated on every day of all of the model runs. The top and bottom vertical levels are excluded from the calculation because of the vertical derivative in the static stability term in equation (15).

CHAPTER 3

REANALYSIS RESEARCH RESULTS & DISCUSSION

PVD Climatology

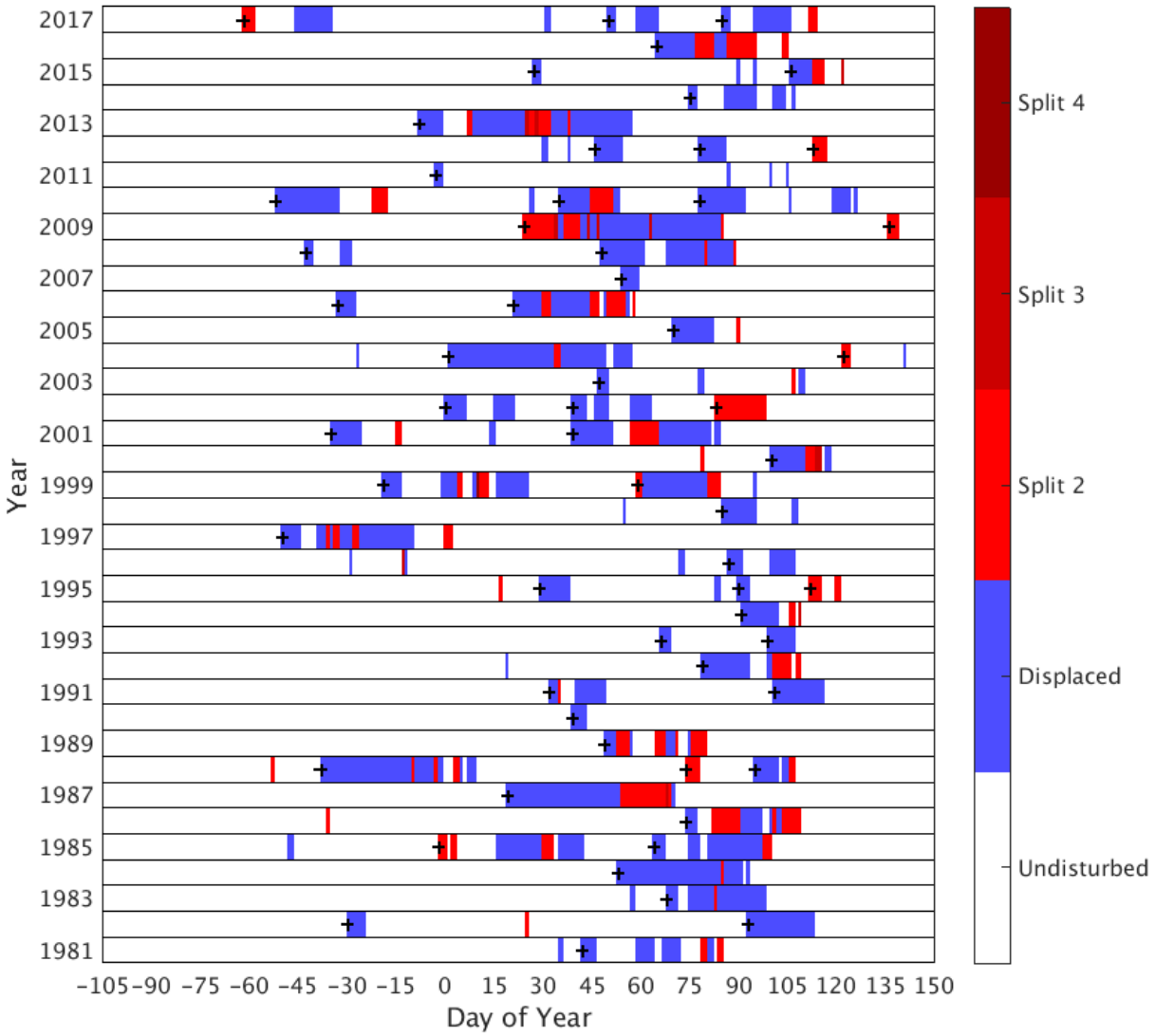

Figure 3: Classifications of the polar vortex are shown for each day of the extended winter season (DOY -105 to 150, or 18 Sept to 30 May) for all of the 37 winter seasons (1981 to 2017). White corresponds to an undisturbed vortex; blue corresponds to a displaced vortex; and red

corresponds to a split vortex. Darker reds indicate the vortex has split into more than two vortices. Black crosses indicate the onset day of polar vortex disturbance events.

The results of the geometric moments analysis are presented in Figure 3. Sixty PVDs were identified in 37 years for a rate of 1.62 events/year. The list of PVD events is presented in Table 2. This is comparable to the rate of disturbances found by Coughlin and Gray (2009) and, assuming one event each year is the final warming, it is also similar to the rate of SSWs found by Charlton and Polvani (2007). The average onset date for an event is DOY 46, or 16 February, and the average duration of an event is 23.8 days. Most events start with a displacement type disturbance then transition to a split, although events in early winter are more likely to remain a displacement. There are very few disturbances that begin with an immediate split of the polar vortex. The January 2009 PVD is the most notable example of a disturbance that begins immediately with a split. The average position of the polar vortex on all days with displaced vortices, and the average PV field of displacements are presented in Figure 4a and 4b, respectively. The average position of the polar vortex on all days with split vortices, and the average PV field of splits are presented in Figure 4c and 4d, respectively.

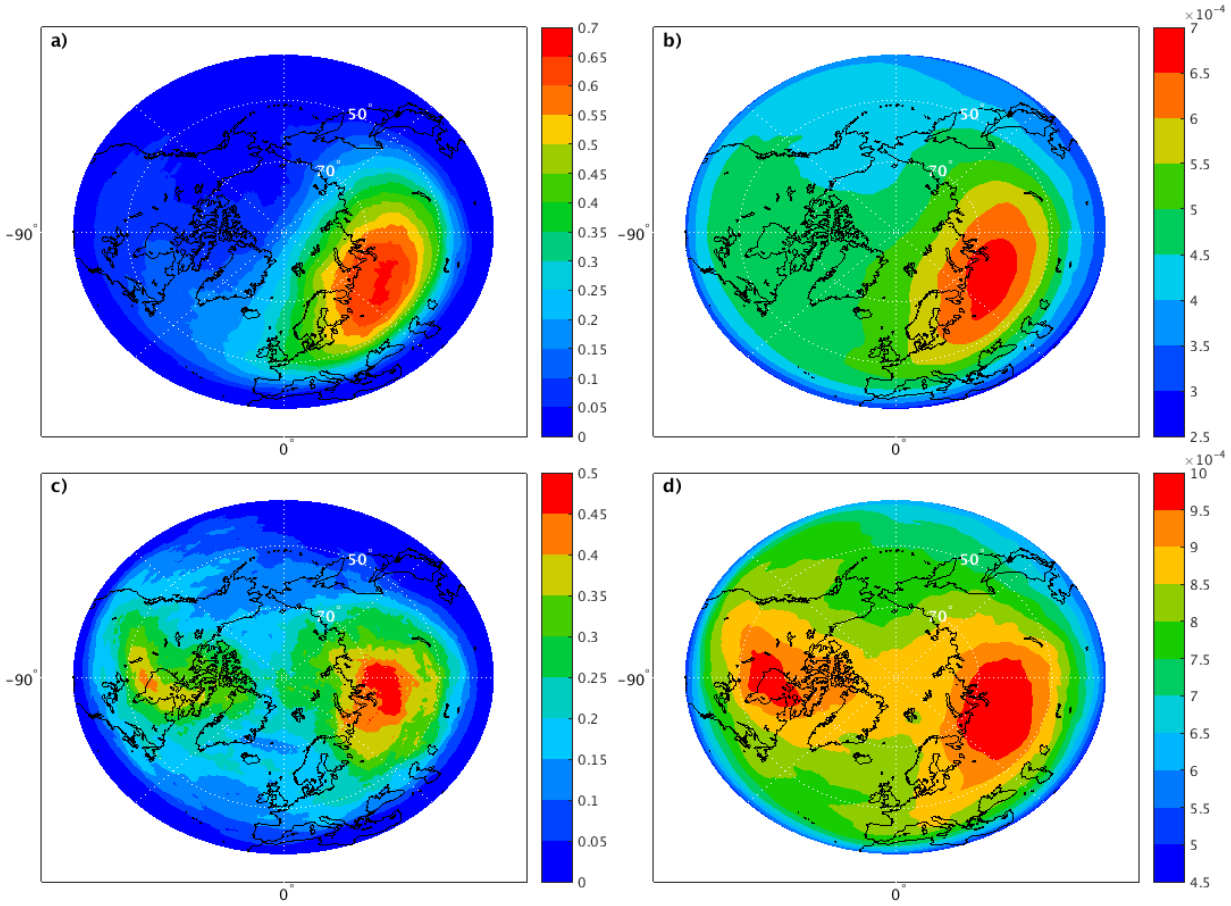

Figure 4: a) Average of area filters representing the average position of all 936 days with a displaced vortex during a PVD. **b)** Average PV field, in units of $m^2s^{-1}K\ kg^{-1}$, of a displaced vortex during a PVD. **c)** Average of area filters representing the average position of all 246 days with a split vortex during a PVD. **d)** Average PV field, in units of $m^2s^{-1}K\ kg^{-1}$, of a split vortex during a PVD. Longitude 90W is marked with -90^o and the Greenwich Meridian is marked with 0^o.

The PVDs presented in Table 2 are compared to the SSW compendium from Butler et al. (2017) and the list of vortex displacements and splits from Mitchell et al. (2013). All of the SSWs from the compendium are included in Table 2, although many more PVDs are found (shown in bold in Table 2). Most of these new PVDs are late winter final warmings; however,

there is a stretch of PVDs from 1990 to 1998 that are identified through our moments method but not through traditional SSW methods. There is much more agreement between the Table 2 events and the events from Mitchell et al. (2013). There are three events from their list missing from our PVDs: two split events (3 Jan 1986 and 13 Jan 1998) which are identified using elongation of the vortex instead of comparing separate vortices, and one displacement (12 Jan 1992) that is too brief to qualify as an event in our data. The PVDs that we identified but are not included in Mitchell et al. (2013) are marked in Table 2 with an asterisks. Many of these events are outside of the period they analyzed with the exception of four: 12 Feb 1981, 6 Mar 1985, 2 Feb 1991, and 8 Mar 1993.

Onset	Decay	Duration (Days)
12 Feb 1981*	27 Mar 1981	44
2 Dec 1981	7 Dec 1981	6
4 Apr 1982*	**24 Apr 1982**	**21**
10 Mar 1983	**9 Apr 1983**	**31**
23 Feb 1984	4 Apr 1984	41
30 Dec 1984	12 Feb 1985	45
6 Mar 1985*	**11 Apr 1985**	**37**
16 Mar 1986	**20 Apr 1986**	**36**
20 Jan 1987	12 Mar 1987	52
24 Nov 1987	10 Jan 1988	48
15 Mar 1988	19 Mar 1988	5
5 Apr 1988*	**17 Apr 1988**	**13**
19 Feb 1989	22 Mar 1989	32
9 Feb 1990	**13 Feb 1990**	**5**
2 Feb 1991*	**19 Feb 1991**	**18**
12 Apr 1991*	**27 Apr 1991**	**16**
20 Mar 1992	**19 Apr 1992**	**31**
8 Mar 1993*	**11 Mar 1993**	**4**
10 Apr 1993*	**18 Apr 1993**	**9**
2 Apr 1994*	**20 Apr 1994**	**19**
30 Jan 1995	**8 Feb 1995**	**10**
1 Apr 1995*	**4 Apr 1995**	**4**
23 Apr 1995*	**2 May 1995**	**10**
28 Mar 1996*	**17 Apr 1996**	**21**

12 Nov 1996*	**3 Jan 1997**	**53**
27 Mar 1998	**14 Apr 1998**	**24**
13 Dec 1998	26 Jan 1999	45
1 Mar 1999	6 Apr 1999	37
11 Apr 2000*	29 Apr 2000	19
27 Nov 2000*	**18 Dec 2000**	**22**
9 Feb 2001	26 Mar 2001	46
1 Jan 2002	22 Jan 2002	22
9 Feb 2002	5 Mar 2002	25
25 Mar 2002	**9 Apr 2002**	**16**
17 Feb 2003	20 Feb 2003	4
2 Jan 2004	27 Feb 2004	57
2 May 2004	**4 May 2004**	**3**
12 Mar 2005	**1 Apr 2005**	**21**
29 Nov 2005	**4 Dec 2005**	**6**
22 Jan 2006	18 Feb 2006	38
24 Feb 2007	1 Mar 2007	6
19 Nov 2007	**3 Dec 2007**	**15**
17 Feb 2008	30 Mar 2008	42
25 Jan 2009	27 Mar 2009	62
17 May 2009	**20 May 2009**	**4**
10 Nov 2009	**14 Dec 2009**	**35**
5 Feb 2010	23 Feb 2010	19
20 Mar 2010	7 May 2010	49
29 Dec 2010	**31 Dec 2010**	**3**
16 Feb 2012	**24 Feb 2012**	**9**
19 Mar 2012	**27 Mar 2012**	**9**
23 Apr 2012	**27 Apr 2012**	**5**
24 Dec 2012	27 Feb 2013	66
17 Mar 2014	**18 Apr 2014**	**33**
28 Jan 2015	**30 Jan 2015**	**3**
7 Apr 2015	**3 May 2015**	**17**
6 Mar 2016	**15 Apr 2016**	**41**
31 Oct 2016	**27 Nov 2016**	**28**
20 Feb 2017	**7 Mar 2017**	**16**
27 Mar 2017	**25 Apr 2017**	**30**

Table 2: The onset and decay dates of all identified PVDs. Bold PVDs were not identified by Butler et al. (2017)**,** and asterisks mark on the onset dates before 2002 that were not identified by Mitchell et al. (2013).

Throughout the 37 extended winter seasons, 12.91% of all days experienced some type of disturbance; 10.24% of all days were displacements and 2.67% of them were splits. This gives a split-displacement ratio of 0.26, a result of the fact that displacements are twice as common as splits and persist, on average, about twice as long. If a narrower perspective of the winter season is adopted, from mid-November (DOY -45) to late March (DOY 90), the likelihood of a disturbed day within a given winter becomes 18.98%, while the split-displacement ratio is unchanged. Of the sixty PVDs identified, thirty-seven (61.7%) contain at least one split day during their duration, and five of those events experience at least one day where the vortex is split into more than two separate vortices.

PVDs are often distinguished as being either a split vortex event or a displaced vortex event. The reality is that classifications are more complicated. From Figure 3 it is clear that a PVD being initiated by a split vortex is rare, with only ten such events in 37 years. However, more than half of the PVDs do have some split vortex days during the duration of the disturbance. A common scenario, especially in events beginning after 1 January, is a PVD being initiated as a displaced vortex then transitioning to a split vortex toward the end of its duration.

By averaging across all years, a seasonal climatology of vortex disturbances is found and presented in Figure 5. The probability of a disturbed vortex throughout the winter season is, unsurprisingly, dominated by the probability of a displaced vortex. Interestingly, this probability displays a clear bimodality with a peak in early December (DOY -29), a local minimum around 1 January (DOY 0), and a second peak in March (DOY 79). Split-type disturbances show a slow increase in occurrence through the early winter then, also, peak in late March (DOY 85). These findings are generally in agreement with the results of Charlton and Polvani (2007) who described split SSWs as being more likely to occur in late winter and displacement events having an even probability throughout the winter. The cause of the local minimum in disturbance probability around 1 January is not clear, nor does it appear in the results of Charlton and Polvani (2007).

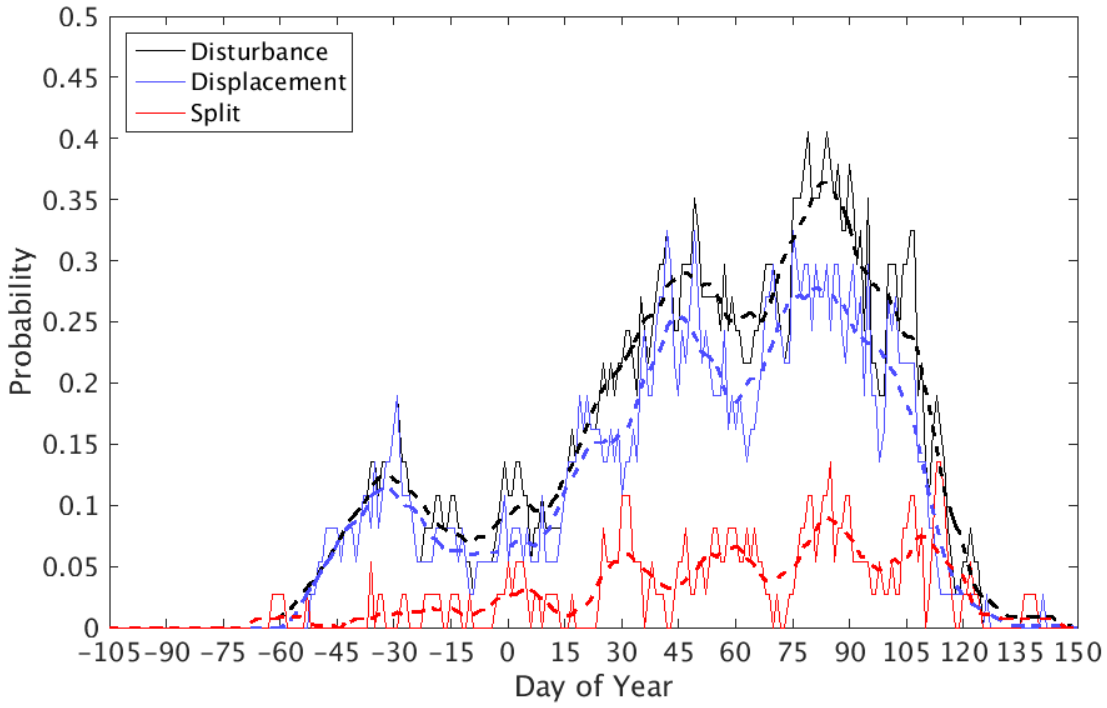

Figure 5: The probability of a disturbed vortex is shown as a function of day relative to 1 January (Day 0). Blue represents displacements, red represents splits, and black represents all disturbances (displacements and splits combined). The bold dashed lines show the values smoothed with a 5-day moving average.

The fraction of disturbed (as well as a displaced or split) days within a given winter is presented in Figure 6. Fractions are calculated by dividing the number of disturbed days each winter by the total number of days in the extended winter season. The number of PVDs each year is also shown in Figure 6 as gray bars. PVDs occur at a fairly consistent rate over the 37-year analysis; however, the number of disturbed days dramatically decreased during the 1990s. This is a result of PVDs during the 1990s tending to be shorter than PVDs in surrounding decades, as seen in Table 2. This lull in polar vortex disturbances in the 1990s is well documented (Charlton and Polvani 2007), but the lull was absent in some of the various methods tested in Butler et al. (2015). Therefore, it is worth noting that the lull is present in our analysis,

although the vortex did occasionally become disturbed during that time and, consistent with climatology, each year had at least one PVD. To test the statistical robustness of this lull a Monte Carlo distribution with 10,000 samples is used to compare the average percentage of disturbed days for the winters of 1990-1998 to the average of nine random years. A p-value of 0.015 is found for this period, meaning that the 1990s lull is statistically significant above the 95% level.

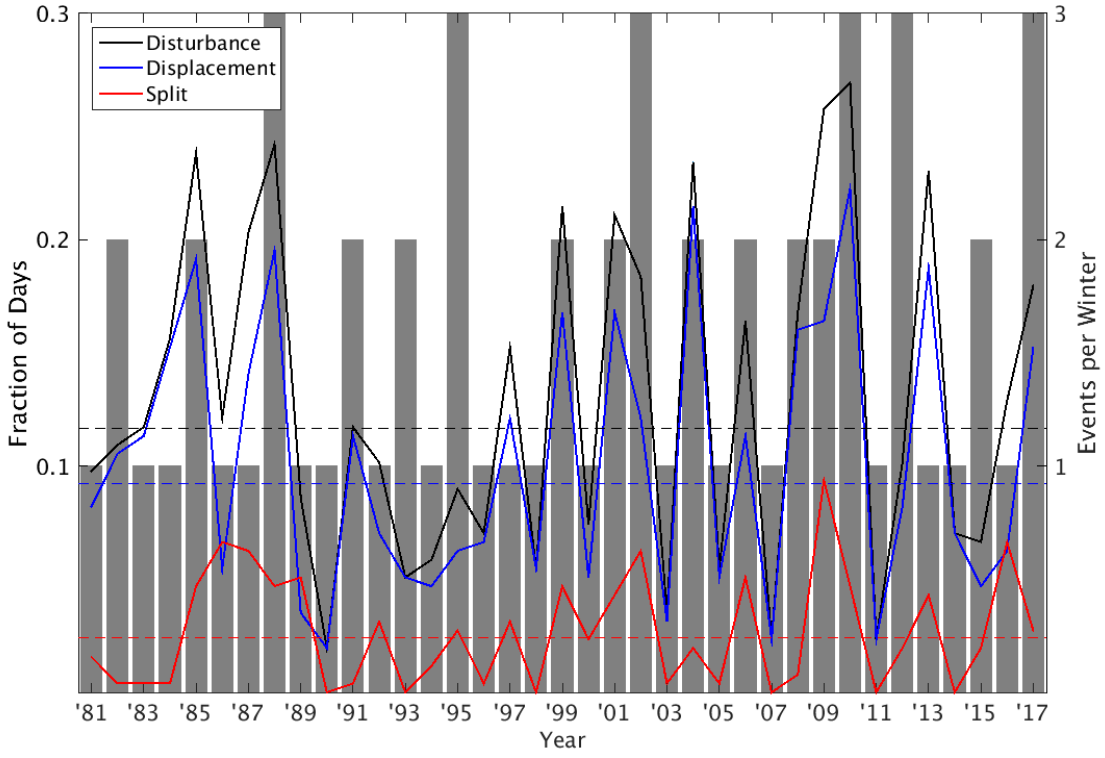

Figure 6: The frequency of a disturbed vortex (left ordinate) is shown as a function of year. As in Figure 4 blue represents displacements, red represents splits, and black represents all disturbances (displacements and splits combined). The dashed lines show the mean values for each of those three quantities. The gray bars represent the number of PVD events identified in each year (right ordinate).

Height & Temperature tendencies around PVDs

The composite of the geopotential height and temperature tendencies and anomalies for all sixty PVDs is presented in Figure 7. The onset of a PVD is associated with negative geopotential height anomalies throughout the lower and mid-stratosphere, peaking one day later. These height anomalies build with negative height tendencies for about 15 days before the onset, and decay with positive height tendencies for about 30 days after the onset. The peak in negative temperature anomalies occurs a few days after the onset of a PVD and exists throughout the lower stratosphere and upper troposphere. These cold anomalies build with cooling (negative temperature tendencies) for about 15 days before the onset, and decay (with positive temperature tendencies) for about 20 days after the onset. There is also a strong warm anomaly in the upper stratosphere, around 3 hPa, that peaks about 3 days after onset.

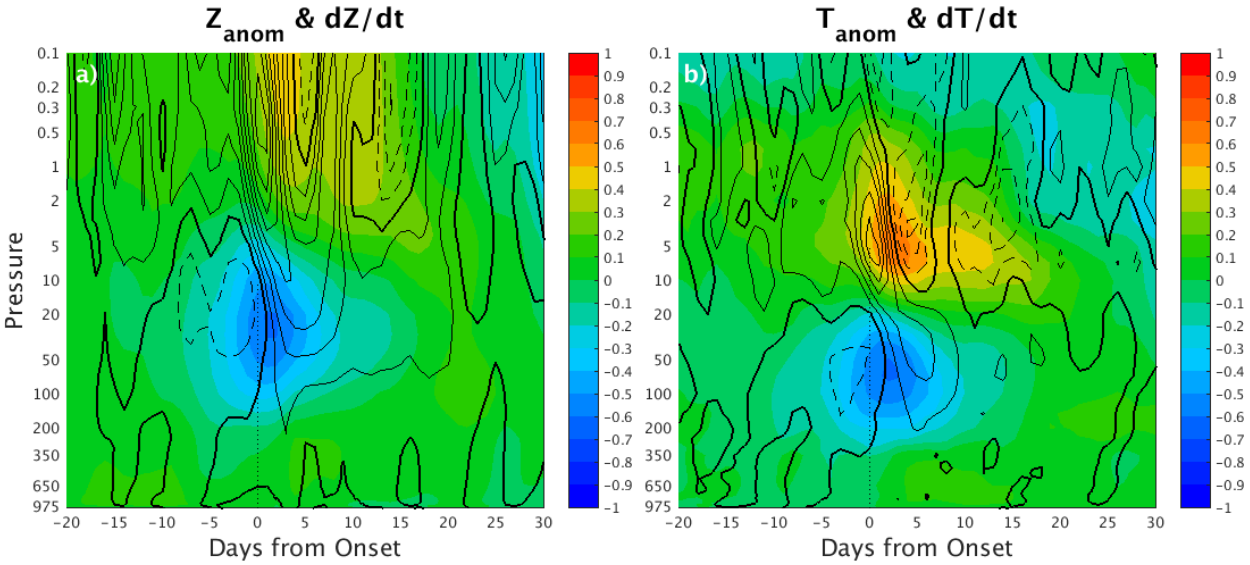

Figure 7: Composites of all 60 PVDs with the area filter associated with each event from 20 days before through 30 days after the onset. The vertical dotted line represents the onset. **a)** Normalized height anomalies in color, contoured at 0.1 standard deviation intervals. Analyzed

height tendencies (m/days) in black, contoured at 10 m/days intervals with the bold contour representing zero and dashed contours being negative. **b)** Normalized temperature anomalies in color, contoured at 0.1 standard deviation intervals. Analyzed temperature tendencies (K/days) in black, contoured at 0.5 K/days intervals with the bold contour representing zero and dashed contours being negative.

Figure 7 demonstrates the presence of the atmospheric cooling in the mid-latitude disturbance region and its colocation with geopotential height falls. For the weeks preceding the onset of PVDs, a cooling signal begins to intensify and permeate upward, reaching its largest magnitude within 5 days before the onset at approximately 50 hPa (Figure 7b). This suggests that cooling throughout the troposphere and lower stratosphere is related to height falls above those regions during the weeks before a PVD onset. The relationship between cooling and geopotential height falls is based on the hydrostatic assumption that the cooling of an air column is associated with a contraction of that air column and consequential geopotential height falls at the top of the column. This is evident by the fact that cold temperature anomalies and negative height anomalies peak at the same time with contraction occurring immediately above the cold region (Figure 7). Not visible in the temperature anomalies under the polar vortex (Figure 7b) is the downward propagation of cold air into the troposphere following the onset. This is not surprising since tropospheric cooling after a PVD is associated with changes in the meridional circulation and consequent spreading of the cold air away from the polar vortex (Yu et al. 2015b).

The composites of the thermodynamic energy budget terms for all sixty events are presented in Figure 8. Values below 99% statistical significance are removed from Figure 8. The null distribution is constructed by running a Monte Carlo simulation wherein random mid-latitude data points are averaged together from sixty random winter days. Rejecting the null hypothesis with 99% confidence means that these observed mid-latitude values surrounding the onset of

PVDs are, thus, unlikely to be independent of the PVD. Preceding the onset, the lower and middle stratosphere feature strong advective cooling, while at and after the onset the upper stratosphere features strong advective warming (Figure 8b). There is weak but significant advective warming in the troposphere throughout the duration and in the lower stratosphere after the onset. The troposphere also features residual cooling throughout the duration, with significant residual warming throughout the lower and middle stratosphere before the onset, and residual cooling after onset in the upper stratosphere (Figure 8c).

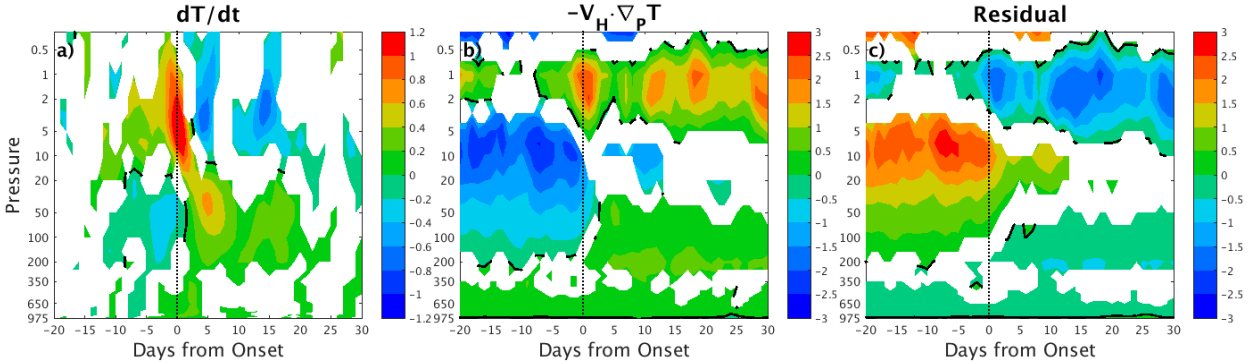

Figure 8: Composites of all 60 PVDs with the area filter associated with each event from 20 days before through 30 days after the onset. The vertical dotted line represents the onset. **a)** the analyzed temperature changes, **b)** the temperature changes from horizontal advection, and **c)** the residual temperature changes. All temperature changes in units of K/day. The zero contour is dark black and the color scale on each panel is unique. Values below 99% statistical significance are removed.

Horizontal advection of cold air in the stratosphere, preceding the onset of a PVD, is the defining feature in the composite thermodynamic energy budget over the mid-latitude region into which the polar vortex migrates (Figure 8b). This suggests that the lower and middle stratospheric cooling preceding PVD onset in Figures 7b and 8a is primarily driven by advective processes. This is supported by inspection of the mid-latitude thermodynamic energy budget for individual PVDs, such as that for the 10 Apr 1993 event (Figure 9) using the area averaging filter

for that event shown in Figure 2a. There is good agreement between the analyzed cooling and the advective cooling preceding the onset in the troposphere and lower stratosphere (Figure 9a,b).

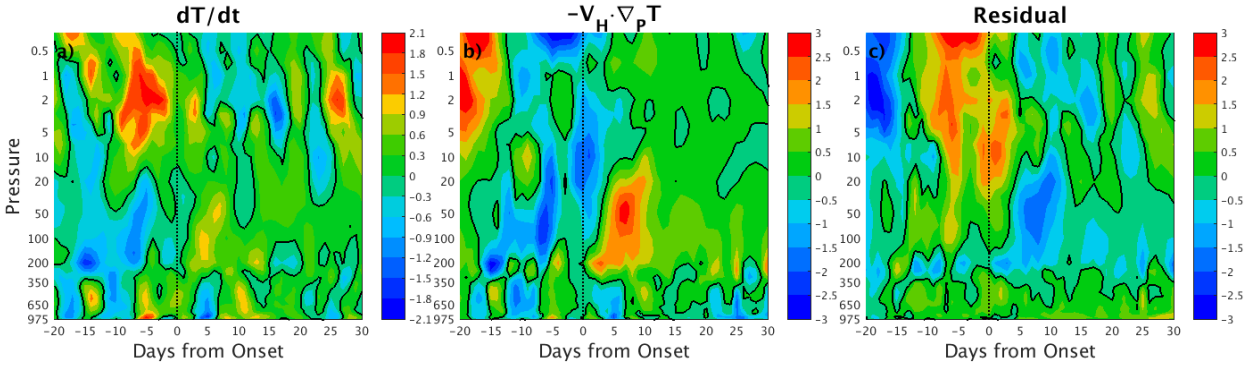

Figure 9: Thermodynamic energy budget values for the 10 Apr 1993 PVD averaged with the area filter associated with the event (Figure 1a) from 20 days before through 30 days after the onset. The vertical dotted line represents the onset. **a)** the analyzed temperature changes, **b)** the temperature changes from horizontal advection, **c)** the adiabatic temperature changes, and **d)** the residual temperature changes. All temperature changes in units of K/day.

The large stratospheric residual values in Figures 8c and 9c, opposite in sign to the advective temperature changes, suggest a near cancellation between advective and adiabatic temperature changes in the stratosphere. There is significant residual cooling, possibly associated with rising, adiabatically cooling air, in the troposphere both before and after PVD onset. This suggests that strong adiabatic cooling could be an important feature of the tropospheric mid-latitude region over which a disturbed polar vortex will migrate. The rising and adiabatically cooling tropospheric air could be a response to a vertically deep trough (Figure 7a), the stratospheric portion of which is being forced by advective cooling (Figure 8b). There is also strong residual (likely adiabatic) warming in the lower and mid-stratosphere preceding PVD onset, and strong residual (likely adiabatic) cooling in the upper stratosphere following PVD onset.

As previously noted, vertical wind data are available in the MERRA2 dataset; however, when adiabatic temperature changes were calculated using the available vertical winds, there were still large residual values, especially in the stratosphere, where vertical winds are very small in the MERRA2 dataset above 200 hPa. When adiabatic temperature changes are calculated using the available vertical wind data, they show good qualitative agreement with the residual temperature changes in Figure 8c, particularly in the troposphere. The stratospheric residuals, especially above 30 hPa, could include numerical errors due to the overestimations of the horizontal wind speed and therefore horizontal advection. This is based on the conclusions of Martineau et al. (2016) who showed dynamic inconsistency using residuals of the zonal-mean momentum equation. In their analysis, residuals become significantly large above 30 hPa owing, in the case of the first MERRA dataset, to errors in the parametrization of gravity wave drag. These same errors in the wind field could be the cause of an over estimation of horizontal advection contributing to high thermodynamic residuals in the upper stratosphere.

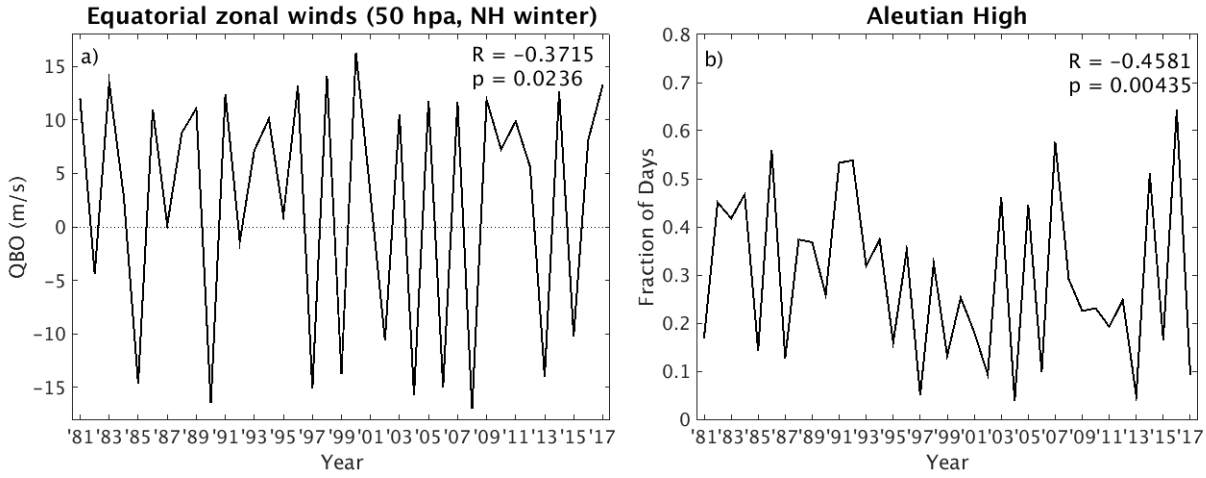

Figure 10: a) Equatorial zonal-mean zonal wind at 50 hPa averaged over the winter season (DJF) for each year representing the phase of the QBO. **b)** The fraction of days in the extended winter season (NDJFM) in which an AH is present. The correlation coefficient with the disturbance time series from Figure 5, along with the p-value of that correlation is in the upper right corner of each plot.

To represent the QBO in this work, the ZMZW at the equator at 50 hPa will be averaged over the winter season (DJF) so there is one wind value for each season. To represent the AH in this work, the AH days are averaged for each winter season to establish a fraction of days each winter in which the AH is present. The equatorial zonal wind at 50 hPa averaged throughout the Northern Hemisphere winter season is presented in Figure 10a, and the fraction of days with an AH present is presented in Figure 10b. The time series in both of these plots is compared to the fraction of PVD days in Figure 6. The correlation coefficient of both of these time series is negative: -0.37 for the QBO phase, and -0.50 for the AH days. The former is statistically significant above the 95% level, and the latter is statistically significant above the 99% level. Both of these relationships will be discussed further.

The negative correlation between the fraction of PVD days per winter (Figure 6) and the fraction of AH days (Figure 10b) is unexpected. The presence of the AH is associated with the PVDs; in fact, Colucci and Ehrmann (2018) showed that the time series of AH days is positively correlated with the time series of PVD days with a several week lag (AH onset precedes PVD onset). Nonetheless, years with more PVD days tend to have fewer AH days, and vice versa. The Colucci and Ehrmann (2018) definition of an AH requires the centroid of the stratospheric anticyclone to be located in a specific latitudinal and longitudinal region of the northern Pacific. Meanwhile, during a PVD, the anticyclone tends to migrate over the pole as the polar vortex breaks down. So, a PVD may be associated with a displaced anticyclone that no longer qualifies as an AH. Additionally, the AH appears in the climatology of the geopotential height field, implying an AH can persist while only slightly displacing an otherwise stable polar vortex. This is likely the cause for seasons with more AH days having fewer PVD days.

PVDs are divided into two groups based on whether or not they are preceded by an AH. Colucci and Ehrmann (2018) showed the AH days correlated positively with PVD days with a twenty to thirty-day lag. So here a PVD is defined as an AH PVD if there is an AH present for

five days in the period thirty-five to fifteen days before the onset of the PVD. All other events are defined as non-AH PVDs. There are thirty-one AH PVDs (51.7%) and twenty-nine non-AH PVDs (48.3%). The average position and average PV field for the AH PVDs are presented in Figure 11a and 11b, and the average for the non-AH PVDs are presented in Figure 11c and 11d. The average positions of the polar vortex in AH PVDs and non-AH PVDs (Figure 11) are generally similar. However, there is a higher percentage of split days in non-AH PVDs than there is in AH PVDs. This is evident in Figure 11c, in comparison to Figure 4c. In Figure 11c, there is a secondary peak in the average position of the polar vortex around 90°W. This suggests that a segment of the polar vortex is over the North American continent for about 25% of days associated with a non-AH PVD. The average vortex position during AH events shows that these PVDs feature fewer splits days, with Figure 11a resembling Figure 4a. In fact, the split-displacement ratio for AH PVDs is 0.24, and for non-AH PVDs it is 0.28. This is not surprising since the AH projects onto the stratosphere's wave 1 mode in the climatology, resembling displacement events.

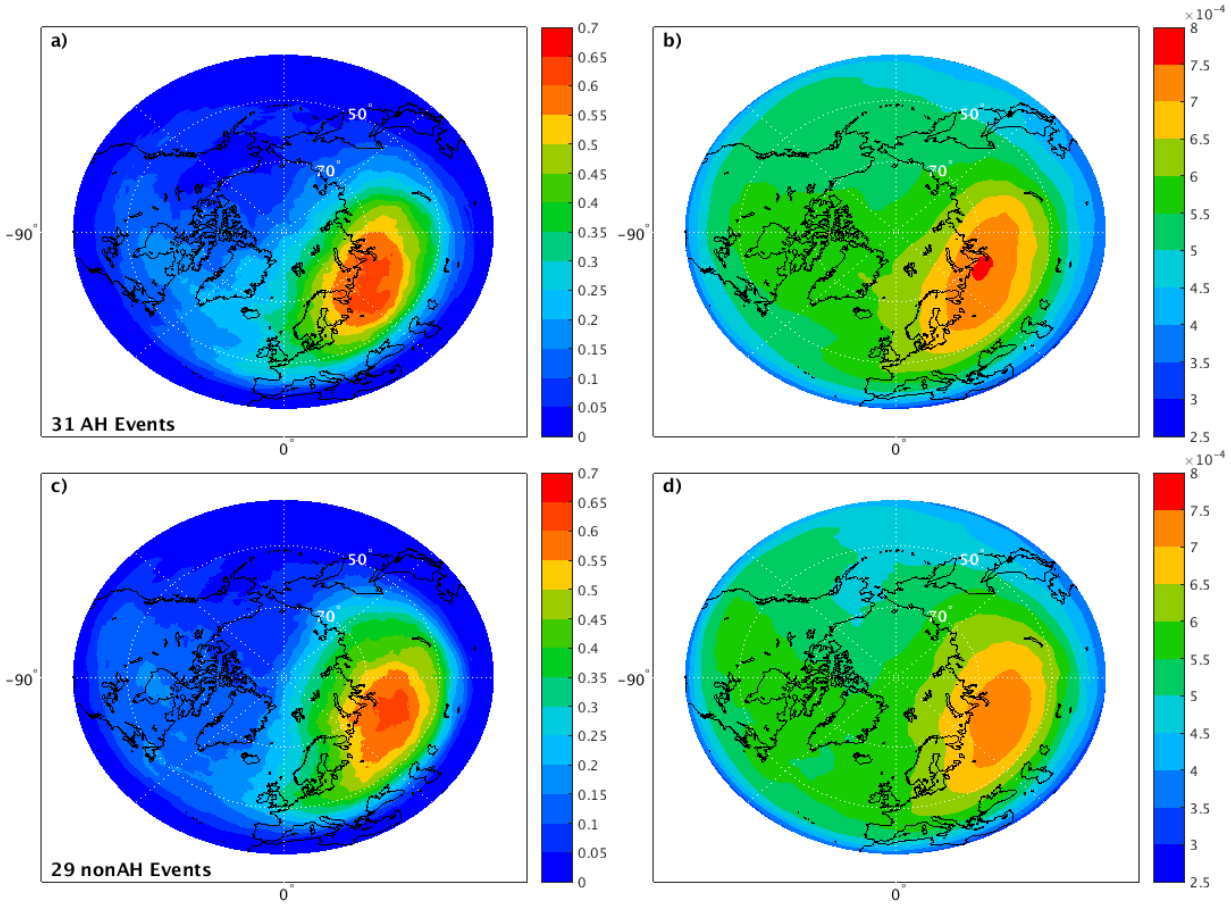

Figure 11: a) Area average representing the position of the polar vortex during AH PVDs. **b)** Average PV field, in units of $m^2s^{-1}K\ kg^{-1}$, of AH PVDs. **c)** Area average representing the position of the polar vortex during non-AH PVDs. **d)** Average PV field, in units of $m^2s^{-1}K\ kg^{-1}$, of a non-AH PVD. Longitude 90W is marked with -90^o and the Greenwich Meridian is marked with 0^o.

The thermodynamic energy budget terms under the disturbed polar vortex for the AH and non-AH PVDs are composited and are qualitatively similar to Figure 8 (not shown). The difference between the thermodynamic energy budget composites for the AH PVDs and non-AH PVDs is shown in Figure 12. Values above 99% and 95% statistical significance are contoured in dashed and solid white lines, respectively. The null distribution is constructed by running a

Monte Carlo simulation wherein each PVD is randomly assigned to one of two groups and the difference of the composites of those two groups is calculated. Rejecting the null hypothesis with 99% confidence means that the difference between these two groups is extremely unlikely to occur by randomly dividing the PVDs. Comparing the thermodynamic energy budget composited over AH PVDs and non-AH PVDs (Figure 12), it appears that the advective cooling associated with the AH is significantly stronger in the middle stratosphere, around 10 hPa, between five and zero days preceding PVD onset, and the residual (likely adiabatic) warming is significantly stronger in the same time and location. This implies that the mid-latitude cooling preceding the onset of AH PVDs is driven primarily by advective processes.

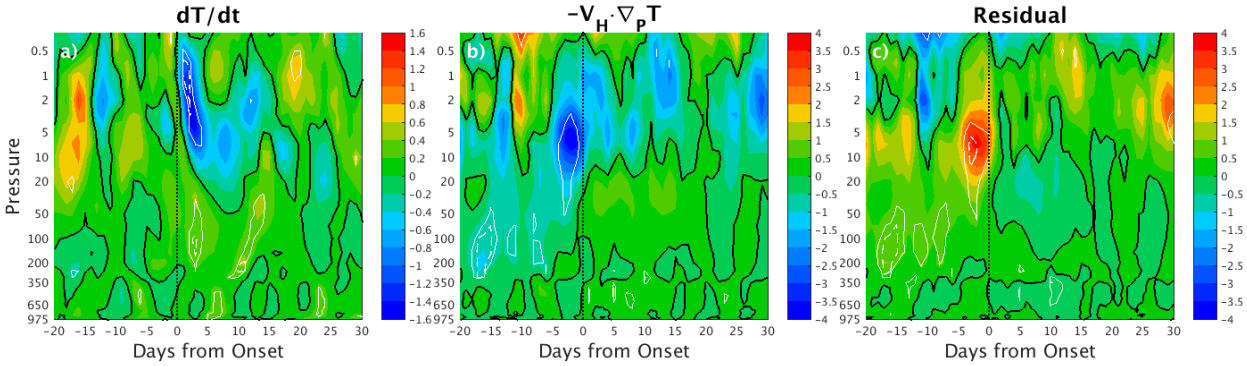

Figure 12: Composites of 31 AH PVDs minus composite of 29 non-AH PVDs. The vertical dotted line represents the onset. **a)** the analyzed temperature changes, **b)** the temperature changes from horizontal advection, and **c)** the residual temperature changes. All temperature changes in units of K/day. Values above 99% and 95% statistical significance are contoured in dashed and solid white lines, respectively.

The relationship between the fraction of PVD days (Figure 6), and the QBO phase (Figure 10a) is consistent with the current understanding of how the QBO effects the polar vortex. The mechanism connecting the polar vortex and the QBO is the Holton and Tan (1980) relationship. The relationship was confirmed by Watson and Gray (2014) using a GCM to show greater convergence of wave activity in the high latitude stratosphere, and decelerating westerlies in the

polar vortex when the model was nudged toward an easterly QBO phase. This mechanism is consistent with our observed correlation between the number of PVD days and the QBO phase where there are more PVD days during winters with an easterly QBO.

PVDs are also divided into two groups based on the phase of the QBO with twenty-one events during the twelve winters with an easterly phase of the QBO (QBOe), and thirty-nine events during the twenty-five winters with a westerly phase (QBOw). This gives a rate of 1.56 PVDs per QBOe winter, and 1.75 PVDs per QBOw winter. The average position and average PV field for the QBOe PVDs are presented in Figure 13a and 13b, and the average for the QBOw PVDs are presented in Figure 13c and 13d. The thermodynamic energy budgets for composites of QBOe and QBOw PVDs are also qualitatively similar to Figure 8 (not shown), and the difference between the thermal budget composites are shown in Figure 14 using the same null distribution as Figure 12.

The average position of the polar vortex for the twenty-one QBOe PVDs (Figure 13a) is spatially confined suggesting that these PVDs experience more consistent displacements into the Eurasian region. The average position for the thirty-nine QBOw PVDs is much broader, suggesting more split vortex days during QBOw PVDs, as well as displacements over a wider region, compared to QBOe PVDs. Comparing the thermodynamic energy budgets of QBOe PVDs to QBOw PVDs, it seems that the advective warming in the upper stratosphere, centered around 2 hPa, is significantly stronger during the fifteen to thirty days after the onset of QBOe PVDs (Figure 14). The difference in the residual (likely adiabatic) temperature changes is also mostly significant around 2 hPa between fifteen and thirty days after PVD onset, offsetting the enhanced advective warming for QBOe PVDs. All of this suggests that the easterly phase of the QBO enhances the PVDs' thermodynamic impact on the mid-latitude upper stratosphere for several weeks after the onset.

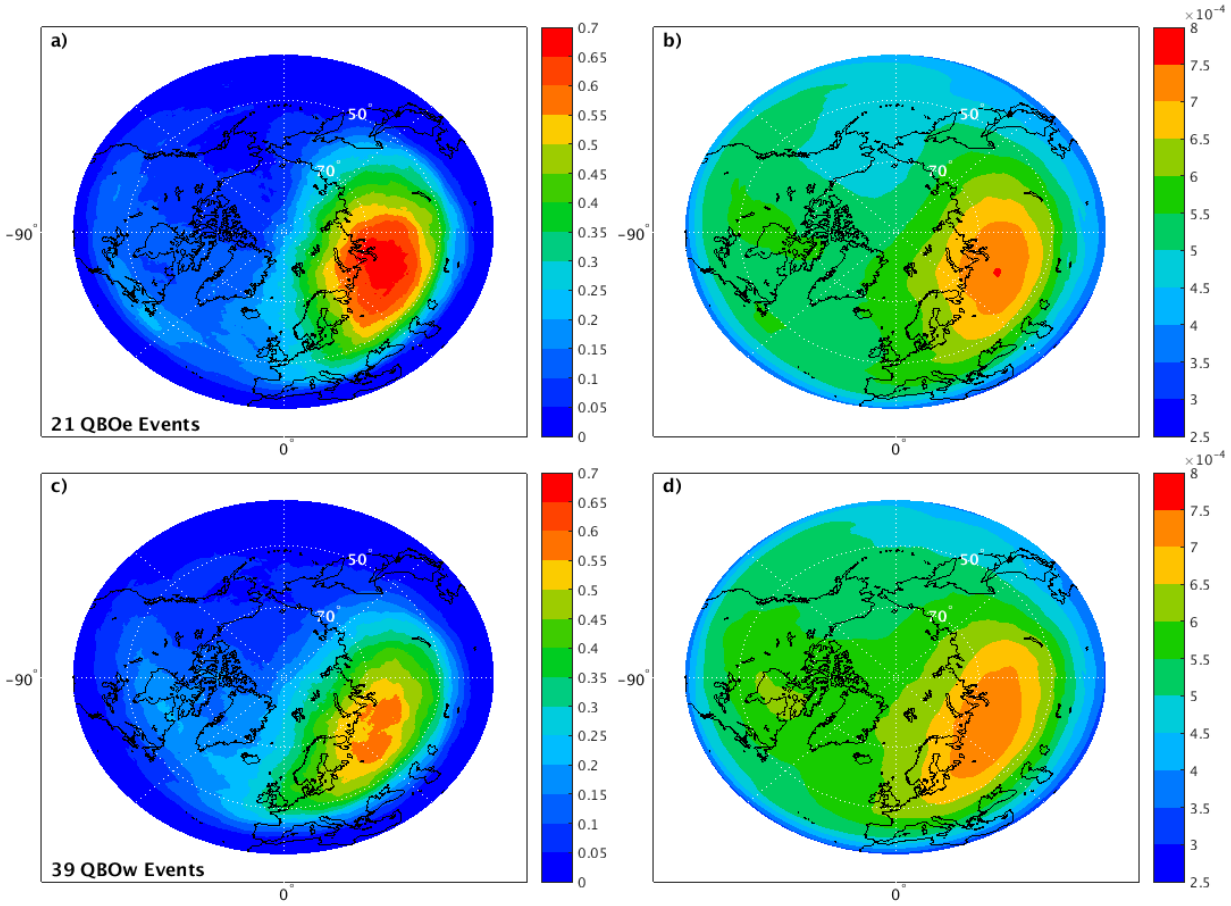

Figure 13: a) Area average representing the position of the polar vortex during a QBOe PVD. **b)** Average PV field, in units of $m^2s^{-1}K\ kg^{-1}$, of a QBOe PVD. **c)** Area average representing the position of the polar vortex during a QBOw PVD. **d)** Average PV field, in units of $m^2s^{-1}K\ kg^{-1}$, of a QBOw PVD. Longitude 90W is marked with -90^o and the Greenwich Meridian is marked with 0^o.

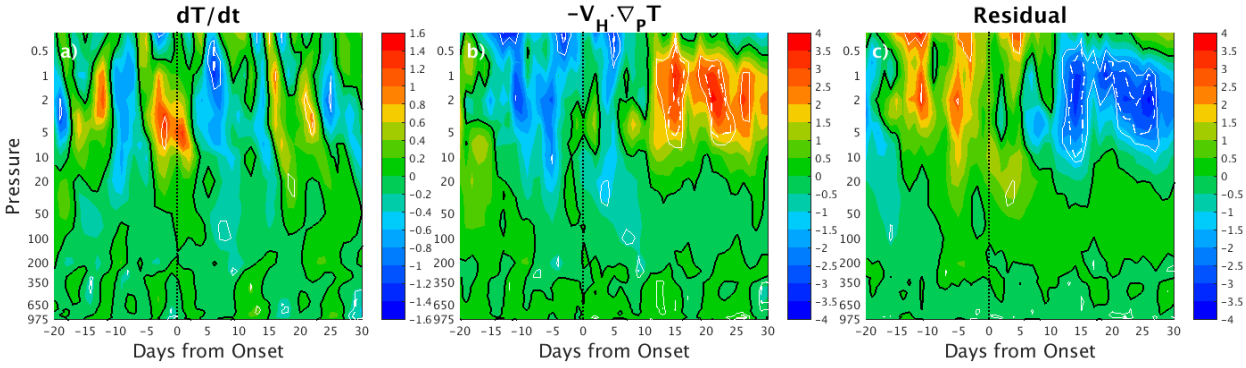

Figure 14: Composites of 21 QBOe PVDs minus composite of 39 QBOw PVDs. The vertical dotted line represents the onset. **a)** The analyzed temperature changes, **b)** the temperature changes from horizontal advection and **c)** the residual temperature changes. All temperature changes in units of K/day. Values above 99% and 95% statistical significance are contoured in dashed and solid white lines, respectively.

The biggest question raised by this work is: Can cooling in the mid-latitude region that spreads vertically through the troposphere through residual (likely upward, adiabatic) motion, and persists in the lower and middle stratosphere through horizontal temperature advection, cause contraction of the troposphere-stratosphere column local to that region to help cause a disturbed polar vortex to migrate above the region of cooling? To be clear, we are not suggesting that column contraction due to cooling is necessary to cause PVDs. Rather, this primarily advective cooling in the lower stratosphere may help drive the orientation of the polar vortex that is being disturbed. This topic will be investigated further in the modelling research.

Aleutian High

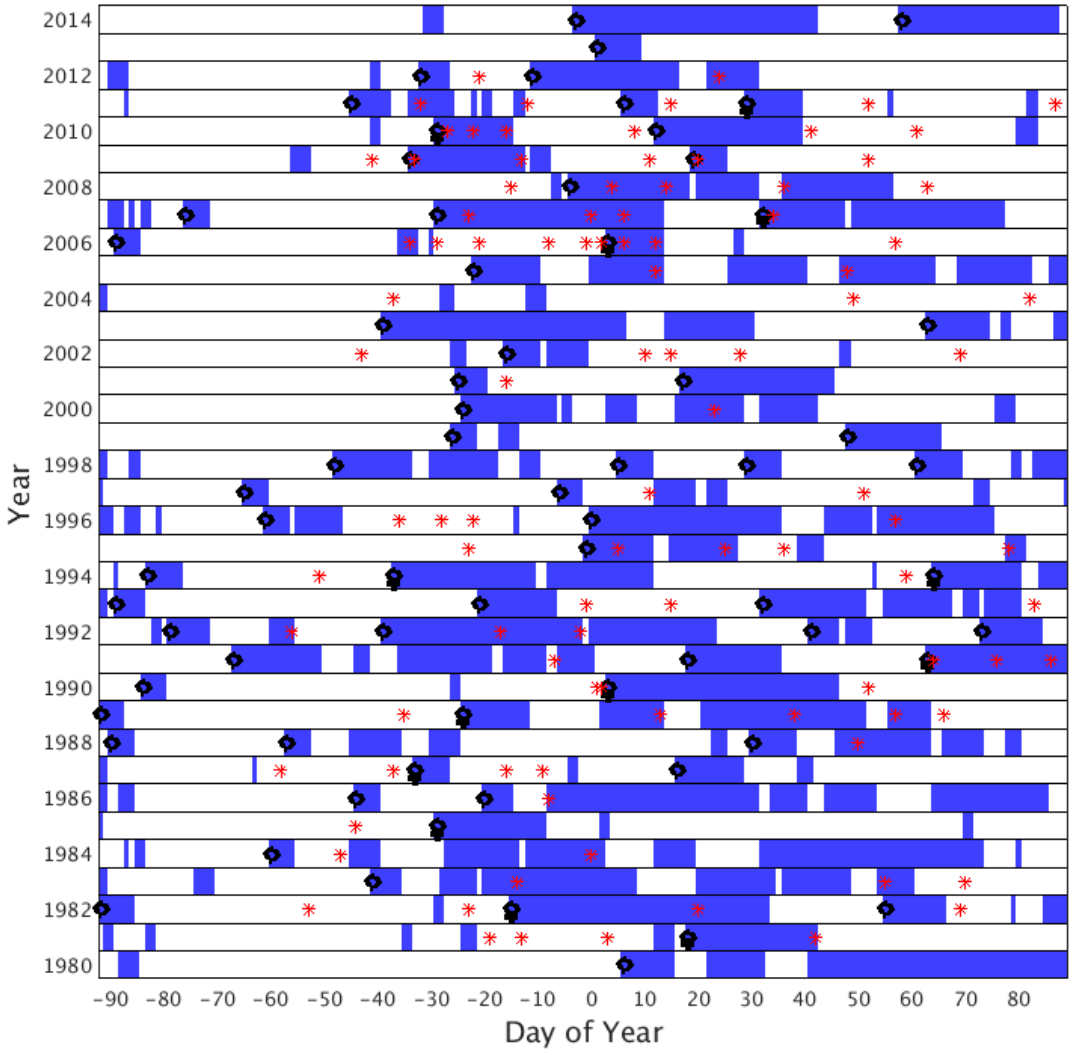

Figure 15: Days satisfying Aleutian High spatial criteria (blue shading) as a function of Day of Year relative to January 1 (Day 0) and the Year of that January 1. Each circle denotes the onset of an Aleutian High event, or a sequence of days satisfying both the spatial and temporal Aleutian High criteria. Each red asterisk marks a wave-breaking block onset within 100E – 80W. Each Aleutian High onset within day -15 and day +5 of a local block onset is marked with a cross beneath its circle.

The AH climatology is presented in Figure 15. Each day on which the AH spatial criteria are met is marked with blue shading; the onset of each event, satisfying the temporal criteria, is marked with a circle. We have identified 68 AH events in the 35 winter seasons for approximately two events per season. However, there were four events in each of two seasons (1992 and 1998) and no events in winter 2004. The average onset date for the first, second, third and fourth events in each season is 18 November, 1 January, 12 February and 7 March, respectively, and each event had an average duration of 32.6 days.

There is qualitative agreement between the AH events in Figure 15 and those identified by Harvey and Hitchman (1996) for a portion of the time period that we have studied. Our climatology has a fewer number of events because we require a 15-day gap between independent events.

Also marked on Figure 15 with red asterisks, are the onset dates of blocking events (from the CK climatology) that occurred within an extended AH domain (100 E eastward through 80W). If a block onset occurred within day -15 and day +5 relative to an AH onset (day 0), that AH onset is marked with a cross under its circle. Thus, there were thirteen AH events (out of 68) that temporally and spatially coincided with tropospheric blocking by the CK definition.

The CK blocking definition is adapted from Pelly and Hoskins' (2003) wave-breaking definition. Because the number of blocking events in a data set may depend upon the definition of blocking, we have also compared our AH climatology to a blocking climatology provided to us by R. Miller and G. Lackmann (hereafter ML; personal communication). In this climatology, blocking is defined by a modification of Dole and Gordon's (1983) persistent positive anomaly. Specifically, a positive anomaly at a grid point and time is defined by 500 hPa geopotential heights at a grid point exceeding two hemispherically averaged standard deviations at that time. Blocking is defined by a positive anomaly persisting for at least five days.

By this definition, in 41 of the 68 AH events, a blocking onset occurred within days -15 and +5 of an AH event. A correlation of AH days with blocking days revealed that, with 90% confidence, a statistically significant number of AH onsets coincided with a blocking event.

Finally, the AH climatology in Figure 15 is compared with the PVD climatology in Figure 16. Here the blue shading (AH days) from Figure 15 is overlain with shading on those days with a displaced (green) or split (red) polar vortex (Figure 3); the onset of each PVD event, satisfying temporal criteria, is marked with a cross. There were 55 PVD events in 35 winter seasons, or roughly three events every two winters.

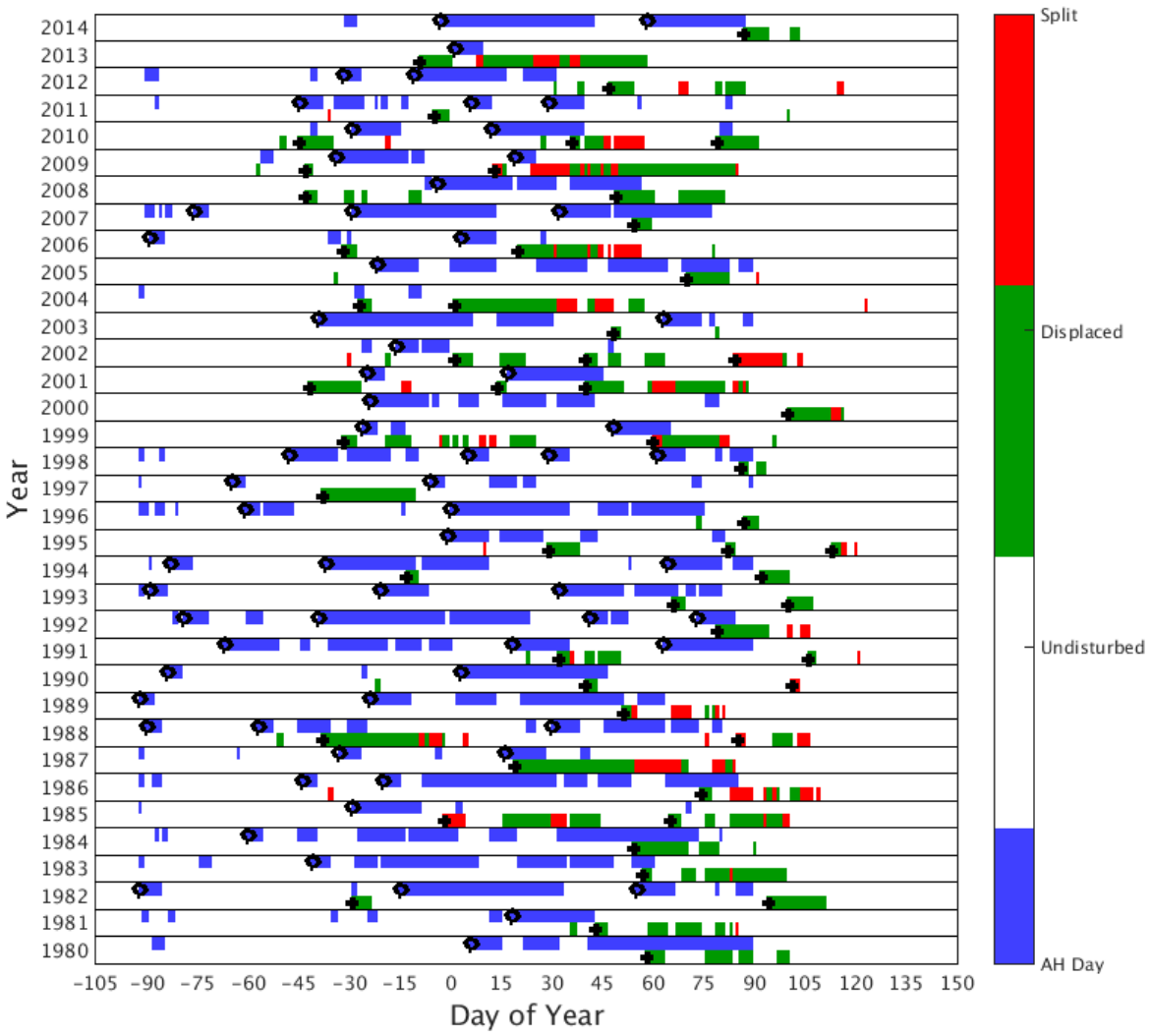

Figure 16: Each day with a displaced or split polar vortex marked with green or red shading respectively. The onset of each PVD is marked with a cross. The blue shading and black circles are as in Figure 15.

In 23 of the 68 AH events, PVD onset occurred within the AH event lifecycle (on or after AH onset and before or on AH decay, defined by the last day on which the AH event definition was satisfied), an average of 39.7 days after AH onset or on an average date of 17 February. For

comparison, these 23 AH events have an average duration of 51.2 days, longer than the 68-sample AH-event averaged duration of 32.6 days. Of the remaining 45 AH events, eighteen are each followed by a PVD event an average of 26.6 days after AH decay. Thus, 41 of 68 AH events each either coincided with or were followed by a PVD event. A lag correlation between AH days and PVD days in the sample reveals that AH days significantly (with 95% confidence) precede PVD days by 20 – 30 days, peaking around 25 days between an AH day and later PVD day.

Forty-seven of the 55 PVD events were each preceded by an AH onset, such that in almost all winters (33 out of 35), an early season AH was followed by a later season PVD. The exceptional winters are 2004, in which there were two PVDs but no AHs, and 2013 when a single PVD preceded a single AH. These particular events are not discussed in detail here, but are worthy of further investigation.

Analyzed and calculated geopotential height tendencies, averaged on each pressure level in the volume of air under the AH at onset (day 0) and composited over all 68 cases, are presented as a function of pressure and time relative to onset in Figure 17. There is very good qualitative agreement between the analyzed (Figure 17a) and total calculated (Figure 17b) height tendencies, with the latter slightly underestimating the former in magnitude. The height rises near AH onset and 10 hPa are almost entirely due to stratospheric PV changes (Figure 17d); these are statistically significant almost everywhere, including the troposphere. The downward influence of stratospheric PV changes on tropospheric geopotential height changes here is analogous to the downward propagation of anomalies from the stratosphere discussed by Kidston et al. (2015) and references therein. Interestingly, the lower boundary height tendency induces a small but insignificant contribution to the AH development (Figure 17e) while tropospheric PV changes oppose it (Figure 17). Tropospheric PV changes do induce significant height rises that extend into the stratosphere under the incipient AH near day -5 relative to AH onset, as well as

significant height rises in the troposphere and lower stratosphere after AH onset under this region.

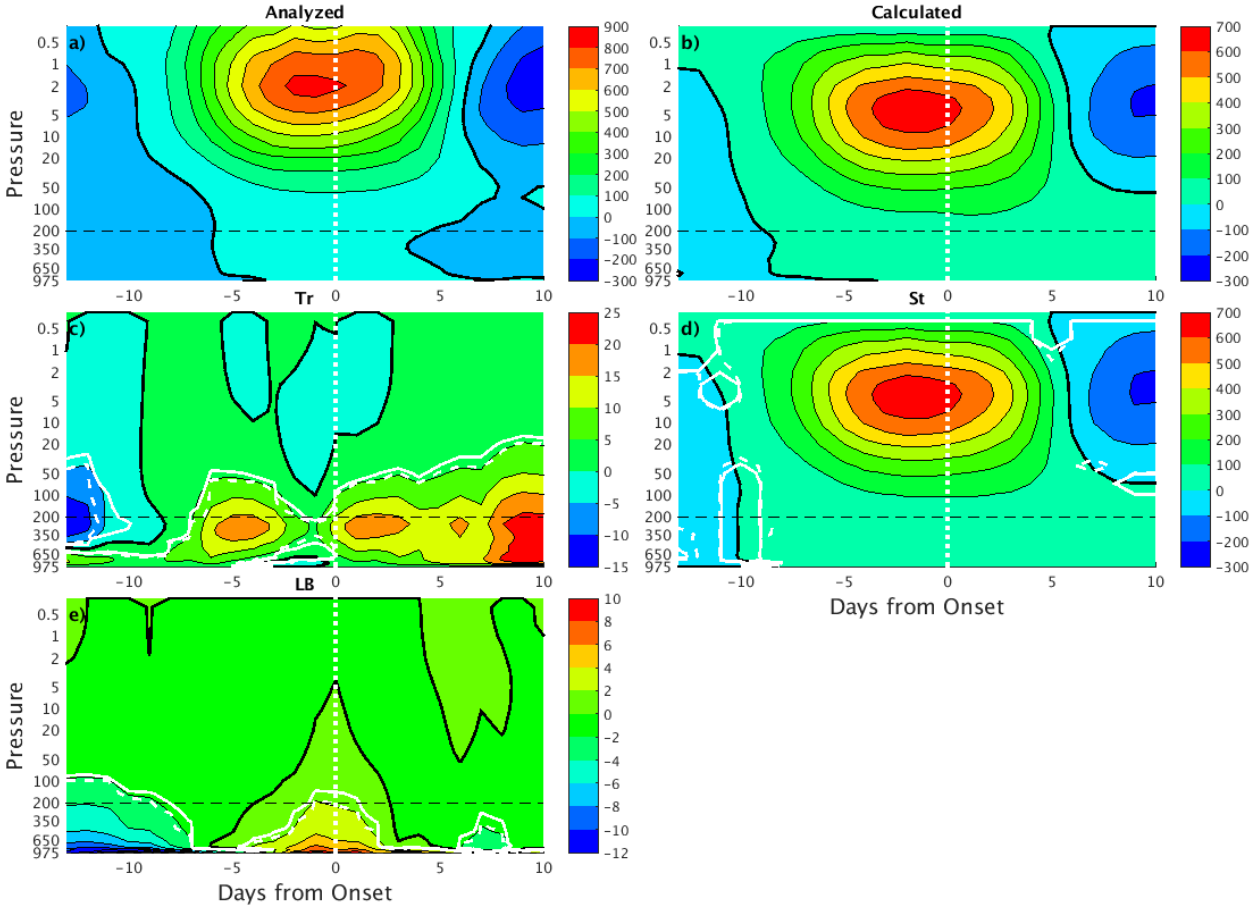

Figure 17: Geopotential height tendencies [m $(10d)^{-1}$] averaged over the area enclosed by each Aleutian High at its onset and composited over all 68 Aleutian High cases as a function of Days from Onset (Day 0) and Pressure (hPa): (a) height tendencies calculated directly from the analyzed geopotential heights, (b) Sum total of height tendencies calculated from all forcing and boundaries, (c) height tendencies due to potential vorticity changes in the troposphere, (d) height tendencies due to potential vorticity changes in the stratosphere, and (e) height tendencies due to the height changes at the lower boundary pressure level. The contour interval is 100 m $(10d)^{-1}$ in panels (a), (b) and (d), 5 m $(10d)^{-1}$ in panel (c), and 2 m $(10d)^{-1}$ in panel (e). The bold dark

contour is zero. Areas within solid and dashed white curves denote 95% and 99% significance, respectively, while the vertical dotted white line is Day 0.

This general picture does not change much if we restrict the composites to just those 13 AH cases coinciding with local tropospheric blocking by the persistent anomaly definition (Figure 25); stratospheric PV changes still largely account for the stratospheric geopotential height tendencies near AH onset. These stratospherically induced height rises extend significantly downward into the troposphere. Tropospheric and lower stratospheric height rises due to tropospheric anticyclonic PV increases under the AH are slightly reduced (enhanced) before (after) AH onset. Interestingly, there are the significant height falls in the troposphere and lower stratosphere due to tropospheric cyclonic PV increases about ten days prior to AH onset. There is even a significant contribution to height falls, extending into the stratosphere, from lower boundary height falls before day -10. This suggests that tropospheric cyclogenesis at the location of the incipient AH might be a precursor to AH onset coincident with local blocking. The connection between tropospheric cyclogenesis and tropospheric blocking is well known (e.g. Colucci 1985), but there is not a direct connection between the tropospheric cyclogenesis and the AH development apparent in Figure 18. The composited height tendencies in Figure 18 are qualitatively similar to those constructed from the 41 AH events associated with blocking by the ML definition, but are weaker in magnitude (figure not shown).

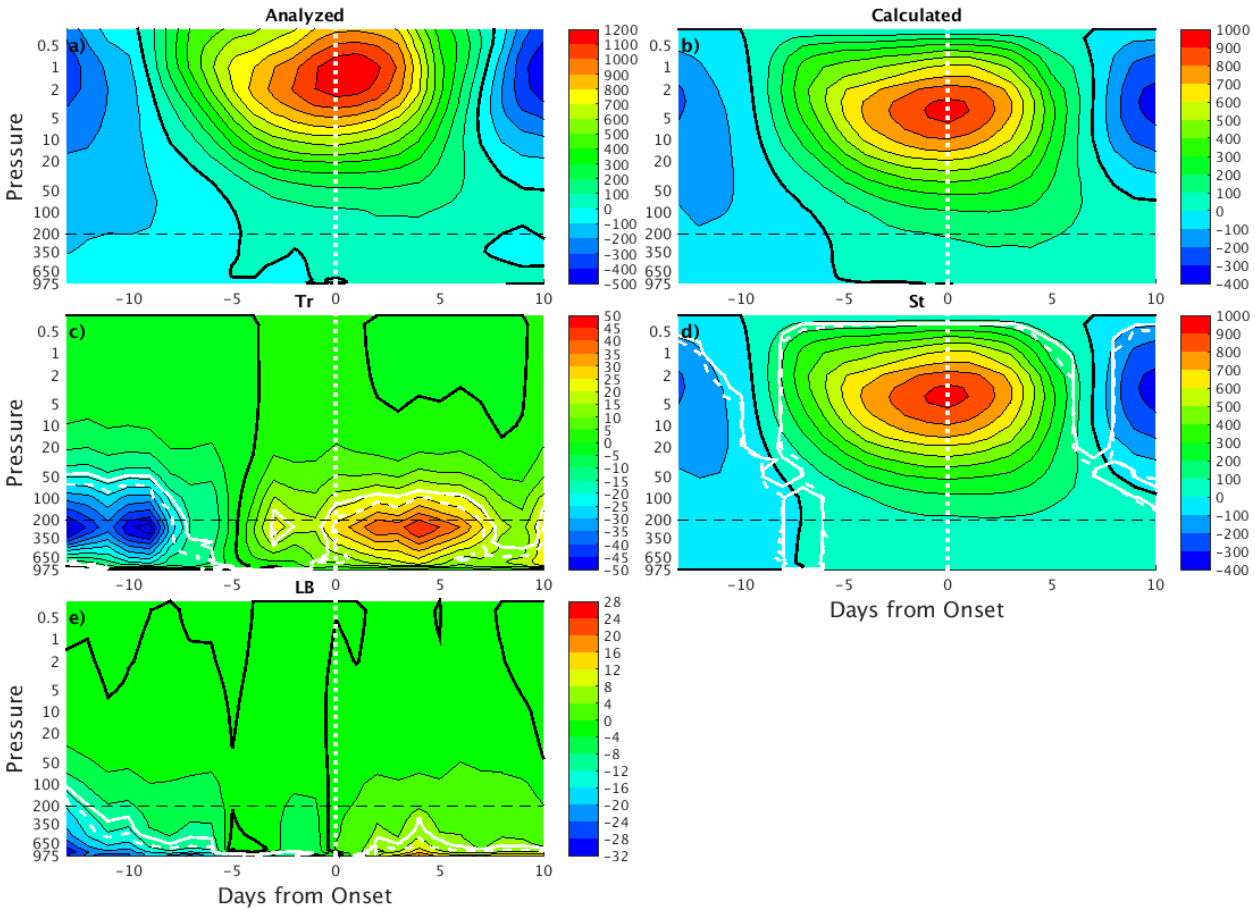

Figure 18: As in Figure 17, but composited over the 13 Aleutian High cases coinciding with local blocking, determined from a wave-breaking definition and that the contour interval is 4 m $(10d)^{-1}$ in panel (e).

The composited analyzed and calculated geopotential height tendencies during AH decay are presented in Figure 19. The analyzed, total calculated and stratospherically forced height tendencies appear to be opposite those during AH onset (compare Figure 19a, 19b, and 19d with Figure 17a, 17b, 17d, respectively). However, the maximum height changes near 10 hPa immediately follow AH decay, but immediately precede AH onset. There is a striking difference in the tropospherically forced height tendencies during AH decay (Figure 19c) relative to AH onset (Figure 17c). During AH decay, cyclonic PV changes in the troposphere induce significant

height falls all the way to 10 hPa. We will interpret these features in light of heat flux composites in the next section.

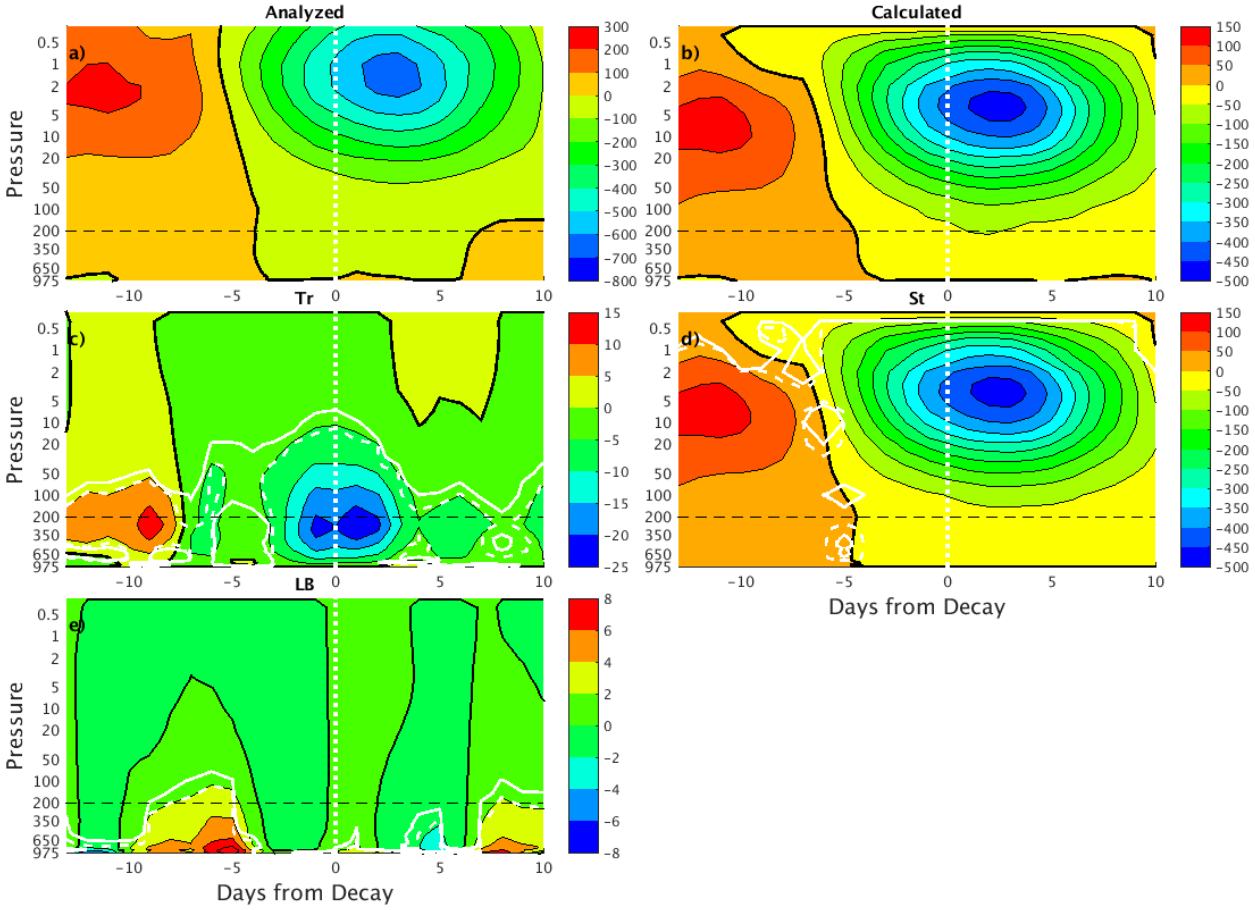

Figure 19: As in Figure 17, but composited over all 68 Aleutian High cases as a function of days from Decay (Day 0) and that the contour interval is 50 m $(10d)^{-1}$ in panels (b) and (d).

Like in the AH/blocking composites (Figure 17), the most prominent tropospheric signal in the height tendency fields is tropospherically forced height rises extending into the stratosphere after AH onset (Figure 17c). There are lower boundary-induced height falls in the lower troposphere near day -20 (Figure 17e), associated with an intense surface cyclone over the northwestern Pacific Ocean (not shown). However, there are no tropospherically forced height rises near 10 hPa prior to AH onset, suggesting that this case, as in the composites, was primarily

forced by stratospheric PV changes. Geopotential height falls are evident at all levels in all panels by Day 30 (2 January 1985), just prior to the decay of this AH event two days later and consistent with features in the composites of AH Decays (Figure 19), except that maximum height falls occur before (after) decay in this case (the composites).

Considering that AH development in idealized models has been attributed to an "upward burrowing" of anticyclones from the troposphere (O'Neill and Pope 1988), and that there were a significant number of AH onsets in our sample coinciding with persistently positive geopotential height anomalies in the troposphere, the absence of a tropospheric forcing of AH onsets in our geopotential height tendency diagnostics is a surprise. Our finding that the geopotential height rises associated with AH onset are forced primarily by stratospheric, not tropospheric, anticyclonic PV increases can be reconciled with the upward burrowing concept as follows. The stratospheric anticyclonic PV increases could be due in part to warm-air advection or poleward eddy heat fluxes. A time-pressure plot of meridional eddy heat fluxes (Figure 20) indeed reveals increasing eddy heat fluxes near 20 hPa leading up to AH onset. These eddy heat fluxes represent upward wave propagation, possibly from the troposphere or at least the lower stratosphere, toward the 10-hPa level. Thus, although we do not find evidence for a direct tropospheric forcing on AH development, there is indirect evidence for upward wave propagation from the troposphere in the heat flux plot.

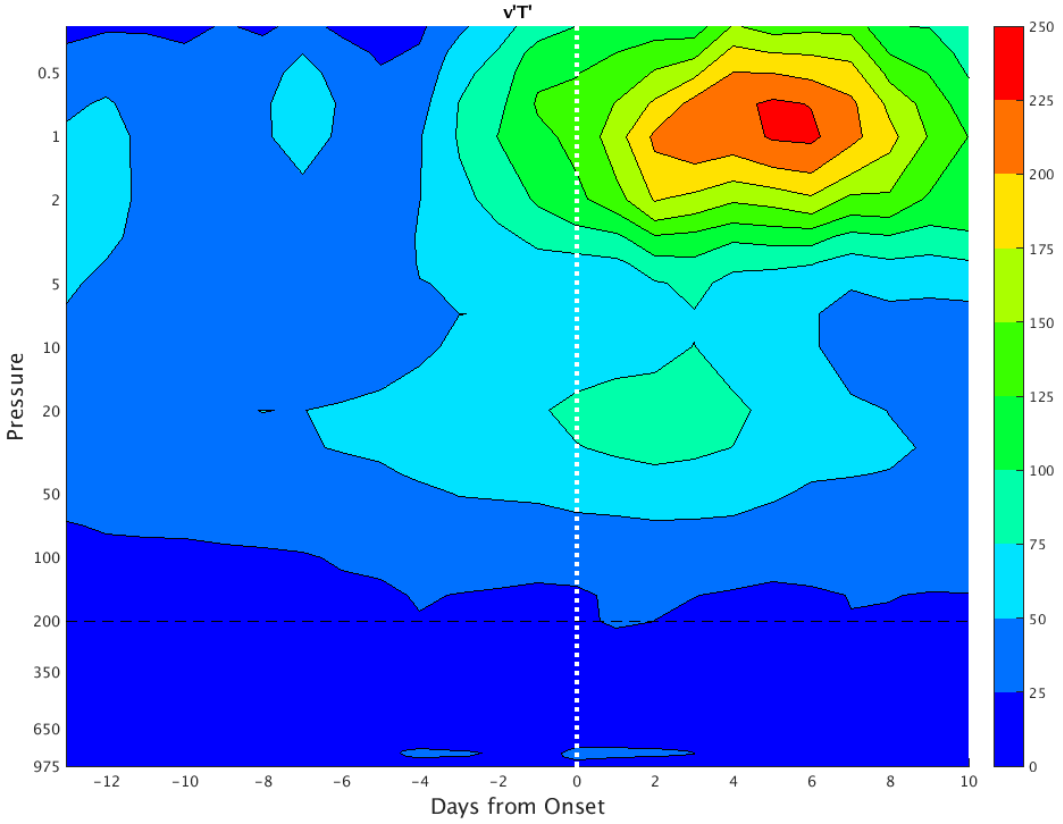

Figure 20: Eddy heat fluxes (K m s^{-1}) averaged over the area enclosed by each Aleutian High at its onset and composited over all 68 Aleutian High cases as a function of Days from Onset (Day 0) and Pressure (hPa). The contour interval is 25 K m s^{-1} and the white dotted line marks Day 0.

It is interesting that the maximum poleward eddy heat flux occurs in the composite after AH onset. This may reflect the fact that most AH events were followed by PVDs that are known to be forced by poleward eddy heat fluxes. Also, those AH events that were followed by PVDs had longer durations, on average, than those of AH events averaged over the entire sample. One could interpret this as meaning that long-lasting AH events are more likely to be followed by PVDs, or that the same process (poleward eddy heat flux) that forces a PVD helps maintain the antecedent AH.

A time-pressure plot of poleward eddy heat fluxes during AH decay is presented in Figure 21. The striking feature in this display is the weakening of the heat fluxes prior to AH decay; eddy heat fluxes near 20 hPa decrease from about 60 to 20 K m s^{-1} in the 12 days preceding composited AH decay. This feature coincides with stratospheric geopotential height falls induced by cyclonic PV increases in the troposphere and stratosphere. We therefore interpret AH onset and maintenance to be due to poleward eddy heat fluxes in the stratosphere, coupled with upward propagating anticyclonic waves from the troposphere, while AH decay is ascribed to the weakening of these heat fluxes, coincident with column-deep cyclonic PV increases.

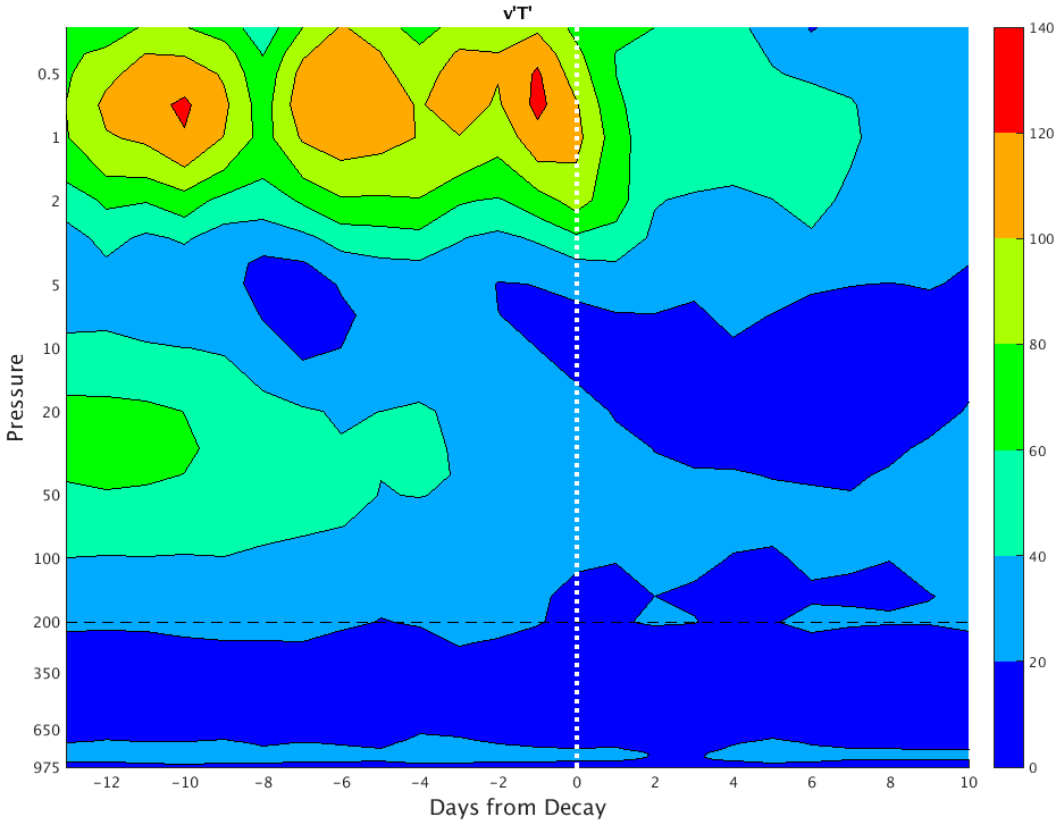

Figure 21: As in Figure 20, but averaged over the area enclosed by each Aleutian High at its decay and composited over all 68 Aleutian High cases as a function of Days from Decay (Day 0) and Pressure (hPa). The contour interval is 20 K m s^{-1}.

CHAPTER 4
GCM RESEARCH RESULTS AND DISCUSSION

GCM Results

The idealized GCM described in Chapter 2 was run in four different control run configurations. The first control run is the standard Polvani-Kushner model with no additional forcing. The control run is used to to form the climatological mean state of the model. The next two control runs both used the topographic forcing also described in the Chapter 2 section describing the model. The first of these uses the 2 km amplitude topography, and the second uses the 1.5 km topography. The topography serves as a source for planetary scale waves capable of displacing the polar vortex, so these topography-only control runs are used as baseline for comparing wave activity and displacements of the polar vortex in other model runs. The last control run uses no topography, but includes the tropospheric temperature perturbation, with λ_0=180° from equation (3). In addition to these control runs, the model was run with 2 km topography and temperature perturbations with λ_0 varied in 45° increments, and with 1.5 km topography and temperature perturbations with λ_0 varied in 22.5° increments. For all the model runs temperature, geopotential height, and horizontal wind values are recorded at six-hour intervals in isobaric spherical coordinates. The vertical wave activity and the geometric moments of the polar vortex are calculated at every time-step in all model runs. As mentioned in the introduction, this modelling research is motivated by a specific question: how does a temperature wave in the lower troposphere interact with surface topography to influence the polar vortex? I have two hypotheses for the answer to this question: local warming collocated with the topographic mountain will amplify the upward propagating wave, or a temperature wave phase shifted 90° west from topography will maximize vertical wave activity at the surface.

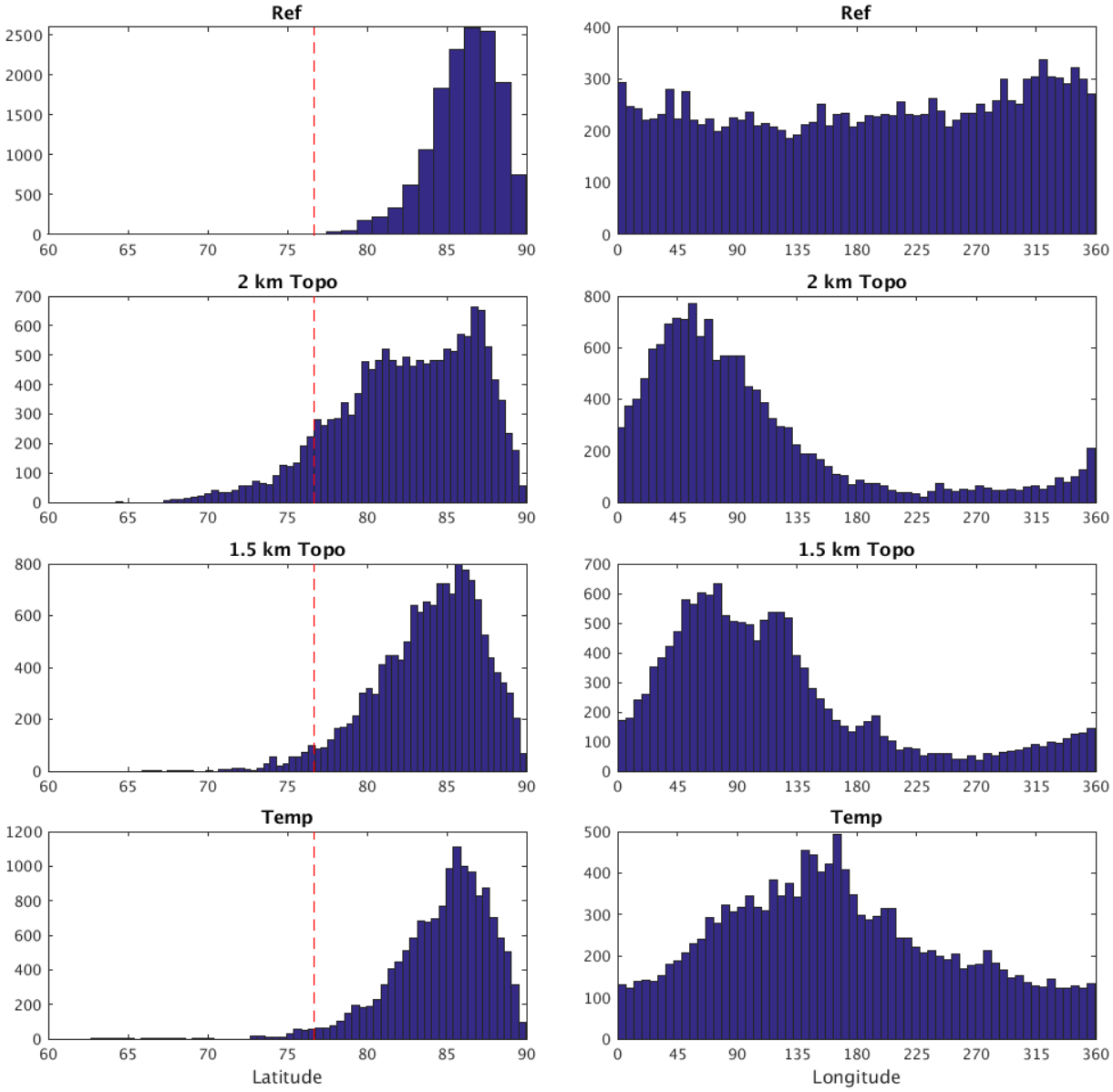

Figure 22: Histograms of the centroid latitude and longitude of the polar vortex in each control model run. The vertical red line in the centroid latitude plots represents the threshold for determining a displaced vortex (76.7°N).

The statistical distribution of the centroid of the polar vortex for each of the four control runs is presented in Figure 22. The vertical dashed line on the distribution of centroid latitude

indicates the threshold latitude for defining a displaced polar vortex. It is clear that the addition of topography broadens the distribution of the centroid latitudes causing the polar vortex to more often become displaced; increasing the amplitude of the topography increases the number of displacements. The centroid longitude of the polar vortex during the control runs with topography tends to be located opposite the topographic peak, although about 45° east of being exactly 180° away. The control run with only the thermal forcing also had some displaced days, though fewer than either topography run, and the centroid longitude distribution is broader than the topography runs with a peak near the maximum warm perturbation. Interestingly, this means that the warm-cool wave pattern in the troposphere, in the absence of any topography, is capable of displacing the stratospheric polar vortex.

There are eight model runs with the 2 km topography and thermal forcing with λ_0 varied in 45° increments. The response of the polar vortex in each of these runs is shown in Figure 23. In Figure 23a the percentage of days with a displaced polar vortex in each of these model runs is presented, and the percentage of displaced days for the control 2 km topography run and the control temperature perturbation run are shown with dashed black and red lines, respectively. In any combination of the thermal forcing and the 2 km topography, the occurrence rate of a displaced polar vortex never really increases above the 2 km topographic reference. This suggest that there is a saturation of wave-activity in the troposphere preventing the polar vortex from being displaced any more often. This is consistent with the results of Sheshadri et al. (2015), who found that increasing the wave-1 topography above 2 km did not increase the rate of polar vortex disturbances. To work around this issue the 1.5 km topography is used for all further analysis.

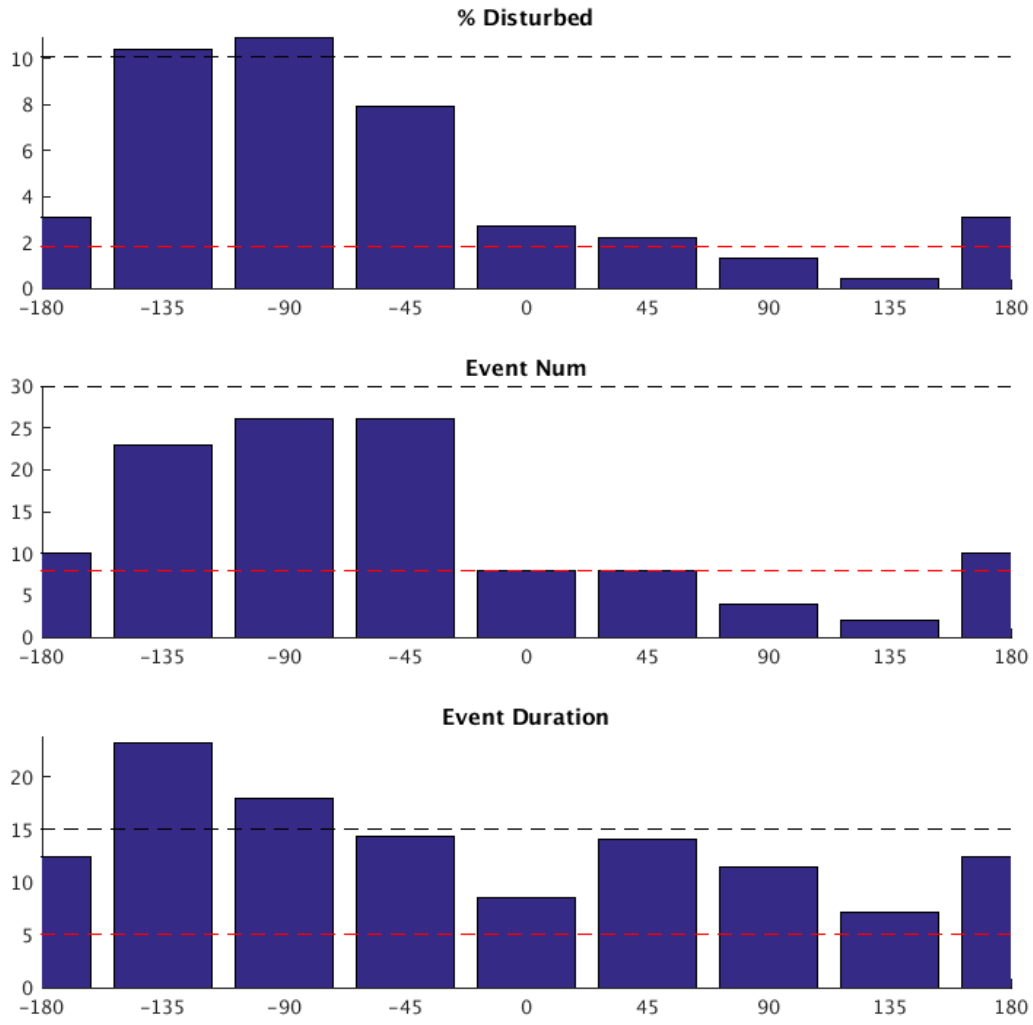

Figure 23: The percentage of disturbed days, number of PVD events, and average PVD duration in days is shown as a function of the phase difference between the topography and temperature forcing for the 2 km topography runs. The values for the topography only and thermal forcing only runs are shown with dashed black and red lines, respectively.

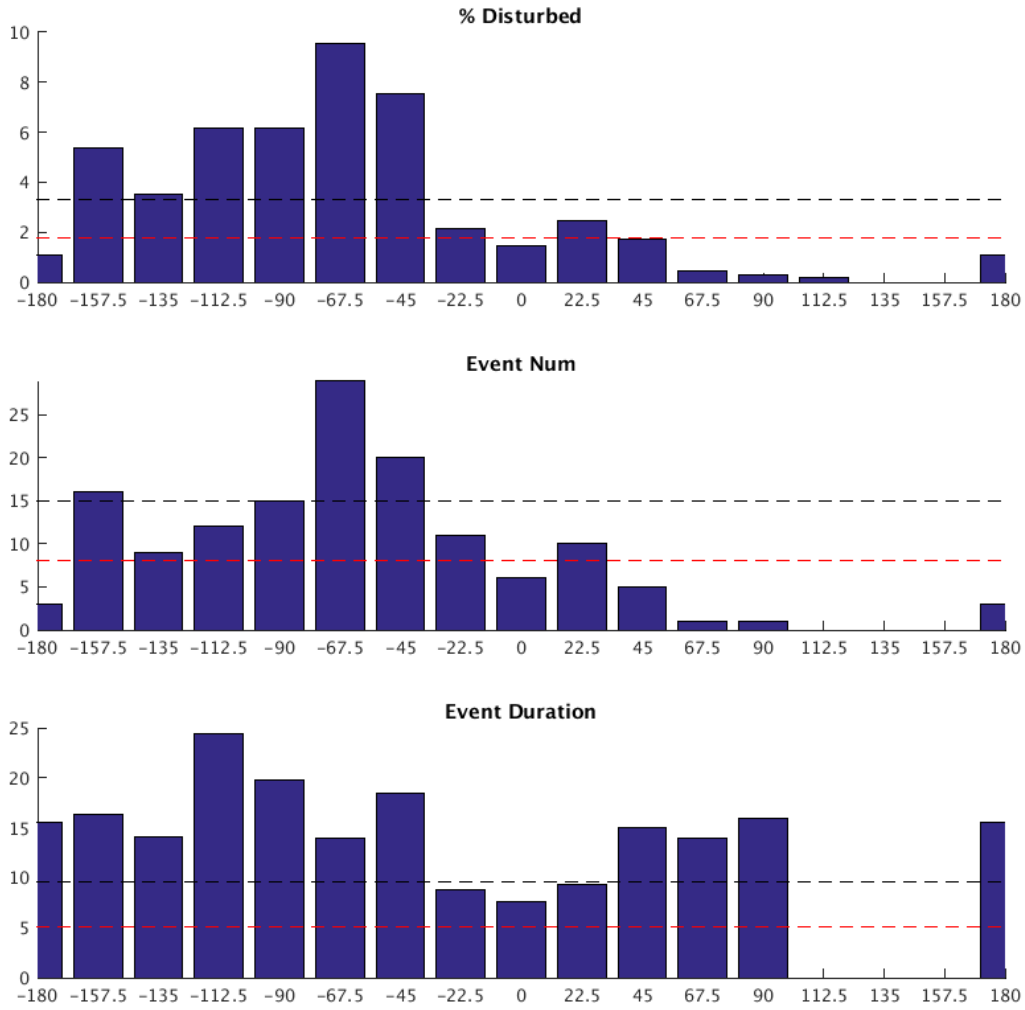

Figure 24: Same as Figure 23 but for the 1.5 km topography runs.

There are sixteen model runs with the 1.5 km topography and thermal forcing with λ_0 varied in 22.5° increments. The response of the polar vortex in each of these runs is shown in Figure 24. As before, in Figure 24a the percentage of days with a displaced polar vortex in each of these model runs is presented, and the percentage of displaced days for the control 1.5 km topography run and the control temperature perturbation run are shown with dashed black and

red lines, respectively. By comparing Figures 23 and 24, it is clear that in any configuration of temperature forcing, greater amplitude topography causes the polar vortex to be displaced more often. However, as expected, the number of displaced days for some of these runs is now larger than the 1.5 km topographic reference run, specifically the runs where the warming is east of the topographic peak. Surprisingly, despite there being more displaced days than in topography alone for six of the combined forcing runs, there are actually only two runs with noticeably more displacement events and two other runs with about the same number of events (Figure 24b). This means the displacement events in the other runs with an increased probability of displacement must have longer duration events. This is clearly true in Figure 24c, and in fact almost every run where the combined forcing causes displacements, those displacements end up having longer duration on average.

GCM Discussion

The most important result in this research is from Figure 24a, which shows the percentage of days with a displaced vortex in each model run. If the threshold latitude for designating a displaced polar vortex (76.7°N) is adjusted higher or lower the qualitative features of Figure 24a remain unchanged. In fact, the only aspect of Figure 24 which is sensitive to the threshold latitude is the average event duration (Figure 24c) for model runs with very few events (Figure 24b). For this reason, the event duration for model runs with fewer than five PVDs should be regarded as insignificant.

Adjusting the orientation of the warm and cold eddies relative to the topography has the ability to both substantially increase and completely suppress polar vortex displacements, compared to topography alone. Because disturbances of the polar vortex are considered a response to wave activity (Matsuno 1971; Polvani and Waugh 2004), the WAFz will be the tool we use to understand the differences in each model run. As mentioned earlier, when the WAFz is zonally averaged it gives the vertical EP flux. The vertical EP flux in the NH for the four

control runs and for the sixteen combined forcing runs are shown in Figures 25 and 26, respectively. What is most immediately clear throughout Figures 25 and 26 is that there are two distinct vertical levels in the troposphere with substantive vertical wave activity: one peaking near the surface at approximately 850 hPa, and the other in the upper troposphere peaking around 260 hPa. The time-mean WAFz, hence force denoted with square brackets as [WAFz], at these two levels for the four control runs are shown in Figure 27, and for the combined forcing runs Figures 28 and 29 show the [WAFz] at 850 hPa and 260 hPa, respectively. From Figures 27, 28, and 29 it is clear that the largest magnitudes of [WAFz] are occurring around the mid-latitude region on both vertical levels for every model run. Therefore, the [WAFz] in the region between 30°N and 70°N, which is also the region with the topography and temperature eddy forcing, is averaged (weighted by latitude) for every model run. This mid-latitude [WAFz] in the lower and upper troposphere is plotted as a function of the phase angle between the topography and the warm eddy in Figure 30. The values of the four controls are also included in Figure 30 as horizontal black lines labelled by the legend in the figure.

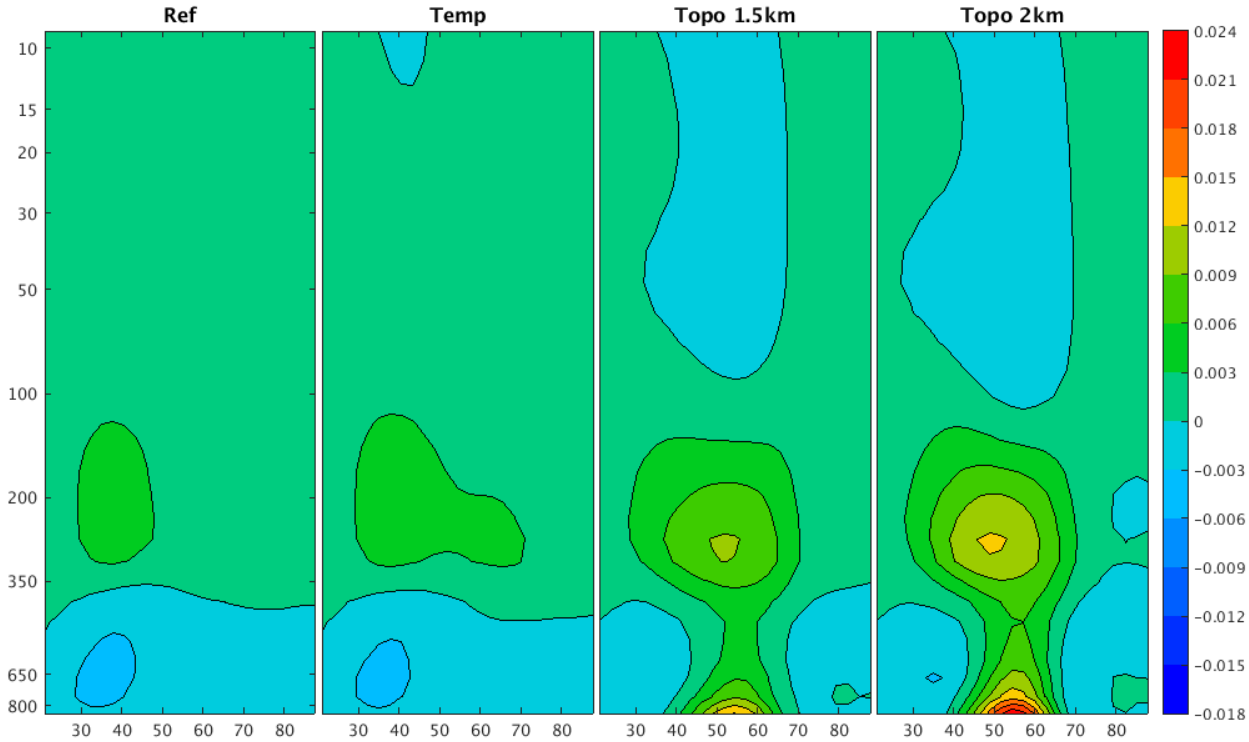

Figure 25: The time-mean vertical EP flux in all four model control runs as a function of latitude and pressure, and in units of m^2/s^2.

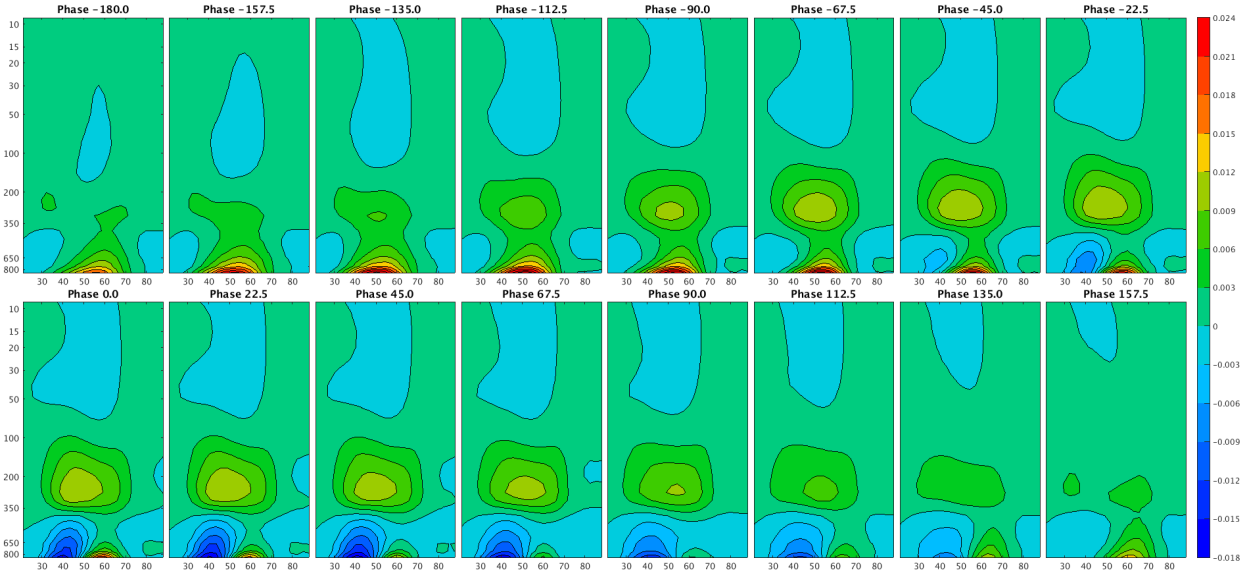

Figure 26: Same as Figure 25 but for all the 1.5 km topography and temperature forcing runs.

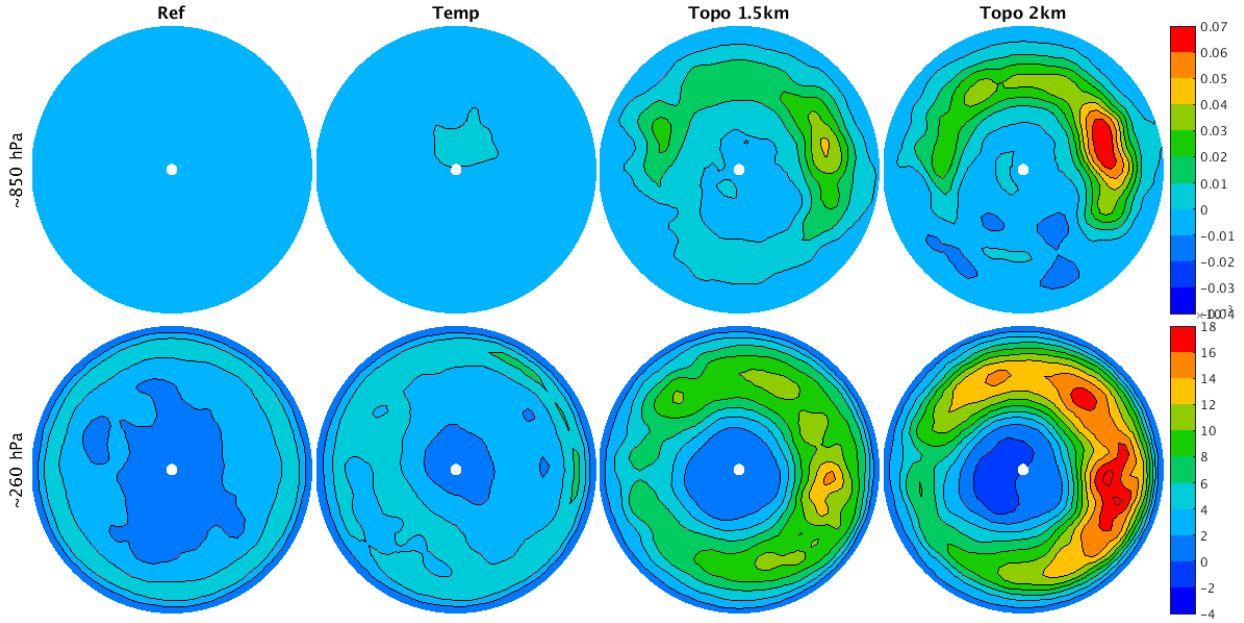

Figure 27: The time-mean WAFz in the control runs in upper and lower troposphere in units of m^2/s^2.

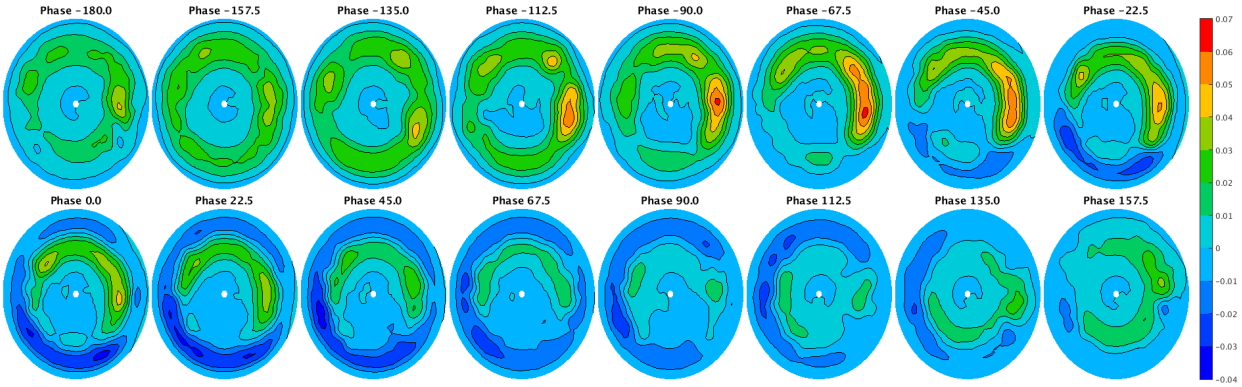

Figure 28: The time-mean WAFz for all the 1.5 km topography and temperature forcing runs in the lower troposphere in units of m^2/s^2.

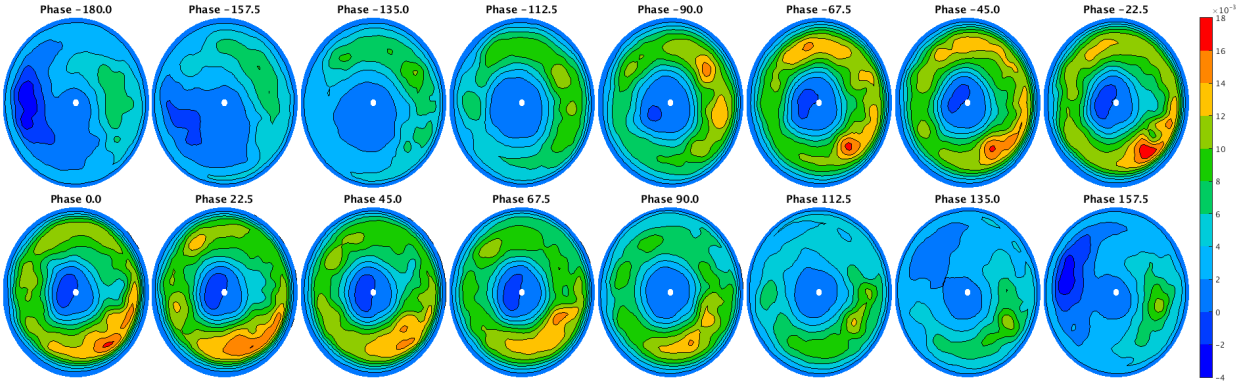

Figure 29: The time-mean WAFz for all the 1.5 km topography and temperature forcing runs in the upper troposphere in units of m^2/s^2.

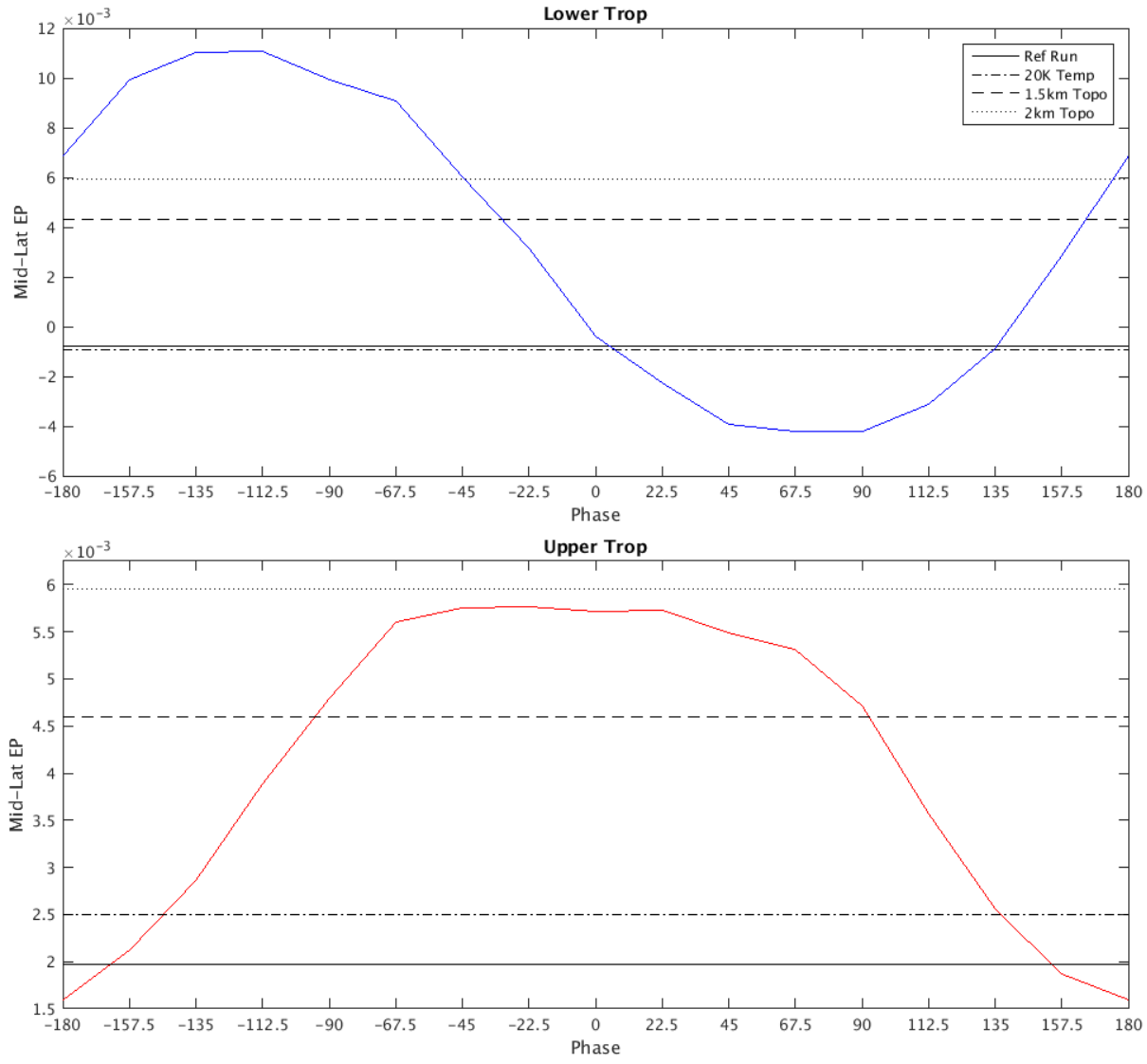

Figure 30: The time-mean WAFz averaged between 30°N and 70°N for all the 1.5 km topography and temperature forcing runs in the lower and upper troposphere. The four control runs are also included using the horizontal black lines described in the figure key.

There is an analytical way to predict how the temperatures wave and the topography will interact to generate wave activity near the surface using equation (15) for WAFz. Assuming the winds are geostrophic then the maximum meridional winds should be located 90°W (-90°) from the topography peak. Therefore, when the warm eddies in the temperature wave are -90° phase

shifted from the topography peak, WAFz should be maximized. This prediction proves to be correct for the mid-latitude [WAFZ] in the lower troposphere in Figure 30a. The peak in Figure 30a is actually at -112.5°, but Figure 31 shows [T'] and [Z] for all the combined forcing runs and from that we can see the climatological position on the temperature eddies shifted slightly east from the maximum in the temperature forcing. It is important to note that this explanation of the lower tropospheric wave activity does not completely explain the probability of a displaced polar vortex in Figure 24a. Although, it is only model runs with more lower tropospheric [WAFz] that have a higher probability of a displaced vortex compared to the 1.5 km reference run.

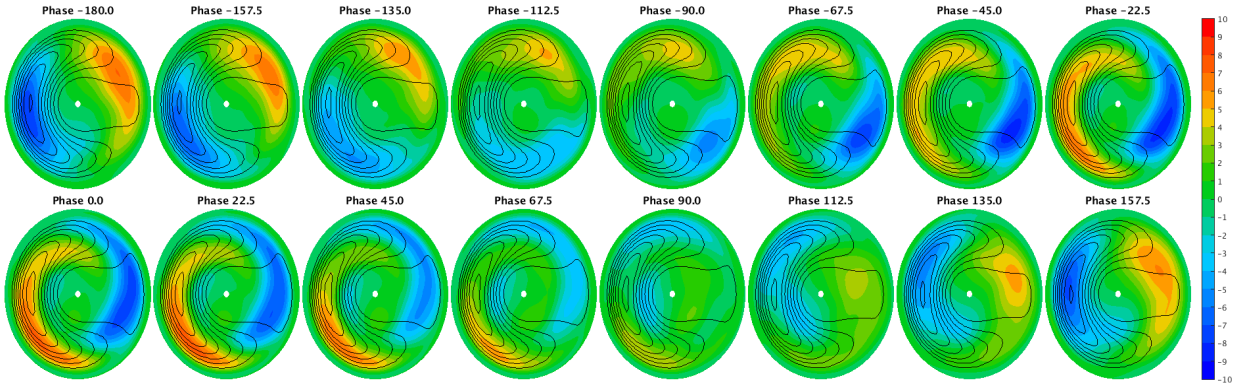

Figure 31: Time-mean eddy temperatures and time-mean geopotential height in lower troposphere for all the 1.5 km topography and temperature forcing runs.

To understand why the -67.5° and -45° runs have the highest probability of a displaced vortex, the upper tropospheric [WAFz], Figure 30b, must also be discussed. The upper troposphere [WAFz] peaks in the -22.5° run, meaning the run with the eddy warming most collocated with the topography peak. From the ideal gas law and hydrostatic equation, warm air leads to an expanding air column which induces geopotential height rises aloft, likewise cold air leads to geopotential height falls aloft. So it follows, when the warm eddy forcing in the lower troposphere is collocated with the topography peak, and cold eddy forcing is opposite it, the topographically induced wave pattern in the geopotential height field of the upper troposphere

will be amplified by the respective expanding and contracting. This amplification of the geopotential height wave, which would also amplify the meridional winds geostrophically, is the driver of how upper tropospheric [WAFz] responds to the temperature forcing. In fact, the temperature forcing reference run only had notably positive [WAFz] in the upper troposphere, and still almost 2% of days in that run have a displaced polar vortex. This means it is possible to disturb the polar vortex with upward wave activity only from the upper troposphere, and not from the surface. Combining this understanding of how both the lower and upper troposphere are influenced by the temperature forcing explains why the -67.5° run has the highest probability of a displaced polar vortex. When the temperature wave is phase shifted about -45° from the topographic wave the upper and lower tropospheric [WAFz] are increased compared to the 1.5 km reference run.

Another interesting result of this experiment is that when combined with topography the temperature forcing can not only increase, but in some configurations substantially decrease [WAFz]. There are, in fact, three model runs in Figure 24b that do not contain any displacement events (112.5°, 135°, and 157.5°), the latter two not having a single day with a displace polar vortex. From Figure 30, both the lower and upper troposphere have runs where [WAFz] is reduced even below the values found in the control run, meaning the combination of the temperature wave and topography wave in those runs generate less upward wave activity than no forcing at all. However, if we compare, for example, the upper tropospheric [WAFz] for the -180° run to the upper tropospheric [WAFz] in the control run, Figures 26 and 27, respectively, we see that there is more spatial variability in the -180° run despite having a lower mid-latitude average.

This spatial variability of the [WAFz] in the lower and upper troposphere is worth further discussion to better understand what is generating the wave activity. Looking at the zonally averaged [WAFz] near the surface in Figure 26, there are two distinct latitude regimes. The positive [WAFz] always peaks north of 50°N, often contained between 50°N-70°N, and the

negative [WAFz] is mostly contained between 30°N-50°N. Both forcings are contained between 30°N-70°N with a maximum amplitude at 50°N. So, the large amplitudes in near surface [WAFz] occur within the region influenced by the forcing with positive [WAFz] to the north of the maximum forcing, and negative to the south. The meridional dependence of the lower troposphere [WAFz], Figure 28, shows more distinction between the regions of positive and negative [WAFz]. The positive [WAFz] tends to be located west of the topography peak with a maximum opposite the topography. The eddy warming on the western side of the anticyclone is associated with positive [WAFz], comparing Figure 28 to Figure 31, but the largest values of [WAFz] are collocated with the cold eddies and largest negative values are associated with warm eddies on the eastern side of the anticyclone. For the upper tropospheric [WAFz], in the few runs with negative [WAFz] it is always collocated with the topographically generated anticyclone, and positive [WAFz] are largely centered opposite the topography with some east west variability based on which side of the anticyclone is being amplified by eddy warming below (Figure 29).

At this point it is worth readdressing the motivating question of this research: how does a temperature wave in the lower troposphere interact with surface topography to influence the polar vortex? It is clear that the temperature wave is influencing the polar vortex, and that the this is largely achieved through interacting with the topography. There were two hypotheses for how this would occur: local warming collocated with the topographic mountain will amplify the upward propagating wave, or a temperature wave phase shifted 90° west from topography will maximize vertical wave activity at the surface. Interestingly, both of these hypotheses seem to be true, however, the second hypothesis is the most important. Having the temperature wave phase shifted west from the topography amplifies the vertical wave activity near the surface increasing the probability of a displacement over topography alone. Although, warming at least nearly collocated with the topography peak will amplify the geopotential wave pattern, and therefore the vertical wave activity, in the upper troposphere also influencing the polar vortx.

The largest probability of a displace polar vortex occurs when temperature wave is phase shifted 45° west from topography, averaged between the values predicted by each hypothesis.

The final aspect of the modelling results that needs to be discussed is increased duration of PVDs during model runs that included both forcings, compared to topography alone. To try and better understand this, Figure 32 shows the lower (blue) and upper (red) tropospheric mid-latitude EP-flux composited around the onset of each PVD for all the phase experiments with an increased likihood of displacement. The lower and upper tropospheric mid-latitude EP-fluxes are composited for the 1.5 km topography control run and plotted with dashed lines and the same color scheme in each panel of Figure 32. Compared to the topography reference, all of the runs shown in Figure 32 have larger lower tropospheric wave activity around the onset, and the two runs with the most events also have incread upper tropospheric wave activity. This is consistent with the results discussed earlier. Also unsurprising, for all runs, including the control, the lower tropospheric wave activity peaks about 5 days before the onset of a PVD. The increased amplitude of the lower tropospheric wave activity preceding the onset of a PVD is likely enough to increase the duration of the resulting PVD in the combined forcing runs. However, an interesting additional feature in Figure 32, there is a secondary maximum in the lower tropospheric wave activity between 5 to 15 days after the onset for all combined forcing runs. This suggest that the PVDs in the combined forcing runs are associated with wave packets with longer duration, or potentially with multiple wave packets, along with having a greater amplitude, compared to the topography alone. This is a possible explination for the increased duration of PVDs in the combined forcing run, but a more thorough investigation is needed.

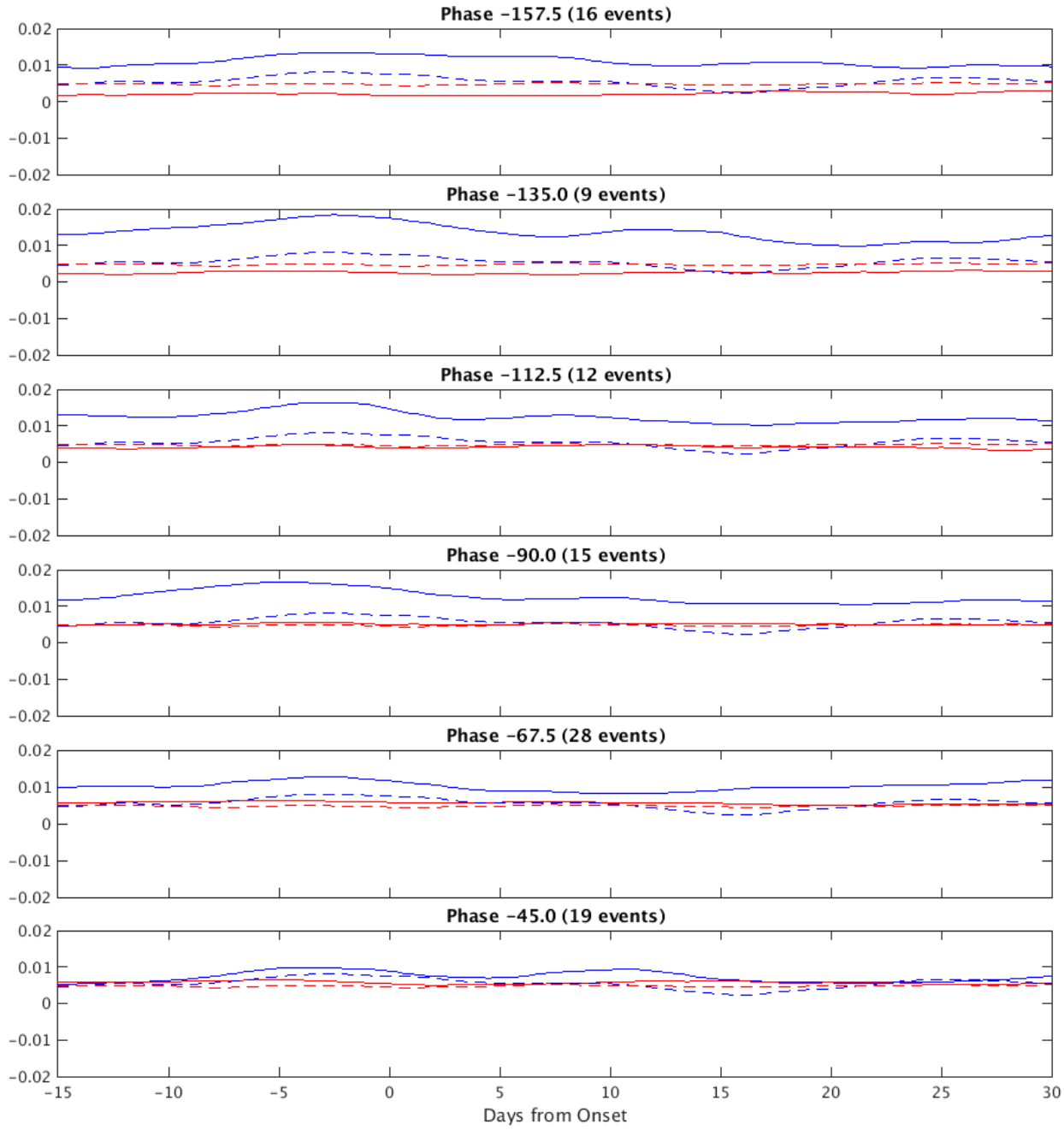

Figure 32: Lower tropospheric (blue) and upper tropospheric (red) mid-latitude EP fluxes composited around the onset of all PVDs in each phase experiment (solid) with increased probability of disturbance and the topography only control (dashed)

CHAPTER 5

CONCLUSION

The stratospheric polar vortex was analyzed using geometric moments on each day for the winter seasons of 1981-2017 and was classified as being split, displaced, or undisturbed. The classified days were then used to identify disturbance events, or PVDs, based on whether the polar vortex was split or displaced for at least 3 consecutive days. Sixty PVDs were identified for the 37 years included in this study, and the average duration of an event was 23.8 days while the average onset date was 16 February.

The climatology of PVDs suggests that a disturbed polar vortex is most likely to be present from late January to early April. There is also a secondary peak in PVD probability in early December, with a local minimum around 1 January. The number of PVD events per winter was approximately constant for the period analyzed. However, the fraction of disturbed days per winter showed a statistically significant lull during the period from 1990 to 1998 due to shorter duration events during this period, consistent with previous research.

For each event, a spatial averaging filter based on the position of the disturbed polar vortex throughout the duration of the event was calculated. This is used as a weighting for averaging geopotential height and temperature anomalies and tendencies to find a mean value under the vortex disturbance. Both height and temperature tendencies are negative preceding the onset of a PVD (Figure 7), while the negative temperature tendencies coincide with the negative height tendencies and seem to permeate upward from the troposphere. This suggests that regional tropospheric cooling could help contract the atmosphere, driving negative height tendencies that permeate in the stratosphere, as evident by the height falls being immediately above the cooling. This creates an incentive for the polar vortex to migrate over the region of antecedent cooling.

The spatial averaging filter is also used to average terms from a thermodynamic budget under the disturbed polar vortex. Significant advective cooling in the lower and middle stratosphere

persists for weeks preceding the onset of a PVD, and significant residual (likely adiabatic) cooling persists in the troposphere for the entire period analyzed around PVD onset (20 days before to 30 days after). Advective cooling is the primary contributor to the negative temperature tendencies preceding PVD onset in the lower stratosphere. Residual (likely adiabatic) cooling is an important tropospheric feature of the mid-latitude region into which a disturbed polar vortex migrates, and contributes, along with the advective cooling in the stratosphere, to the analyzed cooling preceding PVD onset.

Applying a geometric moments technique to the reanalysis data set and updating a previously published definition, we have identified 68 AH events during 35 winter (October through March) seasons (1979-80 through 2013-14), for approximately two events per season. The number of events per season ranged from zero to four. On average, the first and second events began on 18 November and 1 January, respectively, with each event approximately lasting an average of 33 days.

Thirteen (41) of the 68 AH events each temporally and spatially coincided with tropospheric blocking, identified with a wave-breaking (persistent anomaly) definition. A statistically significant number of AH onsets coincide with a persistently positive geopotential height anomaly in the troposphere. Forty-one of the 68 AH events each either coincided with or were followed by a PVD event, determined though application of the moments technique to reanalysis PV data. Forty-seven of the identified 55 PVD events were each preceded by an AH onset, such that in almost all winters (33 out of 35), an early season AH was followed by a later season PVD. With statistical significance, a PVD day was preceded, at 20 – 30 days, by an AH day in our dataset.

Employing a form of PV inversion, we have determined that, in a composite sense, the geopotential height rises associated with AH onset are forced primarily by anticyclonic PV increases in the stratosphere. These stratospheric PV changes significantly induce tropospheric height rises following AH onset, suggesting a downward coupling of the stratosphere to the

troposphere. This is also true for the composite of the subset of AH onsets coincident with tropospheric blocking (by either definition). In those events, there were also composite tropospheric and lower stratospheric height rises due to tropospheric anticyclonic PV increases under the AH after AH onset. Interestingly, in these cases there are significant height falls in the troposphere and lower stratosphere beneath the incipient AH due to tropospheric cyclonic PV increases about ten days prior to AH onset. The geopotential height falls associated with composite AH decay were found to be due to cyclonic PV increases in both the troposphere and stratosphere.

Next, poleward eddy heat fluxes in the stratosphere precede and especially follow composite AH onset. This result is consistent with our findings that composite AH onset is forced primarily by anticyclonic PV increases in the stratosphere and that many AH onsets were each followed by a PVD onset. Poleward eddy heat fluxes weaken in the stratosphere prior to AH decay, coinciding with stratospheric geopotential height falls induced by cyclonic PV increases in both the troposphere and stratosphere. The onset-decay asymmetry in the tropospheric forcing of stratospheric height tendencies (present at decay but absent during onset) is mysterious and deserving of further investigation.

The fraction of disturbed days was shown to be negatively correlated to the fraction of days with an Aleutian High present and with the westerly phase of the QBO. The former result is surprising given the findings of Colucci and Ehrmann (2018) while the latter is consistent with the Holton and Tan (1980) relationship. AH PVDs feature fewer split vortices because of the association of the AH with the wave-1 planetary waves. The advective cooling in the lower and middle stratosphere is also significantly more intense for AH PVDs before the onset. The average position of QBOe PVDs suggest consistent displacements into the Eurasian region, and QBOw PVDs contain more split vortices and a broader distribution of displacement positions. The easterly QBO is also associated with stronger thermodynamic activity in the upper stratosphere in the fifteen to thirty days following PVD onset.

The reanalysis work suggested a connection between the polar vortex and tropospheric temperatures. Particularly, this work suggest that tropospheric temperatures could play a role in the onset of a PVD, with cooling in the upper troposphere preceding the onset of PVDs in the vicinity of the disturbed polar vortex. To further tease out this relationship between tropospheric temperatures and the polar vortex, a series of modeling experiments are performed. The CAM6 dry-core is run in the Held-Suarez configuration with the Polvani-Kushner modifications. Additionally, the model is forced with a zonal wave number 1 topographical mountain, and a zonal wave 1 temperature wave added to the reference temperature profile, each contained within the mid-latitudes of the winter hemisphere. The phase difference between temperature wave and the topography wave is varied to test how region of relative warming or cooling effect the topographies ability to influence the stratosphere.

Each model experiment is run for ten years with the first two-hundred days dismissed as spin-up. Geometric moments were taken of the geopotential height field at approximately 8 hPa on every day of all model runs to determine whether or not the polar vortex is displaced. The percentage of days with a displaced polar vortex, the number of PVDs, and the average duration of a PVD was also calculated for all model runs. When the regional warming was located west (east) of the topography peak and regional cooling to the east (west), this increased (decreased) the probability of the polar vortex being disturbed compared to topography alone. The phase difference between the temperature wave and topography wave that provides the highest probability of a disturbed polar vortex is -67.5°, or the maximum warm eddies located 67.5° west of the topography peak. In order to maximize WAFz in the lower troposphere the warm eddies must be to the west of the topography, collocated with the positive meridional wind. It is also important that warm eddies be close to topography peak because this amplifies the anticyclone aloft, increasing WAFz in the upper troposphere. The combination of these two factors suggest warm eddies 45° west of the topography peak would be ideal for amplifying wave activity in the upper and lower troposphere. Since the actual location of the warm and cold eddies drifts about

22.5° east from their location in the reference temperature profile in the model, the -67.5° model run actually has peak eddy warming about 45° west of the topography peak. This means that amplifying WAFz in the lower and upper troposphere is more important for increasing the probability of a vortex disturbance then lower tropospheric wave activity alone.

For many model runs with a higher probability of a displacement compared to just topography, the actual number of PVDs in a ten year run decreased. This means that the average duration of a PVD increased for those, and, in fact, almost every model run. This increased duration is likely a result of the fact that the wave packets that triggered the PVDs in model run with the thermal forcing had larger amplitudes and durations, on average, than the topography only run. This causes the polar vortex to takes longer to recover to its undisturbed position, making the duration of the events increase.

It is also worth discussing how the reference run with only temperature forcing, and no topography also had several PVDs. This model run had no upward wave activity in the lower troposphere, with the only positive WAFz in the upper troposphere. This means that the polar vortex can be displaced without topographically forced waves, and without waves generated at the surface. This specifically, along with the broader results of the modelling work highlights the importance of upper tropospheric wave activity in triggering PVDs.

Tying these results back to reanalysis results, the optimal position for the tropospheric cooling is 45° west of the surface pressure low. This is also the longitudinal position that the polar vortex tends to migrate toward in the model run. This means that the polar vortex will tend to migrate toward the region of tropospheric cooling in the ideal configuration for a PVD. Unlike the reanalysis results this cooling is in the lower troposphere not the upper troposphere, the cooling is driven by diabatic processes forcing the model not advective processes, and the model cooling is in the climatology not the anomalously large cooling in the reanalysis. Nonetheless, the modeling work suggest that region tropospheric cooling in the vicinity of the

disturbed polar vortex is reflection of the tropospheric temperature patterns being in an ideal configuration compared to the surface pressure wave.

I believe the these results are most informative about the likelihood of specific weather systems leading to a PVD. In the Lehtonen and Karpechko (2016) paper, mentioned in the introduction, statistically significant near-surface temperature anomalies are found in a wave-1 pattern preceding mid-winter PVDs. That temperature anomaly pattern is phase shifted west from the sea-level pressure anomalies present during that same time, also in a wave-1 pattern. There result indicates that a wave-1 temperature pattern is often present preceding a PVD, and the modelling work here shows that that temperature pattern contributes in an important way to causing the PVD. In regards to the goal of more accurately predicting the onset and evolution of a PVD, the results of this modelling work highlight the importance of accurately predicting the global surface temperature patterns. The ability of a model to predict the orientation of the near-surface temperature wave relative to the sea-level pressure wave will directly influence the likelihood of a PVD appearing in the model.

It is, perhaps, worth excercising caution when interpreting the result that some of the configurations in the modelling research showed a complete surpression of PVDs. The temperature wave pattern in the model is supported through diabatic processes by relaxing toward the reference temperatures. Constant diabatic warming of air flowing from the pole, or diabatic cooling of air flowing from the equator, is not representative of any real physical process, so it is unlikely that the temperature patterns associated with no PVDs could persist. However, if this pattern of cold air west of the topographic peak did develop it would make the likelihood of a PVD much lower as long as the temperature pattern persisted.

It is worth considering how these results relate to the problem of the changing climate. Given the well documented changes of the Earth's climatological temperature field, it will be important to remember going forward that changes in the longitudinal structure of the temperature field will interact with the surface pressure wave. This asymmetric change has the

potential to either increase or decrease the likelihood of a PVD occurring, which will strongly influence the variability of mid-winter weather in the North Hemisphere, especially the likelihood of a cold air outbreak. Additionally, "artic amplification", defined by relatively higher warming near the poles, weakens the meridional temperature gradient from equator to pole. Rerunning these modelling experiments with reference temperature field that also has a weakened meridional temperature gradient could potentially illuminate ways in which climate change can effect the probability of a PVD.

The most obvious direction to go to expand this work further would by testing the wave-2 topography case. It would be interesting to see additional of the temperature wave has the same potential to increase the probability of a PVD in the wave-2 case. The importance of anomalous temperatures in causing a PVD could also be explored in further modeling experiments by having the temperature wave pattern turned on and off during a model run to test how this affects the likelihood of a displacement on shorter timescales.

Lastly, the model used in this research was one of the most idealized models still in use by the research community. There is a whole hierarchy of models with increasing degrees of complexity and realism. First, the idealized model could be adjusted in ways that make it more similar to the Earth's climate. A seasonal cycle could be added by using a different reference temperature profiles for each month or day. This seasonality would indicate how the PVD probability changes during mid-winter and late winter, and if any period is particulary sensitive to the temperature wave forcing. Next, a more realistic topography and a more realistic reference temperature profile is could be used without any fundamental changes to the model. Running the temperature wave forcing experiments in this setting would serve to reinforce the robustness of my results, although I suspect the basic conclusions would remain unchanged. Finally, a non-idealized full physics model can be used, capturing all the physical processes important to the atmosphere. These expariments would require "turning on" the temperature wave forcing temporarily, as it would be important to not change the underlying climatology.

Using the full-physics model would prove most conclusively, in concert with the results of the idealized model, how the temperature wave influences the polar vortex. It is clear that understanding how tropospheric temperatures influence the polar vortex is an important part of predicting how and when the polar vortex will be disturbed.

REFERENCES

Bao, M., X. Tan, D. L. Hartmann, and P. Ceppi, 2017: Classifying the tropospheric precursor patterns of sudden stratospheric warmings. *Geophys. Res. Lett.*, doi:10.1002/2017GL074611.

Bresky, W. C., and S. J. Colucci, 1996: A Forecast and Analyzed Cyclogenesis Event Diagnosed with Potential vorticity. *Mon. Weather Rev.*, **124**, 2227–2244, doi:10.1175/1520-0493(1996)124<2227:AFAACE>2.0.CO;2. http://journals.ametsoc.org/doi/abs/10.1175/1520-0493%281996%29124%3C2227%3AAFAACE%3E2.0.CO%3B2.

Butler, A. H., D. J. Seidel, S. C. Hardiman, N. Butchart, T. Birner, and A. Match, 2015: Defining sudden stratospheric warmings. *Bull. Am. Meteorol. Soc.*, **96**, 1913–1928, doi:10.1175/BAMS-D-13-00173.1.

——, J. P. Sjoberg, D. J. Seidel, and K. H. Rosenlof, 2017: A sudden stratospheric warming compendium. *Earth Syst. Sci. Data*, doi:10.5194/essd-9-63-2017.

Charlton, A. J., and L. M. Polvani, 2007: A new look at stratospheric sudden warmings. Part I: Climatology and modeling benchmarks. *J. Clim.*, **20**, 449–469, doi:10.1175/JCLI3996.1.

Colucci, S. J., 1985: Explosive Cyclogenesis and Large-Scale Circulation Changes: Implications for Atmospheric Blocking. *J. Atmos. Sci.*, **42**, 2701–2717, doi:10.1175/1520-0469(1985)042<2701:ECALSC>2.0.CO;2. http://journals.ametsoc.org/doi/abs/10.1175/1520-0469%281985%29042%3C2701%3AECALSC%3E2.0.CO%3B2.

——, 2010: Stratospheric Influences on Tropospheric Weather Systems. *J. Atmos. Sci.*, **67**, 324–344, doi:10.1175/2009JAS3148.1. http://journals.ametsoc.org/doi/abs/10.1175/2009JAS3148.1.

Colucci, S. J., and M. E. Kelleher, 2015: Diagnostic Comparison of Tropospheric Blocking

Events with and without Sudden Stratospheric Warming. *J. Atmos. Sci.*, **72**, 2227–2240, doi:10.1175/JAS-D-14-0160.1. http://dx.doi.org/10.1175/JAS-D-14-0160.1.

Colucci, S. J., and T. S. Ehrmann, 2018: Synoptic-Dynamic Climatology of the Aleutian High. *J. Atmos. Sci.*, doi:10.1175/JAS-D-17-0215.1.

Colucci, S. J., D. P. Baumhefner, and C. E. Konrad, 1999: Numerical prediction of a cold-air outbreak: A case study with ensemble forecasts. *Mon. Weather Rev.*, doi:10.1175/1520-0493(1999)127<1538:NPOACA>2.0.CO;2.

Coughlin, K., and L. J. Gray, 2009: A Continuum of Sudden Stratospheric Warmings. *J. Atmos. Sci.*, **66**, 531–540, doi:10.1175/2008JAS2792.1. http://journals.ametsoc.org/doi/abs/10.1175/2008JAS2792.1.

Davis, C. A., and K. A. Emanuel, 1991: Potential Vorticity Diagnostics of Cyclogenesis. *Mon. Weather Rev.*, **119**, 1929–1953, doi:10.1175/1520-0493(1991)119<1929:PVDOC>2.0.CO;2. http://journals.ametsoc.org/doi/abs/10.1175/1520-0493%281991%29119%3C1929%3APVDOC%3E2.0.CO%3B2.

Dennis, J. M., and Coauthors, 2012: CAM-SE: A scalable spectral element dynamical core for the Community Atmosphere Model. *Int. J. High Perform. Comput. Appl.*, **26**, 74–89, doi:10.1177/1094342011428142. http://journals.sagepub.com/doi/10.1177/1094342011428142.

Dole, R. M., and N. D. Gordon, 1983: Persistent Anomalies of the Extratropical Northern Hemisphere Wintertime Circulation: Geographical Distribution and Regional Persistence Characteristics. *Mon. Weather Rev.*, **111**, 1567–1586, doi:10.1175/1520-0493(1983)111<1567:PAOTEN>2.0.CO;2. http://journals.ametsoc.org/doi/abs/10.1175/1520-0493%281983%29111%3C1567%3APAOTEN%3E2.0.CO%3B2.

Dunn-Sigouin, E., and T. A. Shaw, 2015: Comparing and contrasting extreme stratospheric

events, including their coupling to the tropospheric circulation. *J. Geophys. Res.*, doi:10.1002/2014JD022116.

Edmon, H. J., B. J. Hoskins, and M. E. McIntyre, 1980: Eliassen-Palm Cross Sections for the Troposphere. *J. Atmos. Sci.*, **37**, 2600–2616, doi:10.1175/1520-0469(1980)037<2600:EPCSFT>2.0.CO;2. http://journals.ametsoc.org/doi/abs/10.1175/1520-0469%281980%29037%3C2600%3AEPCSFT%3E2.0.CO%3B2.

Ehrmann, T. S., and S. J. Colucci, 2019: A thermodynamic climatology of the disturbed stratospheric polar vortex. *Int. J. Climatol.*, joc.6015, doi:10.1002/joc.6015. https://onlinelibrary.wiley.com/doi/abs/10.1002/joc.6015.

Garfinkel, C. I., D. L. Hartmann, and F. Sassi, 2010: Tropospheric precursors of anomalous northern hemisphere stratospheric polar vortices. *J. Clim.*, doi:10.1175/2010JCLI3010.1.

Gelaro, R., and Coauthors, 2017: The modern-era retrospective analysis for research and applications, version 2 (MERRA-2). *J. Clim.*, doi:10.1175/JCLI-D-16-0758.1.

Hannachi, A., D. Mitchell, L. Gray, and A. Charlton-Perez, 2011: On the Use of Geometric Moments to Examine the Continuum of Sudden Stratospheric Warmings. *J. Atmos. Sci.*, **68**, 657–674, doi:10.1175/2010JAS3585.1. http://journals.ametsoc.org/doi/abs/10.1175/2010JAS3585.1.

Hare, F. K., 1960: THE DISTURBED CIRCULATION OF THE ARCTIC STRATOSPHERE. *J. Meteorol.*, **17**, 36–51, doi:10.1175/1520-0469(1960)017<0036:TDCOTA>2.0.CO;2. http://journals.ametsoc.org/doi/abs/10.1175/1520-0469%281960%29017%3C0036%3ATDCOTA%3E2.0.CO%3B2.

Harvey, V. L., and M. H. Hitchman, 1996: A Climatology of the Aleutian High. *J. Atmos. Sci.*, **53**, 2088–2102, doi:10.1175/1520-0469(1996)053<2088:ACOTAH>2.0.CO;2.

Haynes, P. H., and M. E. McIntyre, 1990: On the Conservation and Impermeability Theorems for Potential Vorticity. *J. Atmos. Sci.*, **47**, 2021–2031, doi:10.1175/1520-

0469(1990)047<2021:OTCAIT>2.0.CO;2.
http://journals.ametsoc.org/doi/abs/10.1175/1520-0469%281990%29047%3C2021%3AOTCAIT%3E2.0.CO%3B2.

Held, I. M., and M. J. Suarez, 1994: A Proposal for the Intercomparison of the Dynamical Cores of Atmospheric General Circulation Models. *Bull. Am. Meteorol. Soc.*, doi:10.1175/1520-0477(1994)075<1825:APFTIO>2.0.CO;2.

Hitchcock, P., T. G. Shepherd, and G. L. Manney, 2013: Statistical characterization of Arctic polar-night jet oscillation events. *J. Clim.*, doi:10.1175/JCLI-D-12-00202.1.

Holton, J. R., and H.-C. Tan, 1980: The Influence of the Equatorial Quasi-Biennial Oscillation on the Global Circulation at 50 mb. *J. Atmos. Sci.*, **37**, 2200–2208, doi:10.1175/1520-0469(1980)037<2200:TIOTEQ>2.0.CO;2.
http://journals.ametsoc.org/doi/abs/10.1175/1520-0469%281980%29037%3C2200%3ATIOTEQ%3E2.0.CO%3B2.

Huang, J., W. Tian, J. Zhang, Q. Huang, H. Tian, and J. Luo, 2017: The connection between extreme stratospheric polar vortex events and tropospheric blockings. *Q. J. R. Meteorol. Soc.*, doi:10.1002/qj.3001.

Jia, L., and Coauthors, 2017: Seasonal prediction skill of northern extratropical surface temperature driven by the stratosphere. *J. Clim.*, doi:10.1175/JCLI-D-16-0475.1.

Karpechko, A. Y., P. Hitchcock, D. H. W. Peters, and A. Schneidereit, 2017: Predictability of downward propagation of major sudden stratospheric warmings. *Q. J. R. Meteorol. Soc.*, doi:10.1002/qj.3017.

Kidston, J., A. A. Scaife, S. C. Hardiman, D. M. Mitchell, N. Butchart, M. P. Baldwin, and L. J. Gray, 2015: Stratospheric influence on tropospheric jet streams, storm tracks and surface weather. *Nat. Geosci.*, doi:10.1038/NGEO2424.

Kolstad, E. W., T. Breiteig, and A. A. Scaife, 2010: The association between stratospheric weak polar vortex events and cold air outbreaks in the Northern Hemisphere. *Q. J. R. Meteorol.*

Soc., **136**, 886–893, doi:10.1002/qj.620.

Konrad II, C. E., and S. J. Colucci, 1989: An Examination of Extreme Cold Air Outbreaks over Eastern North America. *Mon. Weather Rev.*, doi:10.1175/1520-0493(1989)117<2687:AEOECA>2.0.CO;2.

Kretschmer, M., D. Coumou, L. Agel, M. BArlow, E. Tziperman, and J. Da. Cohen, 2018: More-persistent weak stratospheric polar vortex States linked to cold extremes. *Bull. Am. Meteorol. Soc.*, doi:10.1175/BAMS-D-16-0259.1.

Lauritzen, P. H., and Coauthors, 2018: NCAR Release of CAM-SE in CESM2.0: A Reformulation of the Spectral Element Dynamical Core in Dry-Mass Vertical Coordinates With Comprehensive Treatment of Condensates and Energy. *J. Adv. Model. Earth Syst.*, **10**, 1537–1570, doi:10.1029/2017MS001257. http://doi.wiley.com/10.1029/2017MS001257.

Lehtonen, I., and A. Y. Karpechko, 2016: Observed and modeled tropospheric cold anomalies associated with sudden stratospheric warmings. *J. Geophys. Res.*, doi:10.1002/2015JD023860.

Limpasuvan, V., D. W. J. Thompson, and D. L. Hartmann, 2004: The life cycle of the Northern Hemisphere sudden stratospheric warmings. *J. Clim.*, doi:10.1175/1520-0442(2004)017<2584:TLCOTN>2.0.CO;2.

Martineau, P., S. W. Son, and M. Taguchi, 2016: Dynamical consistency of reanalysis datasets in the extratropical stratosphere. *J. Clim.*, doi:10.1175/JCLI-D-15-0469.1.

Matsuno, T., 1971: A Dynamical Model of the Stratospheric Sudden Warming. *J. Atmos. Sci.*, **28**, 1479–1494, doi:10.1175/1520-0469(1971)028<1479:ADMOTS>2.0.CO;2.

Matthewman, N. J., J. G. Esler, A. J. Charlton-Perez, and L. M. Polvani, 2009: A New Look at Stratospheric Sudden Warmings. Part III: Polar Vortex Evolution and Vertical Structure. *J. Clim.*, **22**, 1566–1585, doi:10.1175/2008JCLI2365.1. http://journals.ametsoc.org/doi/abs/10.1175/2008JCLI2365.1.

Mitchell, D. M., A. J. Charlton-Perez, and L. J. Gray, 2011: Characterizing the Variability and

Extremes of the Stratospheric Polar Vortices Using 2D Moment Analysis. *J. Atmos. Sci.*, doi:10.1175/2010JAS3555.1.

——, L. J. Gray, J. Anstey, M. P. Baldwin, and A. J. Charlton-Perez, 2013: The influence of stratospheric vortex displacements and splits on surface climate. *J. Clim.*, **26**, 2668–2682, doi:10.1175/JCLI-D-12-00030.1.

Mudryk, L. R., and P. J. Kushner, 2011: A method to diagnose sources of annular mode time scales. *J. Geophys. Res. Atmos.*, **116**, 1–13, doi:10.1029/2010JD015291.

O'Neill, A., and V. D. Pope, 1988: Simulations of linear and nonlinear disturbances in the stratosphere. *Q. J. R. Meteorol. Soc.*, **114**, 1063–1110, doi:10.1002/qj.49711448210. http://doi.wiley.com/10.1002/qj.49711448210.

Palmeiro, F. M., D. Barriopedro, R. Garcï¿½a-Herrera, and N. Calvo, 2015: Comparing sudden stratospheric warming definitions in reanalysis data. *J. Clim.*, doi:10.1175/JCLI-D-15-0004.1.

Pelly, J. L., and B. J. Hoskins, 2003: A New Perspective on Blocking. *J. Atmos. Sci.*, **60**, 743–755, doi:10.1175/1520-0469(2003)060<0743:ANPOB>2.0.CO;2. http://journals.ametsoc.org/doi/abs/10.1175/1520-0469%282003%29060%3C0743%3AANPOB%3E2.0.CO%3B2.

Plumb, R. A., 1985: On the Three-Dimensional Propagation of Stationary Waves. *J. Atmos. Sci.*, **42**, 217–229, doi:10.1175/1520-0469(1985)042<0217:OTTDPO>2.0.CO;2. http://journals.ametsoc.org/doi/abs/10.1175/1520-0469%281985%29042%3C0217%3AOTTDPO%3E2.0.CO%3B2.

Polvani, L. M., and P. J. Kushner, 2002: Tropospheric response to stratospheric perturbations in a relatively simple general circulation model. *Geophys. Res. Lett.*, **29**, 1114, doi:10.1029/2001GL014284. http://doi.wiley.com/10.1029/2001GL014284.

——, and D. W. Waugh, 2004: Upward wave activity flux as a precursor to extreme stratospheric events and subsequent anomalous surface weather regimes. *J. Clim.*,

doi:10.1175/1520-0442(2004)017<3548:UWAFAA>2.0.CO;2.

Portis, D. H., M. P. Cellitti, W. L. Chapman, and J. E. Walsh, 2006: Low-Frequency Variability and Evolution of North American Cold Air Outbreaks. *Mon. Weather Rev.*, doi:10.1175/MWR3083.1.

Rosier, S. M., and B. N. Lawrence, 1999: The January 1992 stratospheric sudden warming: A role for tropical inertial instability? *Q. J. R. Meteorol. Soc.*, **125**, 2575–2596, doi:10.1002/qj.49712555912. http://doi.wiley.com/10.1002/qj.49712555912.

Seviour, W. J. M., D. M. Mitchell, and L. J. Gray, 2013: A practical method to identify displaced and split stratospheric polar vortex events. **40**, 5268–5273, doi:10.1002/grl.50927.

Sheshadri, A., R. A. Plumb, and E. P. Gerber, 2015: Seasonal Variability of the Polar Stratospheric Vortex in an Idealized AGCM with Varying Tropospheric Wave Forcing. *J. Atmos. Sci.*, **72**, 2248–2266, doi:10.1175/JAS-D-14-0191.1. http://journals.ametsoc.org/doi/10.1175/JAS-D-14-0191.1.

Stray, N. H., Y. J. Orsolini, P. J. Espy, V. Limpasuvan, and R. E. Hibbins, 2015: Observations of planetary waves in the mesosphere-lower thermosphere during stratospheric warming events. *Atmos. Chem. Phys.*, doi:10.5194/acp-15-4997-2015.

Watson, P. A. G., and L. J. Gray, 2014: How Does the Quasi-Biennial Oscillation Affect the Stratospheric Polar Vortex? *J. Atmos. Sci.*, doi:10.1175/JAS-D-13-096.1.

Waugh, D. N. W., 1997: Elliptical diagnostics of stratospheric polar vortices. *Q. J. R. Meteorol. Soc.*, **123**, 1725–1748, doi:10.1002/qj.49712354213. http://doi.wiley.com/10.1002/qj.49712354213.

Waugh, D. W., and W. Randel, 1999: Climatology of Arctic and Antarctic Polar Vortices Using Elliptical Diagnostics. *J. Atmos. Sci.*, doi:10.1175/1520-0469(1999)056<1594:COAAAP>2.0.CO;2.

——, and L. M. Polvani, 2010: Stratospheric polar vortices. *Geophysical Monograph Series*.

——, A. H. Sobel, and L. M. Polvani, 2016: What is the Polar Vortex, and how does it influence

weather? *Bull. Am. Meteorol. Soc.*, **98**, BAMS-D-15-00212.1, doi:10.1175/BAMS-D-15-00212.1. http://journals.ametsoc.org/doi/abs/10.1175/BAMS-D-15-00212.1.

Wohltmann, I., and M. Rex, 2008: Improvement of vertical and residual velocities in pressure or hybrid sigma-pressure coordinates in analysis data in the stratosphere. *Atmos. Chem. Phys.*, doi:10.5194/acp-8-265-2008.

Yiğit, E., and A. S. Medvedev, 2016: Role of gravity waves in vertical coupling during sudden stratospheric warmings. *Geosci. Lett.*, **3**, 27, doi:10.1186/s40562-016-0056-1. http://geoscienceletters.springeropen.com/articles/10.1186/s40562-016-0056-1.

Yu, Y., M. Cai, R. Ren, and H. M. van den Dool, 2015a: Relationship between Warm Airmass Transport into the Upper Polar Atmosphere and Cold Air Outbreaks in Winter. *J. Atmos. Sci.*, doi:10.1175/JAS-D-14-0111.1.

——, R. Ren, and M. Cai, 2015b: Dynamical Linkage between Cold Air Outbreaks and Intensity Variations of the Meridional Mass Circulation. *J. Atmos. Sci.*, **72**, 3214–3232, doi:10.1175/JAS-D-14-0390.1. http://dx.doi.org/10.1175/JAS-D-14-0390.1.